Marquette University
e-Publications@Marquette

Dissertations (2009 -) | Dissertations, Theses, and Professional Projects

Dynamics and Interactions of Membrane Proteins

Azamat Galiakhmetov
Marquette University

Recommended Citation
Galiakhmetov, Azamat, "Dynamics and Interactions of Membrane Proteins" (2018). *Dissertations (2009 -)*. 801.
https://epublications.marquette.edu/dissertations_mu/801

DYNAMICS AND INTERACTIONS OF MEMBRANE PROTEINS

by
Azamat Galiakhmetov, B.Sc., M.Sc.

A Dissertation submitted to the Faculty of the Graduate School,
Marquette University,
in Partial Fulfillment of the Requirements for the Degree of Doctor of Philosophy

Milwaukee, Wisconsin
August 2018

ABSTRACT
DYNAMICS AND INTERACTIONS OF MEMBRANE PROTEINS
Azamat Galiakhmetov, B.Sc., M.Sc.

Marquette University, 2018

Membrane proteins are members of the class of proteins that perform their functions while being associated with a lipid bilayer. In the cell, they serve as transporters, receptors, anchors and enzymes. The domain organisation of these proteins suggests importance of lipid membrane and protein-lipid interactions for protein function. The requirement of a membrane mimic and the level of its resemblance to a native one for protein investigation makes the studies of membrane proteins a challenging project.

My research work is focusing on the biophysical and biochemical studies of membrane proteins. This dissertation outlines two separate projects, each with their own challenges.

Ras proteins are members of a superfamily of small GTPases that act as molecular switches that are involved in signal transduction pathways responsible for cell division and proliferation and, as one might guess, protein malfunction can lead to cancer. Recently, there have been a number of studies that suggest Ras protein dimerization on lipid membranes through protein-protein interactions between G-domains. On the basis of the results obtained from solution NMR and fluorescence polarization anisotropy studies, we concluded that the G-domain of the Ras protein by itself is not prone to dimerization. The result of this work was later confirmed by publications from other groups that performed studies in the presence of the lipid bilayer.

NADPH-cytochrome P450 oxidoreductase (POR) is an integral membrane protein involved in an electron transport pathway transferring electrons from NADPH to cytochrome P450. The goal of this project was the development of methodology to obtain structural data on a high-molecular weight protein associated with lipid nanodiscs in the presence of paramagnetic cofactors. The goal was achieved by application of lipid nanodisc technology, ^{13}C-methyl extrinsic labeling coupled with Methyl-TROSY NMR technique that resulted in signals that showed differential sensitivity towards the redox state of the protein cofactors and conformational transitions of the protein. Moreover, results were obtained on a 600MHz instrument under protonated conditions.

Membrane proteins are challenging systems to research due to diverse interactions they experience on the membrane surface. In this dissertation I successfully utilized two approaches investigating this interactions: in my first project, I separately studied protein-protein interaction underlying the dimerization hypothesis, while in my second project I suggested the approach to explore conformational details and diverse interactions in a lipoprotein complex.

ACKNOWLEDGEMENTS

Azamat Galiakhmetov, B.Sc., M.Sc.

I would like to express my gratitude towards my mother, my father, my sister and all my relatives for the support they provided. I am greatly thankful to my research advisor (Dr. Evgenii Kovrigin) and my past laboratory members for everything they done to help me to reach this step in my academic life. I also would like to thank my committee members (Dr. Martin St. Maurice, Dr. Qadir Timerghazin, Dr. William Donaldson, Dr. Nicholas Reiter) for their feedback on my research and the whole faculty of the Chemistry Department of Marquette University with whom I spent this 5-years together.

TABLE OF CONTENTS

ABBREVIATIONS

POR	NADP-cytochrome P450 oxidoreductase
DOPC	1,2-dioleoyl-*sn*-glycero-3-phosphotidylcholine
DOPG	1,2-dioleoyl-*sn*-glycero-3-phosphoglycerol
DOPS	1,2-dioleoyl-*sn*-glycero-3-phosphotidylserine
ET	Electron transfer
FAD	Flavin adenine dinucleotide
FMN	Flavin mononucleotide
GAP	GTPase activator protein
GDP(GTP)	Guanosine diphosphate (Guanosine triphosphate)
GEF	Guanine nucleotide exchange factor
GTP	Guanosine triphosphate
HVR	Hyper variable region
LUV	Large unilamelar vesicles
MALDI-TOF	Matrix assisted laser desorption/ionization spectrometry time of flight
MANT	N'-Methylanthraniloyl fluorescence label
MBD	POR membrane binding domain
MCC-PE	1,2-dioleoyl-*sn*-glycero-3-phosphoethanolamine-N-[4-(p-maleimidomethyl)cyclohexane-carboxamide
MMTS	Methyl methanethiosulfonate
MTC	Methylthiocysteine
NADPH	Nicotinamide adenine dinucleotide phosphate
NMR	Nuclear magnetic resonance
POPC	1-Palmitoyl-2-oleoylphosphatidylcholine
TROSY	Transverse relaxation optimized spectroscopy

I. INTRODUCTION

Lipid Membranes

Biological membrane

The possibility of emergence of life started with the appearance of membranes – a semi-permeable boundary that separates processes that take place within a cell from the surrounding environment. Nature implemented this vital boundary in the form of a lipid bilayer empowered with molecular trafficking ability, capable of sensing changes in the environment and delivering this information inside a cell.

The major structural elements of biological membranes are lipids. Depending on the membrane's role and location in the cell, lipid moiety and composition can be different. In the literature, lipids constituting a bilayer are generally depicted as having a hydrophilic "head" and hydrophobic "tail", as it is shown in Figure 1 below [1].

There are three common lipid components of a membrane:

1. Phospholipids

   Phospholipids are major components of animal biological membranes [1]. Phospholipid backbones can be divided into two structural elements. Fatty acid acyl chains determine interactions inside a lipid bilayer which are responsible for physical properties of a membrane like fluidity or elasticity. Fluidity is closely related to a lipid melting point: the higher is the melting temperature, the less fluid is the lipid. The presence of unsaturated carbons in the chain leads to a decrease in the melting point of a lipid. This is due to the

fact that double bonds introduce kinks in hydrophobic tails, which lead to a weaker van der Waals interaction between them.

Another structural element is a head group, which determines the lipid surface interactions of the membrane, creating nonpolar and polar domains.

Major phospholipids examples are: phosphatidylserine (PS) and phosphatidylinositol (PI) with the negatively charged head groups; neutral zwitterions like phosphatidylethanolamine (PE) or phosphatidylcholine(PC). Another important representative of this class is sphingomyelin. This phospholipid can be found in greater concentration in nerve cells. It also is a crucial element of specific lipid membrane organizations like lipid rafts or caveolae.

2. Glycolipids

   Glycolipids sometimes are thought as a subclass of the phospholipids, since their main structural elements are the same; the main difference is a modification of head groups by carbohydrates. Due to that fact, the function they perform on the membrane are more distinct — they are usually found on an outer leaflet of a cellular membrane, where they act as recognition sites for other molecules.

3. Sterols

   Sterols play important roles in an organism, serving as hormones, signaling molecules and bile acids. Cholesterol is the most investigated and abundant representative of this class. Due to its structural features, cholesterol promotes more compact packing of phospholipids in a lipid bilayer and because of that it plays the vital role of a regulator of membrane fluidity influencing membrane protein behavior.

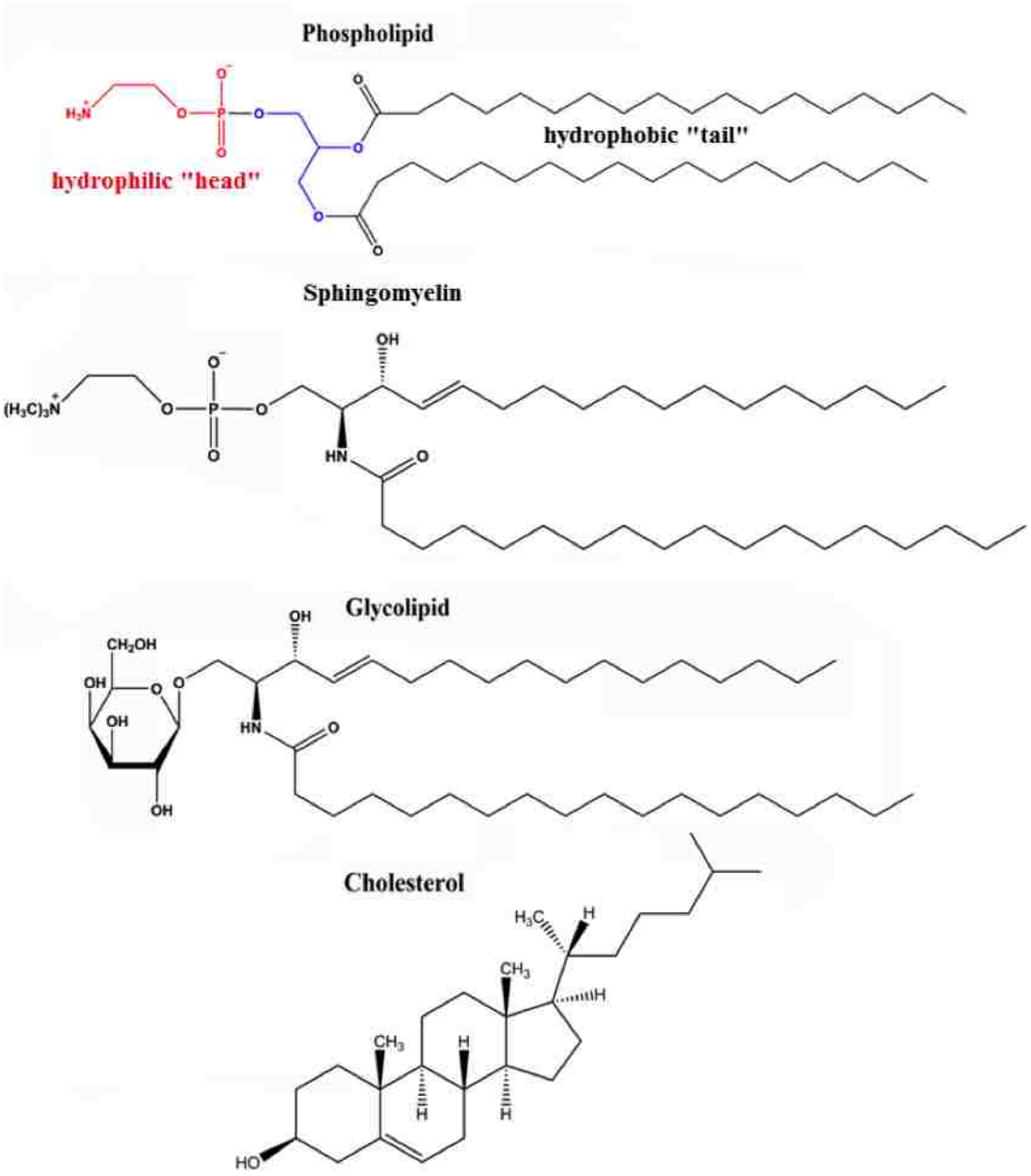

Figure 1. The list of the main lipid classes

Depending on type of the lipid membrane and organism of origin, composition of the lipid bilayer can be diverse. In mammalian cell, framework is made of phosphatidylcholines, while sphingomyelin, cholesterol, phosphatidylserine fluctuates in 10-30% range and phosphatidylinositol, phosphatidylethanolamine moiety are presented by 5-20% [2].

Lipid bilayer organization

Membrane lipids are amphipathic molecules. This molecular property establishes a requirement to insulate long hydrophobic "tails" from water while exposing hydrophilic "head" to a water moiety to be involved into its hydrogen-bonding network. This requirement creates a driving force, known as the hydrophobic effect. Lipid bilayers are capable of creating a number of structures, depending on lipid/water ratio and external conditions.

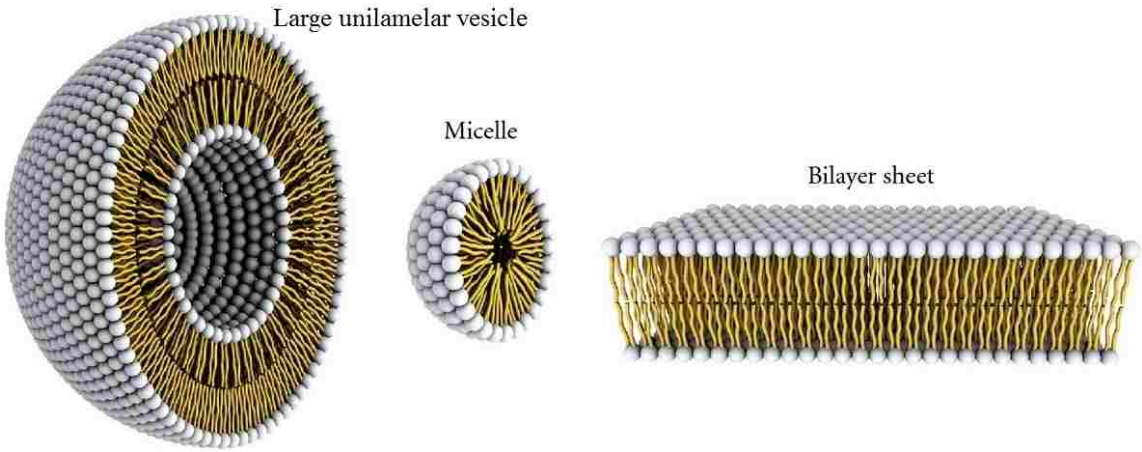

Figure 2. Common biological membrane models. Individual lipids are represented in a cartoon representation where hydrophilic head groups are shown as a white spheres while hydrophobic tails are shown as yellow wave lines [3].

In an aqueous environment, when the lipid portion is small, lipids spontaneously form aggregates called micelles, where hydrophobic tails create the core of a micelle with hydrophilic heads interacting with surrounding water.

If one would increase lipid to water ratio, the lipid moiety in solution will be enough to create a bilayer. This process is driven by the critical micelle concentration which, in turn, depends on packing energies of hydrophobic tails, elastic bending of a monolayer, hydration and electrostatic potential. The critical micelle concentration

(CMC) varies from 10^{-8}-10^{-10} M for membrane lipids. For example, CMC for one of the most common lipids found in biological membranes, 1,2-dihexadecanoyl-*sn*-glycero-3-phosphocholine (DPPC), is equal to 0.46nM [4]. Even a small distortion of a system, such as a physical agitation, can lead to aggregates with an onion-like structure called liposomes in general, and in case of multiple bilayers − multilamelar vesicles (MLV). The application of physical techniques to MLV's, such as sonication or extrusion, can rupture this multi-layered structure to yield, depending on specific characteristic of a treatment, either large unilamelar vesicles (LUV) or small unilamelar vesicles (SUV).

Lipid bilayer domains

A model describing biological membrane behavior — the fluid mosaic model was proposed in 1972 by Singer and Nicoloson [5]. In this model, the lipid bilayer is represented as a two-dimensional liquid where proteins and lipids diffuse freely.

Moreover, cellular membranes are asymmetrical bilayers; first of all, inner and outer leaflets differ in membrane proteins that are associated with the bilayer. Another reason for an asymmetry is a difference in a lipid composition; ratio between constituents of inner and outer leaflets varies. Some lipids can be found mostly on the outer leaflet of a bilayer, but are very scarce on the inner leaflet.

A later model was reviewed and complemented [6] with the ideas of lipid rafts and caveolae due to an emergence of facts [7] that demonstrated that the cellular membrane is not homogeneous: there are microdomains of different composition which laterally diffuse in a bilayer.

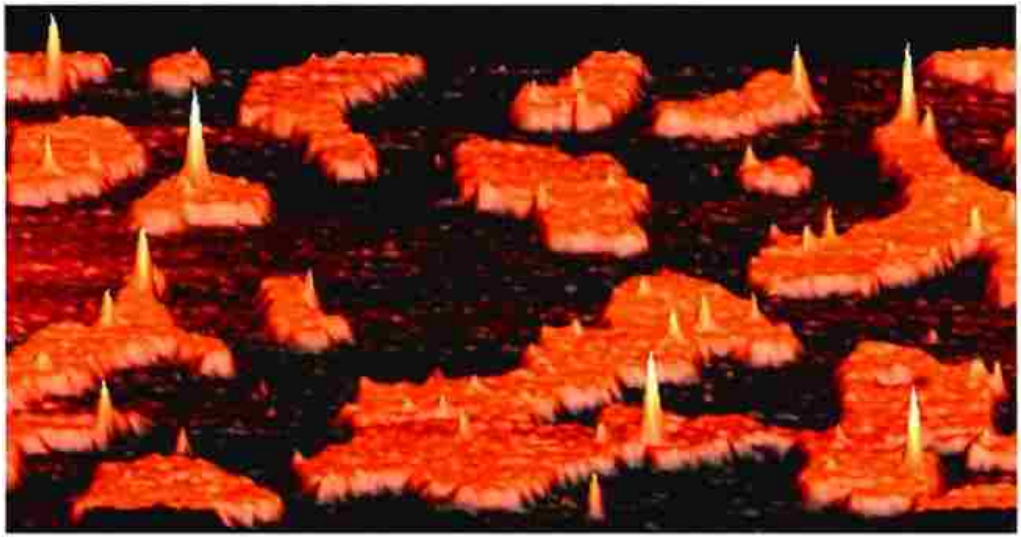

Figure 3. Lipid rafts (red "islands") were observed using atomic force microscopy by detecting the increased thickness of the Lo domains. Spikes correspond to proteins associated with lipid rafts. Reprinted from [8]

Caveolae (Latin for "little caves") are small, flask-shaped invaginations of the bilayer that are one of the forms of lipid rafts. These were first observed in the 1950s [9]. The primary role of caveolae is endocytosis (the process of engulfing extracellular molecules to transport them into the cell). Caveolae formation and maintenance are the main tasks of the protein caveolin. Caveolin has a high binding affinity to lipid rafts. Another feature is a proclivity to oligomerization. Oligomerization of caveolin on the raft, together with higher rigidity due to high cholesterol concentration, is the driving force which leads to bilayer invagination followed by formation of the vesicles. Hereby, caveolin makes the membrane inflect and collapse around a lipid raft, encapsulating vital molecules inside a vesicle.

Lipid rafts are microdomains on biological membrane that are more ordered and tightly packed than the surrounding bilayer, though still retaining fluidity. These microdomains float freely in the membrane bilayer, serving as centers of aggregation, influencing overall membrane fluidity and controlling membrane protein trafficking and signaling. The size of lipid rafts varies from 10-200 nm [10]. In the literature,

domains of high fluidity are called liquid disorder (L_d) , while the ones which are less fluid called liquid order (L_o) .

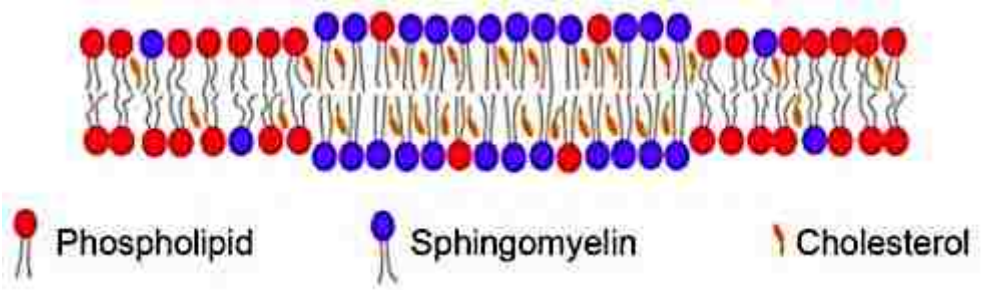

Figure 4. Schematic cartoon representation of a lipid raft on model bilayer.[1]

The reason behind such characteristic organization is enrichment of the domains in cholesterol and unsaturated lipids, specifically sphingomyelin. In fact, cholesterol concentration in lipid rafts is 2-3 fold greater compared to the non-raft bilayer[11].

Being enriched in saturated lipids these domains are thicker compared to a surrounding membrane, which was demonstrated by atomic force microscopy (AFM) spikes which represent protein associated with the membrane (see Figure 3) [12]. It is energetically favored for a membrane to create such binary system, nearly linear long saturated chains prefer to interact with each other to create L_o phase, while unsaturated acyl chain due to kinks of unsaturated carbons prefer to be in L_d phase. The role of cholesterol in a lipid raft is to ensure better packing between lipid acyl chains since the interaction of head groups amends packing.

It should be noted that sphingomyelin, which is essential for lipid rafts organization, is also one of the examples of leaflet asymmetry: its concentration in outer leaflet is

[1] Reprinted from http://www.microscopy-analysis.com

significantly greater than in the inner one [13]. But it has been reported that some intracellular membrane proteins demonstrate differentiation between raft and non-raft domains on the inner leaflet [14]. Reasons for that are the rigidity of lipid raft overall structure and a high local concentration of long-chain saturated lipids in a domain of outer leaflet; weak interactions between hydrophobic tails relay raft-like behavior to the inner leaflet of a cellular domain [15].

Membrane proteins.

This class of proteins carries out their function on biological membranes. It has been reported that up to 30% of all genes encode membrane proteins [16]. One way to categorize such a big class is on the basis of the functions they perform in the cell:

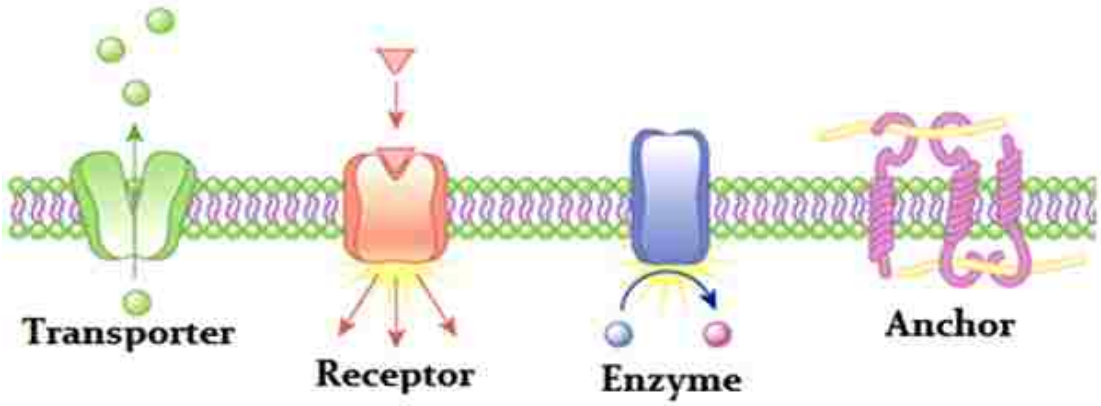

Figure 5. Major classes of membrane proteins depicted on the model of the lipid bilayer.[2]

- Membrane receptors – play communication role whether it is between the cell and the external environment or within the cell between intracellular organelles. Example: receptor tyrosine kinases, which binds growth factors on

[2] Reprinted from http://www.nature.com/scitable/content/ne0000/ne0000/ne0000/ne0000/14706234/U3CP1-4_MemProteinFunction_ksm.jpg

the extracellular side and relay the information to the intracellular side of the membrane.

- Transport proteins – perform transport of essential molecules and ions. Example: potassium channel, which selectively and rapidly transports K^+ ions.
- Cell adhesion molecules – play the role of anchors, for example for a specific cell-cell interaction. Example: bacterial outer membrane protein OmpX which recognizes and specifically binds to host mammalian cell.
- Membrane enzymes – perform catalytic functions that may be coupled with specific interaction. Examples: Ras proteins, which relay signal for cell division/proliferation to downstream messengers.

Another way to classify membrane proteins is by the type of their interaction with a lipid bilayer:

- *Integral membrane* proteins are embedded in the lipid bilayer.
- *Peripheral membrane proteins* are flexibly attached to a bilayer with lipid anchor or through specific interactions with a membrane.

Two conclusions can be drawn from the information above.

1. Membrane proteins are involved in many processes vital for a cell. In fact, 50% of modern drugs targets are membrane proteins [17].
2. To understand their function, they have to be studied in the presence of cellular membrane model. This creates a challenge − due to high complexity, dynamics and the size of investigated systems; research of membrane proteins is a demanding and elaborate task.

My research attention is concentrated on two examples, Ras subfamily of small GTPases and NADP-Cytochrome P450 oxidoreductase.

Ras Subfamily

Members of Ras subfamily are peripheral membrane proteins of small GTPases, involved in processes responsible for cell growth, differentiation and proliferation. Consequently, this subfamily of membrane protein is considered to be proto-oncogenes. In fact, mutations in Ras proteins were observed in 20-25% cases of all human cancers [18].

The Ras subfamily is comprised of three members:

- *H-Ras* (*H*arvey *RA*t *S*arcoma) – has 3 lipid anchors, consisting of 1 farnesyl and 2 palmytoyl
- *N*-Ras (*N*euroblastoma) – has 2 lipid anchors, consisting of 1 farnesyl and 1 palmytoyl
- *K*-Ras (*K*irsten) (has 2 splice variants that differ in anchor region that interacts with lipid bilayer surface)
    - K-Ras4A – has 2 lipid anchors consisting of 1 farnesyl and 1 palmytoyl
    - K-Ras4B – has only a farnesyl lipid anchor but has 6 sequential lysines that create an additional mode of interaction with positively charged lipid head-groups.

All three Ras isoforms contain a conserved G-domain (*guanine-nucleotide binding domain*) and a C-terminal *HVR (HyperVariable Region*). The C-terminal HVR is the region protein where the main difference between isoforms is located and which determines their unique behavior on the membrane. Despite interacting with similar effectors, each isoform demonstrates distinct signal features [19].

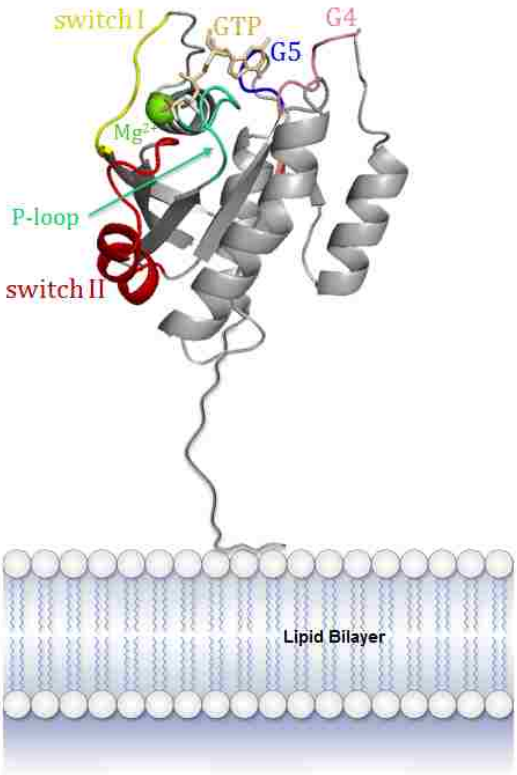

Figure 6. Ras protein G-domain structure. Five G motifs are depicted as G1(limegreen), G2(yellow), G3(red), G4(light pink), G5(blue). Mg^{2+} ion shown as a green sphere while GTP nucleotide is depicted as stick model of wheat color.

Ras G-domain carries 5 G motifs which are essential for nucleotide binding, allosteric interactions and guanosine triphosphate (GTP) hydrolysis:

- G1 – P-loop, *GxxxGKS/T* binds β-phosphate of the nucleotide (GDP/GTP)
- G2 – *Switch I*, includes Threonine-35 that binds terminal γ-phosphate group of GTP and Mg^{2+} ion in nucleotide binding pocket.
- G3 – *Switch II*, includes Glutamine-61, which activates water for nucleophilic attack on the γ-phosphate group of GTP for hydrolysis.
- G4 – *LVGNKxDL* motif provides specific guanine nucleotide interaction.
- G5 – *sAk* motif, A- Alanine-146, essential to Guanine nucleotide binding, where *s* and *k* are Serine-145 and Lysine-147, respectively.

After ribosomal synthesis, a protein may require additional modification, necessary for proper operation or activation. These processes include cleavage of a specific sequencer or phosphorylation, glycosylation, methylation, acetylation, lipidation and proteolysis. [20].

In the case of Ras, after being synthesized as cytosolic precursors, proteins undergo post-translation modification on C-terminal *CaaX* motif (where *C*- stands for Cysteine, a- any aliphatic aminoacid, *X* – can be Serine/Methionine):

- Palmitoylation, addition of palmitic acid, 16 carbon saturated acid attached via thioester bond to a cysteine.
- Isoprenylation, addition of farnesyl, 14 carbon unsaturated group attached via thioether bond to a cysteine.

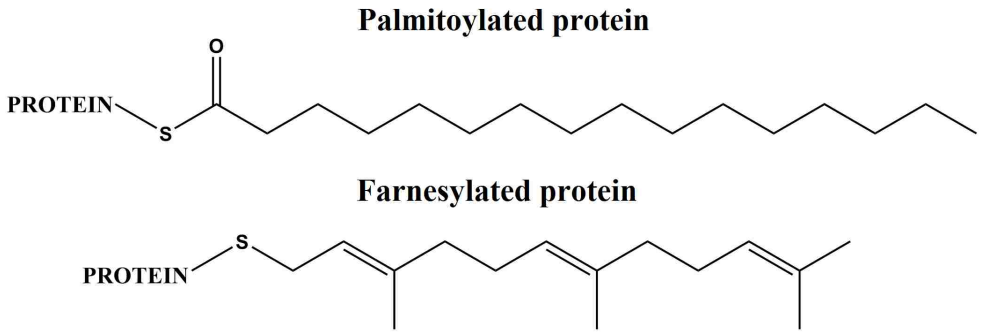

Figure 7. Lipid anchors introduced in Ras during post-translational modifications.

CaaX motif is recognized by farnesyl transferase, an enzyme that attaches a farnesyl group on a cysteine of the Caax motif [21]. After this step, Ras associates with the endoplasmic reticulum (ER), where *aaX* is cleaved, and is followed by methylation of the C-terminal farnesylated cysteine by methyltransferase[22].

In the next step H- and N-Ras are palmitoylated by Ras palmitoyltransferase on ER and targeted by sequence following terminal cysteine to cellular membrane through

Golgi. In the case of K-Ras, its association with a membrane proceeds through an unknown pathway [23].

Ras proteins serve as a molecular switch in a signal transduction pathway from a receptor tyrosine kinase activated by a signal molecule to downstream secondary messengers. Representatives of this family are involved in mitogen-activated protein kinase (MAPK) signal transduction cascade also called RAS-RAF-MEK-ERK cascade according to the proteins involved in it. The GDP-bound state of a protein is considered to be an "OFF" state of the molecule. In this state, the signal is not transmitted. For the protein to get activated it needs to be loaded with GTP. *GEF – Guanine nucleotide Exchange Factor* is the protein that promotes GDP dissociation. After GDP is released in the cytosol, due to a greater GTP concentration and a high GTP affinity of the G-domain, the protein gets loaded with GTP and undergoes a conformational change.

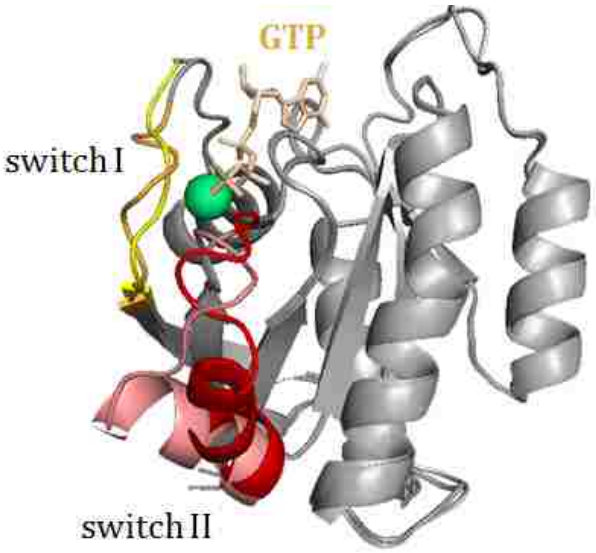

Figure 8. Overlapped crystal structures of Ras G-domain in "ON" and "OFF" states. GTP-bound "ON" state is represented by yellow Switch I and red Switch conformations. While GDP-bound "OFF" state is depicted with orange Switch I and pink Switch II conformations. GTP nucleotide (from ON state) is shown on the figure to demonstrate nucleotide orientation in Ras nucleotide binding pocket.

As a GTPase, Ras proteins possess an intrinsic activity to hydrolyze GTP, but this process is slow; the reaction is catalyzed by *GAP – GTPase-Activating Protein* leading to the reaction rate enhancement of 4-5 orders of magnitude compared to intrinsic hydrolysis by Ras [24].

From Ras signaling cycle depicted below

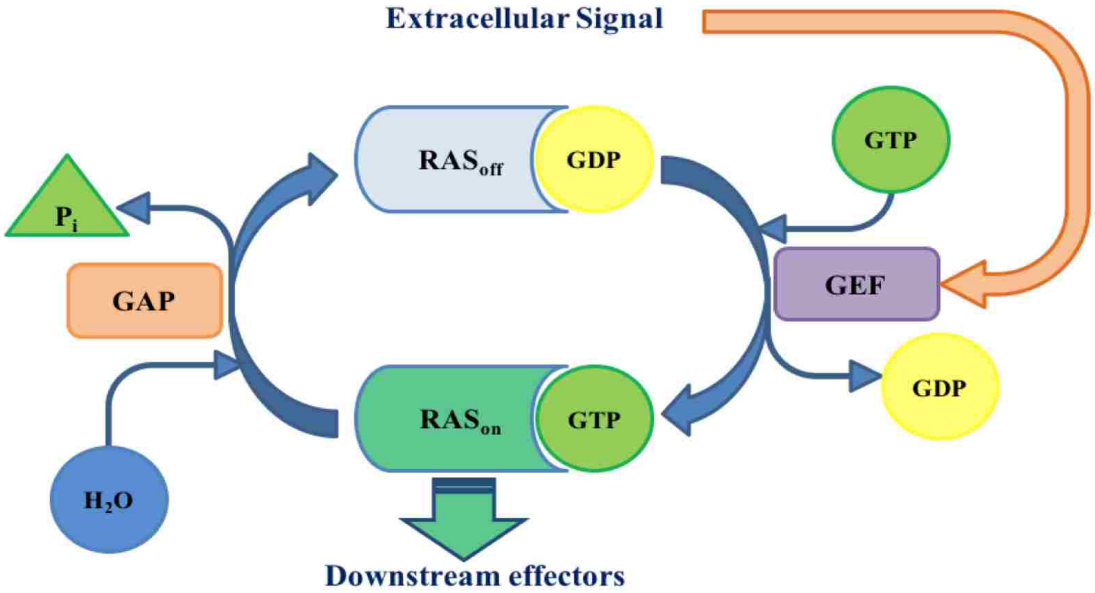

Figure 9) one can suggest two possible ways how mutation can distort Ras performance: either by abolishing/enhancing its function as a GTPase or by diminishing/reinforcing its interaction with GAP.

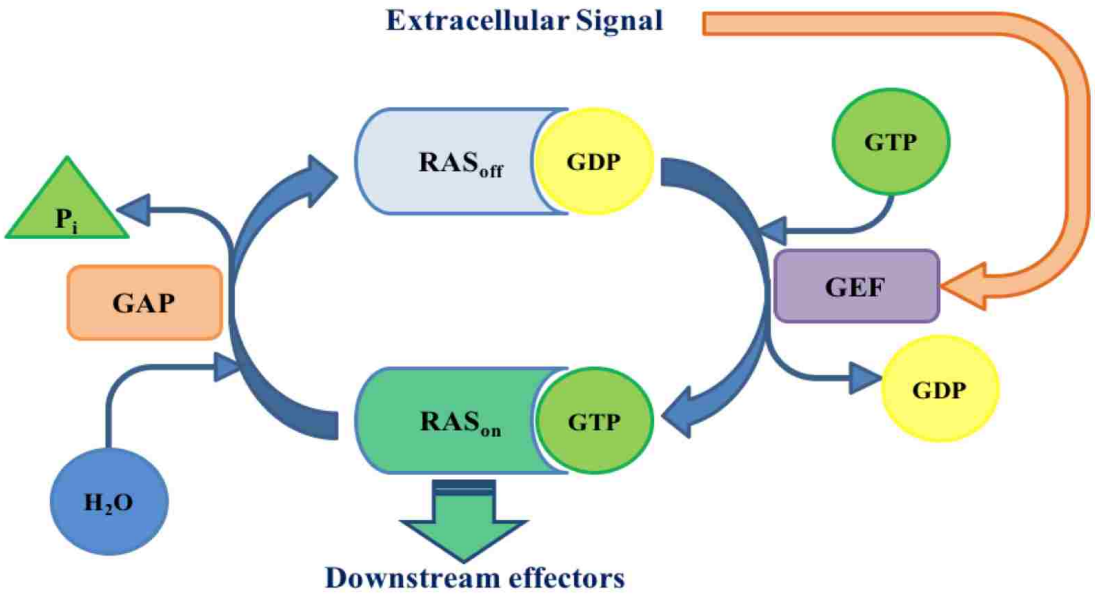

Figure 9. Ras proteins signaling scheme. Abbreviations on the figure: GTP(GDP) – guanosine triphosphate (diiphosphate); GEF – guanine nucleotide exchange factor; GAP – GTPase activator protein: P_i – inorganic phosphate group

Localization on a plasma membrane

The presence of saturated palmitoyl group as a lipid anchors two in H- and one in N-Ras isoforms allows their association with the L_o (liquid ordered) domains of a lipid rafts, while the presence of highly unsaturated farnesyl chain requires interaction with L_d (liquid disordered) domain [25]. In addition to this, K-Ras has a polybasic lysine sequence in a anchor region which creates different mode of interaction. All this suggests different localization of the signaling proteins on the plasma membrane.

Latest [14] quantitative electron microscopy studies demonstrate that 50% of GDP-loaded H-Ras is localized on lipid rafts, while none was found in case of GTP-loaded state. K-Ras on the other hand, predominantly was observed on liquid disorder moiety in both nucleotide bound states. Recent studies of N-Ras showed that regardless to GDP/GTP state, protein remained associated with a boundary between lipid rafts and liquid disordered domains [26].

In the light of these findings, it was proposed that H-Ras exists in a dynamic nucleotide-dependent equilibrium between raft and non-raft domains. This model is in agreement with reports, which observed that GDP-loaded H-Ras has a higher lateral mobility in cholesterol-depleted cells [27]. Due to smaller concentration of cholesterol total concentration of lipid rafts in a bilayer is smaller, which leads to a greater lateral movement of H-Ras after GTP hydrolysis.

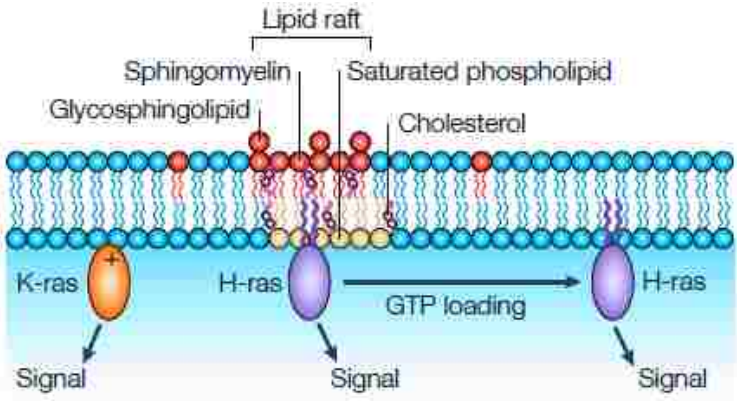

Figure 10. Model representation of nucleotide-dependent localization of K-Ras and H-Ras isoforms on a lipid membrane. Reprinted from [28].

Moreover, it was also observed that K- and H-Ras in GTP-loaded state occupy distinct non-raft micro-domains. Authors suspected that the main reason for that is an interaction between protein polybasic anchor moiety with the domain of a distinct (acidic) lipid composition.

Dimerization of Ras

Despite the fact that, so far, Ras proteins in solution and on the lipid bilayer [29] were observed as a monomers, it has recently been reported [30] that Ras proteins form dimers in the presence of a lipid bilayer. It should be noted that several members across the Ras GTPase subfamilies are known to dimerize [31, 32]. This phenomenon

is specifically interesting since activation of Raf, one of the Ras effectors, requires Raf dimerization [33] and it was proposed that Ras may dimerize to activate Raf. Dimerization can affect protein behavior on the membrane including interactions with other downstream effectors that do not require dimerization, interactions with the lipid bilayer and mobility on the membrane surface which was demonstrated to be crucial for Ras isoforms during their cycle.

In 2012 Gaudenhapt et al. reported on dimerization of N-Ras on POPC (1-Palmitoyl-2-oleoylphosphatidylcholine) membranes using Fourier transform infrared spectroscopy (FTIR) and Forster resonance energy transfer (FRET) [34]. Originally obtained FTIR data implied on perpendicular orientation to the membrane of N-Ras α-helices, which was in contradiction with Molecular Mechanics (MM) simulations that in turn suggested parallel orientation to the membrane. After that, authors analyzed 71 Ras protein crystal structures and in 51 of them they observed Ras similar packing of G-domains. The more detailed investigation of crystal structures allowed to suggest residues that are involved in protein-protein interaction (Figure 9). In the light of this data, it was proposed to include a dimerization model in MM simulation. New results obtained were in agreement with experimental data.

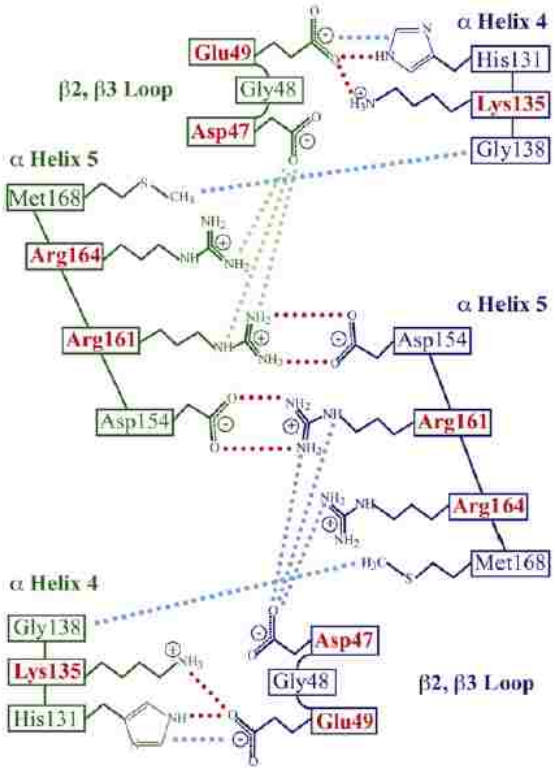

Figure 11. Proposed salt bridges (dotted line) supporting dimer formation where green amino acid residues come from one RAS molecule and blue from the other molecule in a crystal structure. Reprinted from [30].

To verify Ras dimerization, independent FRET studies using Mant-GDP (2'-(or-3')-O-(*N*-Methylanthraniloyl) Guanosine 5'-Diphosphate) and TNP-GDP (2'-(or-3')-O-Trinitrophenyl Guanosine 5'-Diphosphate) as donor-acceptor pair were carried out, according to the results which demonstrated decreased Mant-GDP fluorescence lifetime due to FRET from 5.5 ns to 4.9 ns. Taking into consideration that not all Ras dimers had formed donor-acceptor pairs, the actual FRET efficiency was calculated to be 28%, which corresponds to FRET distance 46 ±6 Å. This value can only be explained in case of oligomerization of the proteins, which was suggested by MM simulations. To exclude FRET due to overcrowding of the proteins on the membrane surface, loading on the membrane models was calculated to be 8%. Interestingly, N-Ras in solution at 10μM concentration demonstrated only 3.5% FRET efficiency thus excluding dimerization in a solution at physiological conditions.

Lin et al. applied fluorescence spectroscopy, single-molecule-tracking and step-photobleaching to investigate H-Ras molecules tethered to a lipid membrane with non-native lipid anchor [35]. This was done to analyze intrinsic ability of a G-domain to form dimers and exclude a lipid anchor clustering effect. Additionally, another doubly lipidated protein construct was used to check whether this process is affected by a number of anchors. Authors emphasize that this is a membrane-induced process since H-Ras did not form dimers in a solution at comparable concentrations.
H-Ras lateral diffusion on a lipid bilayer was monitored by single-molecule tracking (SMT) technique applying Einstein diffusion equation in cylindrical coordinates to the fluorescently labeled protein after step-wise of photobleaching [35]. Using SMT, two groups of species with different lateral mobilities were determined. Noticeably one group had a significantly slower lateral mobility while requiring two steps of photobleaching. Dimer moiety in experiments was estimated to be 10-20% depending on the technique applied at protein surface density 50-100 molecules/μm^2.

In addition, Muratcioglu et al. reported dimerization of K-Ras4B in GTP-bound state, but not GDP-bound state, on the lipid bilayer [36]. Interestingly, two populations of dimer interfaces were observed, one named "β-sheet dimer" was highly populated with the dimer interface involving effector-binding regions [37] and Switch I region, while the other was named "α-helical". During dynamic light scattering experiment of the GDP-loaded Ras, G-domain showed presence of a species with a mass 18 kDa, but GTP-γ-S(slowly hydrolysable GTP analog) demonstrated presence of globular species with the size which corresponds to 41kDa.

Additionally, authors performed NMR studies and analyzed dilution induced chemical shift perturbation for active-like and inactive full-length proteins that demonstrated highly dynamic association involving several sites. It was proposed that dimer

formation provides a mechanism for Raf kinase dimerization and as a consequence control over its signaling, since one of the dimer interfaces can play an inhibitory role while its counterpart is promoting dimerization of Raf.

In a summary, details of how Ras isoforms functions on the membrane surface, selectively interacting with diverse downstream effectors remains unknown. And how dimerization can impact protein behavior needs to be clarified, since it will affect not only interaction with downstream effectors but also protein lateral mobility on the lipid bilayer during activation/inactivation cycle.

NADPH-cytochrome P450 oxidoreductase

NADPH-Cytochrome P450 oxidoreductase (CPR/CYPOR/POR) is a 78kDa integral membrane protein involved in electron transduction pathway from NADPH to Cytochrome P450, where 2 electrons from NADPH are being transferred to 1 electron acceptor heme of cytochrome P450. Cytochrome P450 is involved in drug and hormone metabolism. For example, liver Cyt P450 metabolizes 75% of drugs [38]. As a member of diflavin oxidoreductase family, it contains one molecule each of flavin adenine nucleotide (FAD) and flavin mononucleotide (FMN).

POR molecule has 3 domains:

- FMN-Domain
- Membrane-Binding Domain (MBD)
- FAD-domain (which can itself be divided)

The FAD and FMN domains are connected by a so called “hinge-loop”, it has been suggested that hinge and connecting domain are responsible for relative domain movements, which are thought to be controlling electron transfer [39].

Domain structure

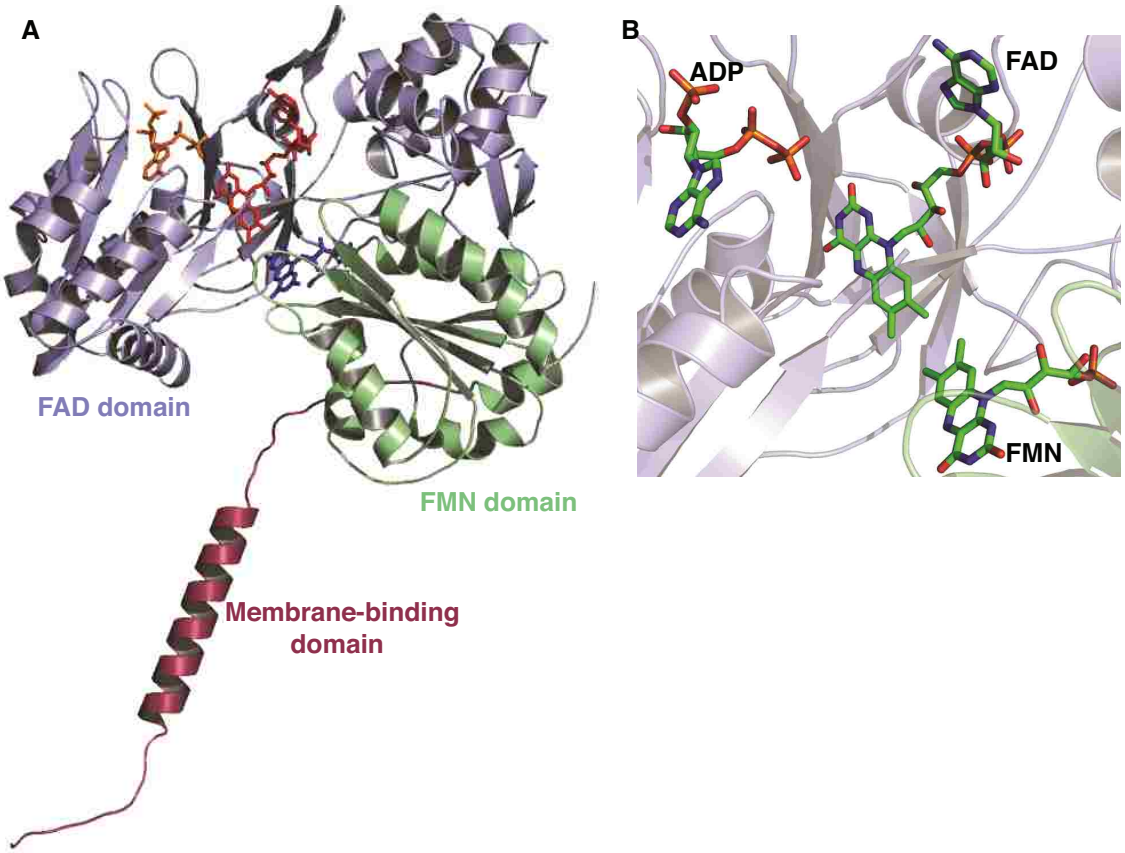

Figure 12. A**.** POR domain structure modeled on the base of the 1AMO crystal structure of the cytosolic portion of POR while Membrane-binding domain was added in PYMOL and model according to results reported by Huang [40]. FAD, FMN and Membrane-binding domain are depicted in a cartoon representation colored slate blue, pale green and maroon, respectively. Cofactors are represented as colored sticks in red (FAD), blue (FMN), orange ($NADP^+$ only ADP moiety is visible). B. Enlarged portion of the crystal structure that demonstrates relative positioning of the cofactors within the protein. Cofactors are shown as sticks with carbon, nitrogen, oxygen, phosphorous atoms are colored green, red, blue, orange, respectively.

MB domain

POR is bound to endoplasmic reticulum by N-termini 56 amino acids (from here on the residue numbers will be given for rat POR, unless mentioned otherwise) of Membrane-binding Domain. Ramamoorthy et al. investigated rat POR MBD using ^{31}P solid-state NMR and determined that residues 22-44 form a helical secondary

structure crossing the bilayer with a tilt of 13° from the bilayer normal [40].

While presence on the membrane is required for interaction with cytochrome P450, it has been shown that both soluble, obtained after cleavage by trypsin at Lysine-56 position, and membrane-bound POR are capable of electron transfer to other electron acceptors (Cytochrome b5, Heme oxygenase etc.) [41]. The ability of a POR to interact with Cytochrome c (non-physiological electron acceptor) is actively applied in its activity studies [42].

It's generally thought that MBD is not involved in catalytic activity and its purpose is to localize POR on the membrane surface, though evidence exists that it might be involved in recognition by specific cytochromes [43]. It was demonstrated by Sligar et al. [44] that presence of the membrane and membrane composition can influence reduction potentials of the cofactors.

FAD domain

FAD domain is comprised of residues 267-678. Nucleotide is tightly bound to the FAD domain (K_d < 1nM) [45]. FAD binding is assisted by Arg454, which stabilizes the pyrophosphate negative charge and Tyr456, positioned close to the isoalloxazine ring with its hydroxyl group forming a hydrogen bond with the hydroxyl group at the 4' position in ribose [46]. Mutation of Ser457, Asp675, and Cys630 to aliphatic amino acids leads to a 1000-fold decrease in catalytic activity — these residues orient the NADP nicotinamide moiety for optimal hydride ion transfer.

Mutagenesis studies and crystal structure analysis of human POR [47] revealed that Trp676 substitution reduces catalytic efficiency due to protein inability to release oxidized nicotinamide from binding pocket. In addition to this, crystallographic

analysis of rat POR Trp677Gly mutant [48] revealed that the NADP nicotinamide group takes position optimal for hydride transfer to FAD, where the Trp677 indole ring is positioned in a wild-type protein. It was proposed that Trp677 moves away from FAD isoalloxazine ring to facilitate hydride transfer and after that moves back to promote NADP release.

In 2011 Xia et al. [49] analyzed POR mutant where one of salt bridges between FAD and FMN domains was substituted to disulfide bond. Crystal structure revealed change of the position of ^{631}GDAR^{634} loop as well as absence of a NADP in the binding pocket. Due to a strong binding of NADP 2'-phosphate group authors proposed that this loop movement, named Asp-loop, maybe involved in the process of $NADP^+$ release.

FMN domain

The FMN-domain is composed of residues 67 to 231. The FMN domain plays a central role in the electron transfer process, recognizing FAD domain to accept electrons from reduced nucleotide to transfer them later to an acceptor. Thus, its surface is capable of interaction with multiple diverse partners meaning that residues affect its electron transfer activity towards one electron acceptor yet can have no effect for another acceptor.

FMN binding is ensured by two tyrosine residues at positions 140 and 178. These two residues are positioned in re- and si-face respectively of the isoalloxazine ring of FMN, thus playing a vital role in the cofactor binding, for instance, mutation Tyr178Asp results in 300-fold decrease in nucleotide binding [50]. Unlike FAD, FMN-nucleotide is loosely bound with $K_d \sim 10^{-8}$ M and can be removed by salt treatment [51].

The FMN domain surface proximal to nucleotide binding site of a POR is negatively charged and interacts with the positively charged surface region close to heme of cytochrome P450. Hamdane et al [42] proposed a model of POR-P450 2B4 complex, where the surface of interaction mentioned represents 58% of total contact area between two molecules; authors stated that not only electrostatic but also a hydrophobic interaction is necessary for the interaction. In this complex, heme and FMN nucleotide are positioned perpendicular to each other while the distance between them is 12 Å. This distance is too long for efficient electron transfer, but Phe429 and Glu439 of cytochrome were found between FMN nucleotide and heme cofactors, allowing authors to assume that they are promoting electron transfer playing the role of "wire".

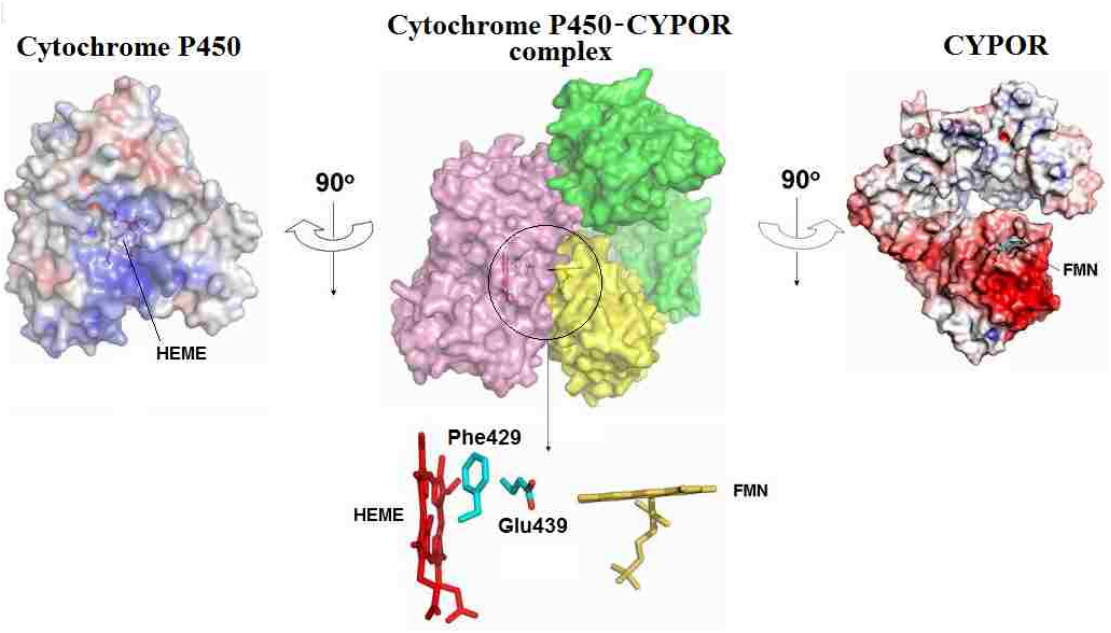

Figure 13. Model of complex formation between POR Δ TGEE and Cytochrome P450. Red color on POR surface represents negatively charged residues; blue– positively charged ones on cytochrome P450 on the left and right panels. Panel on the bottom shows relative orientation of two cofactors (heme and FMN) and residues located between them. Central panel demonstrates relative orientation of the proteins in a proposed model where pink is cytochrome P450, while yellow and green corresponds to FMN and FAD domains of POR, respectively. Reprinted from [41].

The same mode of electron transfer was earlier proposed by Sevrioukova [52] for cytochrome P450-BM3, flavocytochrome from *Bacillus megaterium*, which contains both heme and FMN nucleotide in one unit and acts as homodimer, where reductase of one of the domains reduces heme of another. In this protein crystal structure orientation of cofactors is very similar to that of the complex created by Hamdane et al. while the distance between them is even greater ~18Å.

Residues involved in interaction depend on binding partners providing selectivity, such that ^{213}EED^{215} mutation leads to a significant decrease in level of interaction of cytochrome c, while unaffecting interaction with P450 [53]. At the same time, another group [54] demonstrated that replacement of ^{115}EE^{116} is essential for POR-P450P2B1 complex formation.

Electron transfer

First, a hydride ion from NADPH is transferred to FAD then electrons, one by one are transferred to FMN. This key ability of engaging in both 1- (semiquinone) and 2-electron (hydroquinone) reduction as well as flavins localization in two separate domains provides means to control electron transfer between donor – NADPH and acceptor. It should be noted that the fully reduced form of a POR can be obtained under specific conditions [55] but was never observed *in vitro*. Table 1 provides mean values for the reduction potentials. Data was obtained for solubilized POR of different organism (human [56], rat [44]). The following demonstrates that the driving force of electron transfer is $FMN_{OX/SQ}$ reduction potential.

Table 1. Reduction potentials for POR electron transduction.

Compound	**~E^0, mV**
NADP/NADPH	-320
FAD $_{OX/SQ}$	-310
FAD $_{SQ/HQ}$	-380
FMN $_{OX/SQ}$	-90
FMN $_{SQ/HQ}$	-270

Depending on number of electrons carried by flavins in POR, they can be in the oxidized (ox) state, one-electron reduced semiquinone(sq) state or the two-electron reduced hydroquinone (hq) states. Neutral semiquinones have a broad absorbance with maxima at 585-600, which imparts to their blue color in pH range 6.5—8.5 while oxidized nucleotides have absorption maxima at 450 and 380 nm. This spectral feature was useful in characterization of POR oxidation state during experiments. Under aerobic conditions, the semiquinone state of nucleotides differs in stability: FAD is rapidly oxidized in air while the FMN semiquinone is stable. Moreover, FMN semiquinone has additional absorption maxima of lower intensity at 630nm. This characteristic behavior enables discrimination between FAMH and FADH and analysis of 1 electron transfer from FAD to FMN [51].

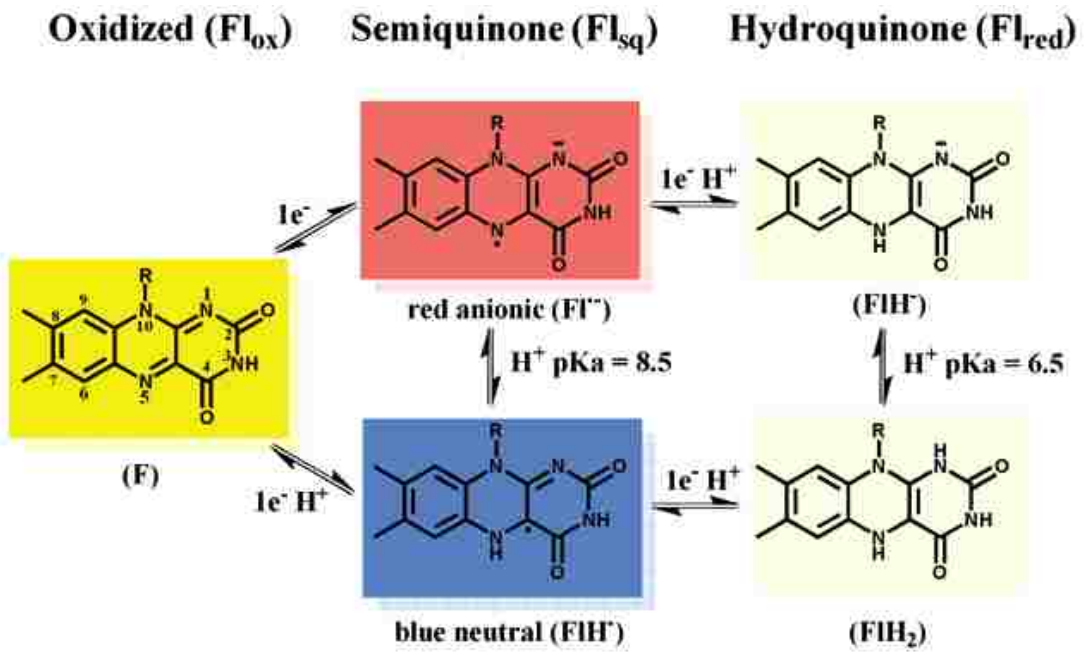

Figure 14. Redox states of the flavins isoalloxazine ring and corresponding redox reactions. Colors corresponds the visible emission spectrum maxima of corresponding species. Reprinted from [41].

As Figure 15 below illustrates, 2 electrons from NADPH are transferred to a FAD in a form of hydride-ion, after that electrons one by one are transferred from FAD to FMN, since FMN semiquinone is stable, electron transfer to one-electron-acceptor cytochrome P450 occurs from hydroquinone FMN, after that another moiety of NADPH binds POR to reduce FAD nucleotide to produce 3 electron reduced state and cycle repeats. It is thought that fully oxidized protein does not exist in the functional cycle of POR.

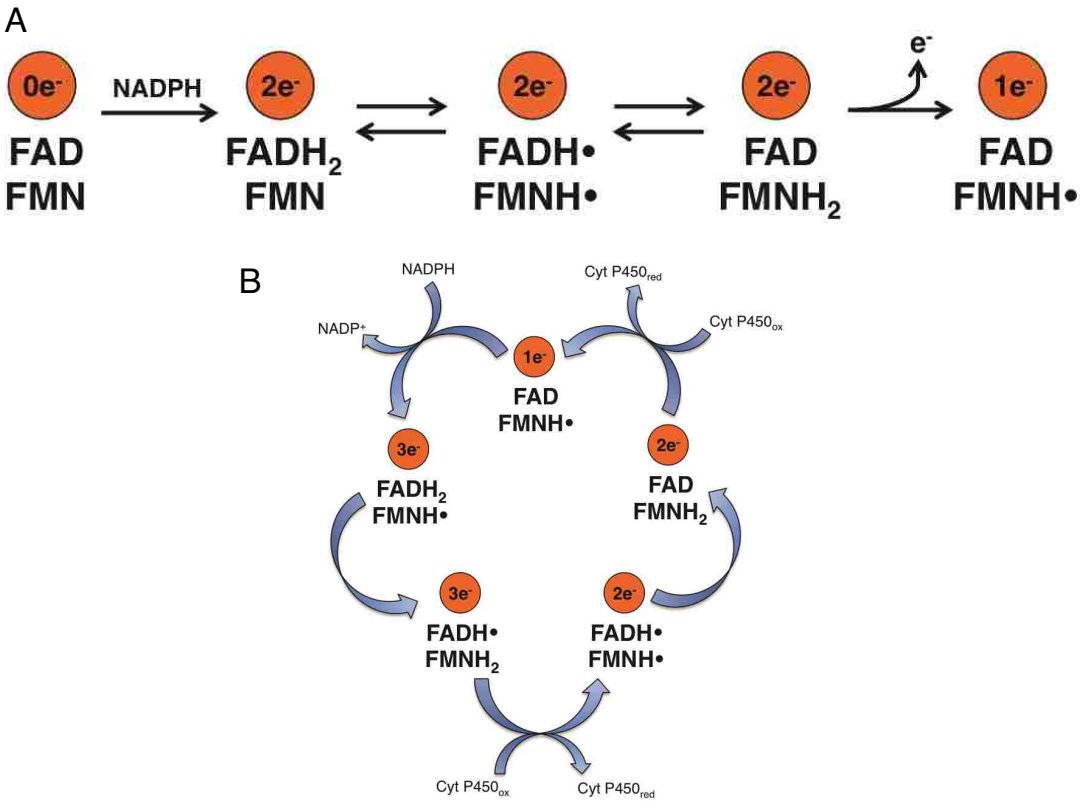

Figure 15. A. Prime redox reaction during one POR cycle. B. Redox cycling of flavin cofactors within POR in vivo.

In a crystal structure obtained for wild-type POR, enzyme was found in a closed conformation, where two flavins moiety are ~ 4Å apart and oriented approximately with 150° angle to each other, which leads to overlap between π-π systems of cofactors [48]. Such orientation should provide very fast electron transfer. But there are two matters that need to be considered:

1. Electron transfer measured during the experiment [57] using stop-flow experiments with NADPH and non-native reducing agent (dithionite) and tracking the change in absorbance of specific bands mentioned previously obtained electron transfer rate of ~50 s^{-1}
2. Moreover, closed conformation observed does not allow further electron transfer from reduced FMN hydroquinone to 1-electron acceptors heme of a cytochrome.

The fact that two cofactors are in separate domains serves as mechanism for electron transfer control; mutagenesis results obtained on unstructured hinge loop serve as a proof to this statement.

In 2002 Gutierrez et al. published a paper where they measured rate of electron transfer by analyzing change in absorbance along the titration [57]. Interestingly, rate of the electron transfer was 55±2 s^{-1} when NADPH was used as a reducing agent. In the case where the chemical reducing agent, dithionite, was used, the rate obtained was 11± 0.5 s^{-1}. It was proposed that presence of NADP moiety in binding pocket is crucial for efficient performance of POR. It was proposed that POR performance involves a conformational gating mechanism, which was demonstrated by carrying out a titration in solution of a different viscosity varying glycerol concentration, it was observed that higher viscosity leads to decrease of electron transfer [57].

Hamdane et al. created a mutant lacking ^{236}TGEE^{239} fragment in a so-called "hinge loop", residues of CD which link FAD and FMN domains together. Using activity assays, it was discovered that the mutant is unable to transfer electrons from FAD to FMN nucleotides; crystallographic structure analysis of the mutant demonstrated that mutant POR is represented in form where distance between FMN and FAD cofactors is 30-60Å, this conformation is actively discussed in literature as "open conformation". Interestingly increase of the loop length by addition of four Ala leads to increased rate of electron transfer [42]. However biological activity studies with chemically reduced FMN nucleotide demonstrated ability of POR mutant to reduce heme of cytochrome P450 B24.

As a conclusion, authors proposed a mechanism for FAD domain movement along with electron transfer (see Figure 16).

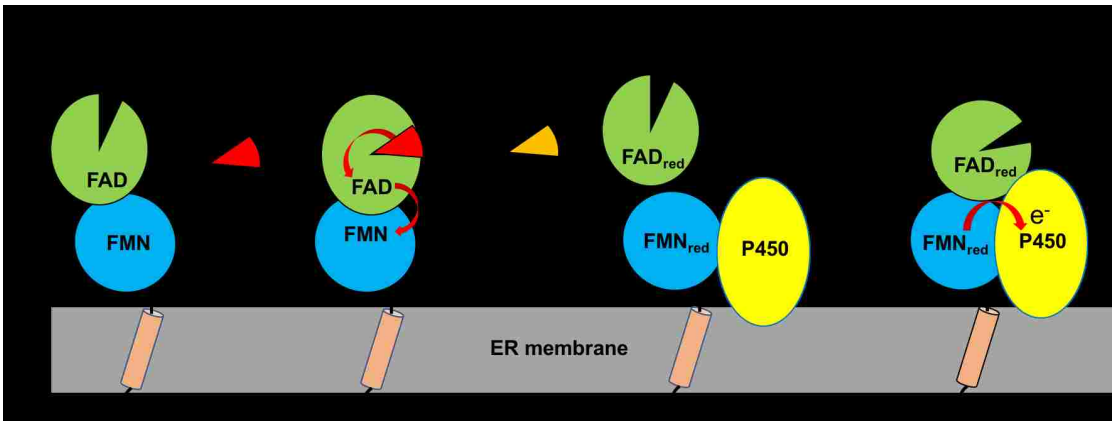

Figure 16. Proposed mechanism of a POR electron transfer on ER membrane.

1. Oxidized POR exists on the membrane in the open conformation.
2. NADPH nucleotide binding leads to a conformational change in a protein and results the formation of the closed state, similar to that observed in a wild-type crystal structure. Electron transfer to FMN nucleotide take place
3. Reduction of FMN nucleotide leads to conformational changes and protein adopts to open conformation with simultaneous release of $NADP^+$ from a binding site, suggesting that large-scale changes are coupled with the Trp677 and Asp632 residue movements.
4. One of a cytochrome (depicted as a red balls) located in close proximity interacts with the reduced FMN and forms a complex which promotes electron transfer to heme.

Xia et al. [49] created a mutant with an engineered disulfide bond between FMN and FAD domains, where salt bridge residues Asp147-Arg514 of wild-type POR were mutated to cysteines, creating an artificial closed conformation of a POR(147C-514C). Residues were selected to be deep enough in a new structure to ensure that disulfide bridge won't be accidentally reduced.

Using spectroscopic analysis of the characteristic absorptions bands specific for the FMN and FAD nucleotides in different redox states during titrations, rates of electron transfer were measured.

It is noteworthy that rate of inter-flavin electron transfer (ET) for the bridged structure was ~ 40 times slower compared to the wild type (1.7 s^{-1}). While ET to acceptors (P450 2B4 and cytochrome c) decreased by more than 90%. Comparison of crystal

structures of the mutant to that of a wild-type POR revealed that relative position of FMN and FAD nucleotide is shifted at 20° angle in a bridged structure, which leads less π-π systems overlap. Authors also performed disulfide bond reduction and carried out the same activity assays to demonstrate that the effect is reversible, where they observed recovery of activity. The table below demonstrates rates obtained using 1 molar and 10 molar equivalents of NADPH at 30°C, using change in absorbance at 452 nm for flavin reduction and 585nm for semiquionone state; change in absorbance were fitted using multi-exponential functions.

Table 2. Rates of ET obtained from redox titration.

Construct	585nm		452 nm		
	k_1, s^{-1}	k_2, s^{-1}	k_1, s^{-1}	k_2, s^{-1}	k_3, s^{-1}
1 molar equivalent NADPH					
Wild-type POR	79 (62%)	6.2 (38%)	75 (79%)	6.1 (21%)	
147C-514C	1.7 (39%)	0.2 (61%)	64 (25%)	12 (43%)	0.8 (32%)
10 molar equivalent NADPH					
Wild-type POR	91		76 (73%)	9.1 (27%)	
147C-514C	52		52 (43%)	2.5(17%)	0.7 (40%)

Moreover, analysis of the crystal structure of the mutant (3JOW) demonstrated that 147C-514C POR lacks presence of a $NADP^+$ in a binding site despite presence in excess in crystallization process. This observation shows that the mutant has a lower affinity to $NADP^+$ compared to a wild-type structure.

Another effect that was observed was a presence of second exponential obtained from the fitting procedure. Originally authors associated it with a hydride transfer from NADPH to FAD nucleotide, but additional experiment carried out in deuterated conditions revealed fallacy of this statement, since no isotopic effect was observed [49]. As a result, authors assigned this process to Asp-loop movement since comparison of the crystal structures with reduced (which had $NADP^+$ in the binding site) and intact 147C-514C bridge showed significant displacement of this moiety.

Through in the last decade multiple papers were published in attempt to reveal the process of POR electron transfer, the exact mechanism of electron transfer to cytochrome specifying residues movements along the process and POR ability to differentiate between diverse cytochromes was yet to be explored.

As it has been demonstrated on the examples of Ras and POR, membrane proteins are challenging systems to study. One of the reasons is that they perform their function on the surface of the lipid bilayer, which requires one to consider diverse interactions protein experience that might affect their behavior.

In my project I demonstrate two approaches to investigate the complexity of membrane proteins. In the case of Ras protein dimerization, studies have been carried out on the lipid bilayer models mimicking native environment of the protein and possible interactions that it experience. But it has been pointed out that protein-protein interaction alone is the driving force of dimerization. Therefore, we plan to investigate protein-protein interaction separately on the model lacking lipid bilayer mimic to assess G-domain propensity to form dimers.

In the second part of the project, we plan to create an approach that will allow to investigate the most complex system with all possible interactions considered.

Number of studies has been performed on cytosolic portion of POR but successful studies of full-length protein, moreover in its reduced state are few in number. So the goal is to design an approach, which will make possible interrogation of conformational details and diverse interactions in a POR-nanodisc lipoprotein complex during its redox cycle.

II. METHODOLOGY

Nanodisc

Membrane proteins exist on a phase separation boundary, which makes them a challenging object to study, since lipids need to be included in the studies as well. Another thing to consider is an absence of a lipid bilayer leads to a significant decrease in protein stability. Furthermore, protein in a soluble state is more convenient to work with.

Originally detergents were utilized in protein solubilizations creating mixed micelles but application of detergents has a number of disadvantages. They can negatively affect protein stability, influence the results of assays, and interact with a substrates or buffer components. Moreover some membrane proteins require specific lipid composition or lipid domains to be active, and this cannot be achieved with detergent micelles [58].

Another membrane mimicking model that is widely used is the liposome. One of the greatest advantages of a liposome is that their lipid composition can be varied depending on the requirements of the experiment. One of the disadvantages of this model is an introduction of curvature into a lipid bilayer in the case of small liposomes that doesn't mimic native conditions in the cell. Another problem is that, due to size of liposomes, they cannot be used in certain techniques, such as NMR. Stability of the liposomes also poses a problem during the membrane protein studies.

More than a decade ago Sligar's group came up with a new membrane model called lipid nanodisc [59]. Lipid nanodisc is soluble complex of a lipid bilayer surrounded

by two molecules of a matrix scaffold protein obtained from apolipoprotein A1. Flat lipid bilayer serves as a perfect cell membrane model, while double-helix belt of MSP makes it soluble. The size of the lipid nanodisc can be varied depending on the length of amino acid sequence of MSP resulting in a range of diameters of the nanodisc. A series of nanodiscs were created with varying size, though it should be mentioned that the smaller nanodiscs are less stable compared to original obtained from MSP1D1 with a nanodisc size of 9.8 nm [60].

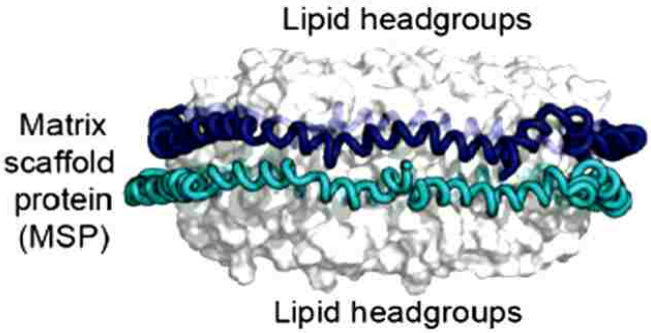

Figure 17. Structure of a lipid nanodisc. Two helix belts colored cyan and blue represents MSP protein that encapsulates lipid bilayer shown as white surface. Reprinted from [61].

One of the advantages of lipid nanodiscs is the ability to incorporate proteins in a monomeric state, thus providing data that reflects actual protein behavior, which is important for biochemical characterizations of the protein. For example, human cytochrome P450 3A4 on a nanodisc demonstrated higher cooperativity in testosterone binding compared to the data obtained using a detergent for solubilizations. Though at low protein concentrations, liposomes can also provide data characterizing monomer species but to obtain data of acceptable quality higher concentration needs to be used, this might create a problem in liposome studies. In the

case of a nanodisc, presence of only one protein unit per nanodisc surface can be ensured.

Moreover, active protein-protein complex can be created on the surface of the nanodisc as it was demonstrated by Denisov et al. with cytochrome P450 3A4 and NADPH cytochrome oxidoreductase [62]. The functional state of the complex was proven by measuring rates of testosterone hydroxylation in the presence and absence of NADPH. Unfortunately, the authors observed that 95% of the NADPH was consumed through non-productive pathways [63]. Despite that, the authors were able to determine that reaction rate increased by 40% in case of nanodisc with 30% 1-palmitoyl-2-oleoyl-*sn*-glycero-3-phospho-L-serine (POPS) and 70% 1-palmitoyl-2-oleoyl-sn-glycero-3-phosphocholine (POPC) lipid composition.

Nanodisc was also applied to study protein-lipid interactions of phosphatidylinositol (PI) binding proteins and lipid bilayer surface [64]. Using lipid composition of 1.25% PI, 98.75% 1,2-dioleoyl-*sn*-glycero-3-phosphotidylcholine (DOPC), dissociation constant for protein lipid complex was determined to be $K_d \sim 30nM$, which shows tighter binding compared to the one obtained previously with application of lipid micelles.

In a review[58] Bayburt et al. provided a number of examples of the successful application of lipid nanodiscs to study membrane proteins such as G-protein coupled receptors, cytochrome c, bacterial chemoreceptor, and receptors tyrosine kinases.

Finally, lipid nanodisc can be applied to study membrane proteins using solution NMR. This was demonstrated by Hagn et al. in his study of bacterial outer-membrane protein OmpX on 1,2-dimyristoyl-*sn*-glycero-3-phosphocholine (DMPC) nanodisc [60]. The authors evaluated the quality of the $^{1}H^{15}N$-TROSY (transverse relaxation

optimized spectroscopy) NMR spectra obtained from highly deuterated samples (both proteins and lipids) as a function of diameter of the lipid nanodisc (Figure 18).

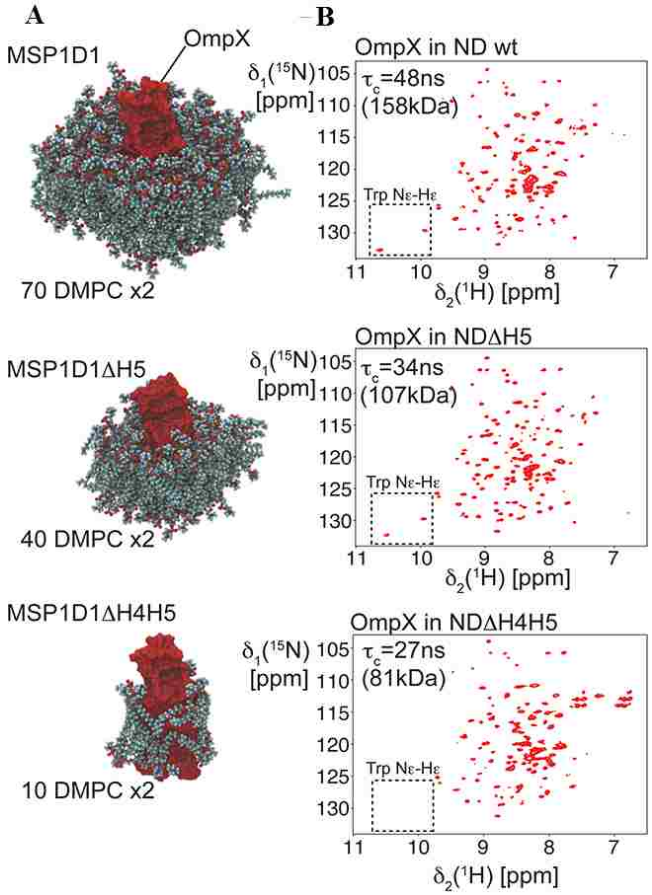

Figure 18. A. Model of OmpX protein (red) incorporated into nanodisc with the number of DMPC lipids (carbon, hydrogen and oxygen atoms colored green, white and red, respectively) per bilayer surrounding the protein. MSP is omitted for clarity. B. $^{1}H^{15}N$-TROSY spectra obtained for OmpX in nanodisc. Red dots correspond to signals from residues. Dotted square demonstrates region of tryptophan peaks. Reprinted from [60].

Nanodisc created with MSP1D1 ΔH4H5 that lacks two helices in a protein sequence can accommodate only 10 DMPC molecules serving as not very good lipid bilayer model. Also, ^{1}H-^{15}N cross-peaks of tryptophans were missing from the TROSY spectra of the protein; this was associated to the interaction of those residues with MSP, which lead to enhanced relaxation rates. In contrast, nanodisc obtained with

MSP1D1 ΔH5 provided a better quality of spectra due to a reduced size and, as consequence, faster rotational correlation time. It was concluded that deuteration of the lipid has a positive impact on NMR spectra quality, especially for the experiments with a side-chain coherence transfer. Hagn et al. confirmed the possibility of application of lipid nanodisc in NMR spectroscopy by providing first NMR structure solved of the membrane protein associated with the lipid nanodisc [60].

Solution Nuclear Magnetic Resonance.

Solution Nuclear Magnetic Resonance (NMR) spectroscopy has been one of the main techniques to study protein structure and dynamics for years due its ability to provide high resolution conformational information at conditions which resemble physiological ones. However classical solution NMR techniques can only be applied to the proteins with molecular weights up to 50kDa, which creates a challenge investigating membrane protein systems that require presence of lipid bilayer mimic. So, the question is, is there a NMR technique that will be suitable to study high-molecular weight systems while maintaining all unique strength of NMR spectroscopy?

The reason behind the inability to apply normal NMR techniques such as hetero nuclear single quantum coherence to a system with mass greater that 50kDa is a slow rotational diffusion of large protein molecules which gives rise to two processes that have a negative effect on the spectral quality:

- Chemical shift anisotropy.

  This effect arises due to anisotropy of electronic environment around each nucleus; in small protein due to high level of rotational freedom, the effect is averaged leaving single isotropic chemical shift value, but tumbling of a larger

molecule takes greater time which leads to different orientations of individual molecules with respect to external magnetic field. This effect leads to signal broadening due to a presence of a distribution of nucleus with different orientation to external magnetic field. It should be noted that this effect depends on the strength of the applied magnetic field.

- Dipolar coupling.

  Another effect that arises due to a slow rotational correlation time of the large proteins. It results from a presence of several nuclear spins in a close proximity to each other. Each of the nuclei has its own local magnetic field which either has additive or deductive effect to the strength of the external magnetic field applied to a neighboring nucleus. For the small molecules, due to a fast rotational freedom, total magnetic field that acts on a given nucleus is averaged. This effect is independent to an external magnetic field strength.

Pervushin in the paper [65] from 1997 presented a technique designed in a fashion that relaxation from chemical shift anisotropy at high magnetic field strength is canceled by the effect from dipolar coupling. Transverse relaxation optimized spectroscopy (TROSY) is capable to overcome the size-limiting problem of classical NMR techniques and it originally was applied to ^{15}N - ^{1}H spin pair to probe a protein backbone.

Methyl-TROSY

In 2003 Tugarinov et al. developed Methyl-TROSY technique [66, 67]. In this method, signal is obtained from labile methyl groups in the slow-tumbling protein. The principle of signal amplification is different from a classic TROSY approach that relies on the effect of inter-cancelation between chemical shift anisotropy and dipolar

coupling effects. Pulse sequence applied in Methyl-TROSY technique is the one used in heteronuclear multiple quantum coherence (HMQC) method, but due to the protein size, slow rotational correlation time and rapidly rotating methyl groups dipolar interactions from protons 2 and 3 in the methyl group are additive in case of outliners and they cancel out for the inner line. This effect is depicted on the multiple quantum coherence during HMQC obtained for sodium acetate and isoleucine-148 of malate synthatase G protein (80kDa protein) [68].

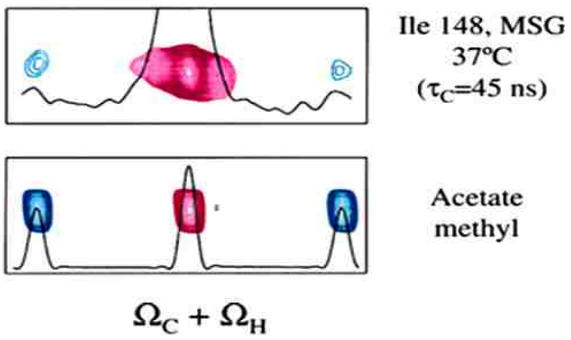

Figure 19. The effect Methyl-TROSY technique on a example of ^{13}C multiplet (red and blue counters) from methyl groups in ^{1}H-^{13}C double quantum correlation map in isoleucine (top) within the synthatase G protein and acetate methyl (bottom) in a solution. 1D proton dimension slices (black line) are overlapped with the two-dimensional spectra. Reprinted from [68].

In case of the methyl group from sodium acetate, triplet with relative intensities of the lines 1:2:1 is observed because of ^{1}H–^{13}C dipolar interactions in the absence of differential relaxation rates due to isotropic effect brought by fast rotational freedom of the small molecule. However, due to a local field effect for the methyl group of isoleucine-148 that is attached to macromolecule, relaxation rates for each line are different, because dipolar fields effect are additive for outliners (blue on the Figure 19, both spins of neighboring protons are up or down) and they cancel each other for inner line (red on the Figure 19) This effect underlies in Methyl-TROSY technique.

And Heteronuclear Multiple Quantum Coherence (HMQC) pulse sequence allows separating slowly relaxing methyl coherence from the fast ones. It should be noted that high levels of deuteration are critical for high TROSY effect. So, a special labeling technique that uses deuterated amino acid precursors carrying only one protonated ^{13}C methyl group are added to deuterated bacteria growth media prior to induction.

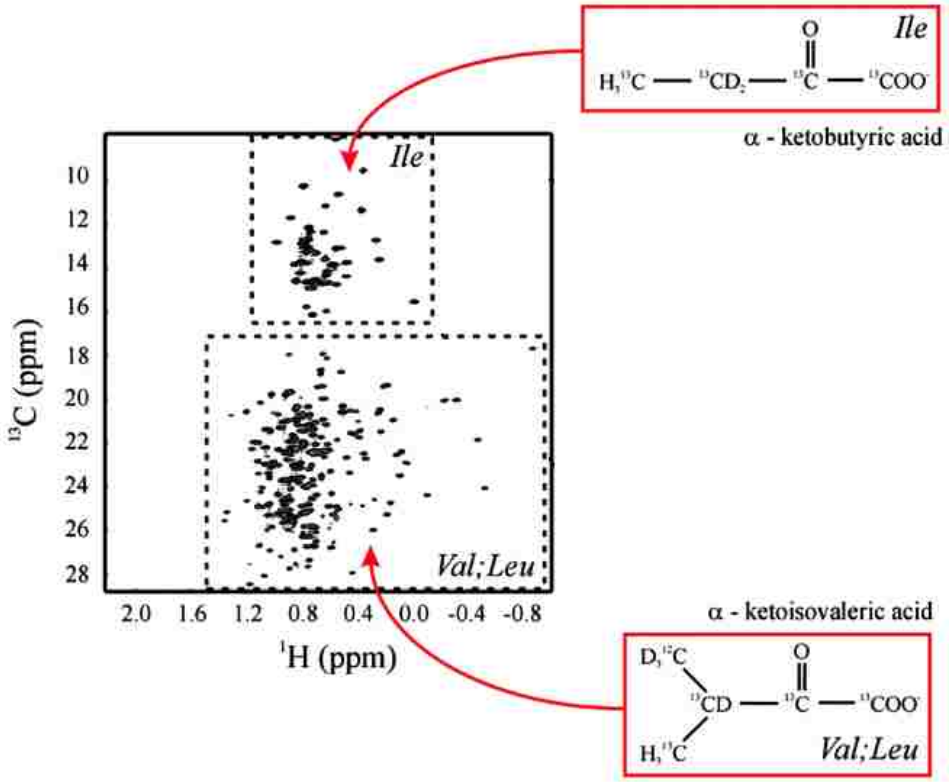

Figure 20. Location of the renounces from methyl-groups of valine, leucine and isoleucine in ^{1}H-^{13}C HMQC for non-uniformly labeled protein with ^{13}C, D-labeled precursors that were added during protein expression into the expression media. Reprinted from [68].

Figure 20 demonstrates the results obtained from Methyl-TROSY experiment with malate synthatase G using isoleucine, leucine and valine methyl groups to probe protein dynamics. In the study [68], α-ketoisovaleric acid was used as a precursor for

valine and leucine, while α-ketoisobutyric acid was utilized to label isoleucines. Signals were then assigned using set of $^{13}C_{aliphatic}$–$^{1}H_{methyl}$ and ^{13}CO–$^{1}H_{methy}$ TOCSY and original data from backbone assignment. To increase sensitivity of the assignment, a novel "out-and-back" approach was used in this work, where magnetization originating from methyl groups is being transferred to carbonyl carbons of the same residue and then back to the methyl from it is being detected.

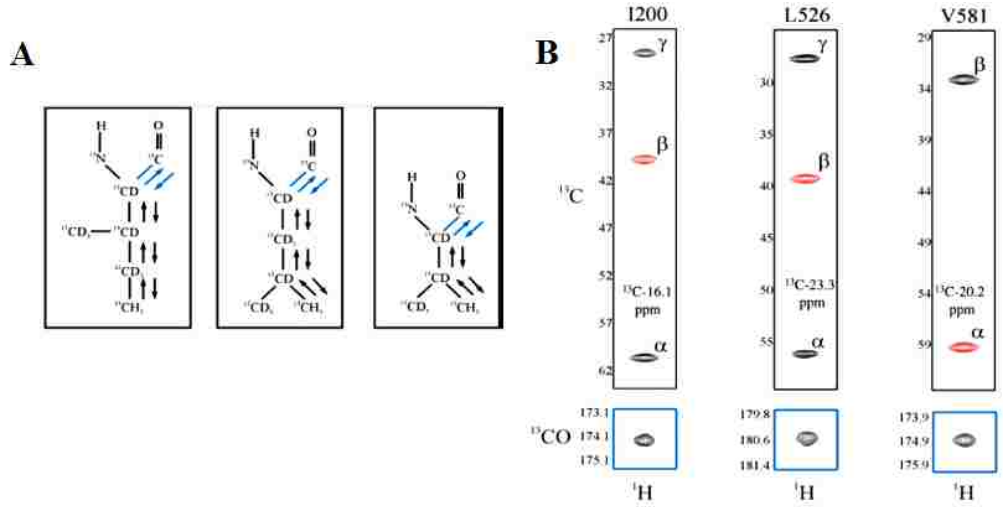

Figure 21. "Out-and-back" approach for a methyl groups assignment. A. The flow of magnetization in the residues, initiating from methyl going to carboxyl carbon and back. B. Strips from $^{13}C_{aliphatic}$–$^{1}H_{methyl}$ and ^{13}CO–$^{1}H_{methy}$ TOCSY are demonstrated for selected residues of malate synthatase G to show effectiveness of "out-and-back" approach. Reprinted from [68].

This approach allowed to assign 95% of isoleucine, 91% of leucine and 99% of valine methyl groups of the protein. Thus, authors demonstrated that Methyl-TROSY can indeed be applied to investigate protein dynamics and interactions for the high molecular weight systems which remained elusive for classical NMR techniques.

One of the examples of such systems is a complex formed between heat-shock protein ClpB, a major protein disaggregase in mitochondria of all eukaryotic cells, and DnaK chaperone. This bichaperone system assembly is required to recover proteins from

aggregates but, due to its size and dynamism of the interaction, structural features of this complex remained unknown. In 2013 Rosenzweig et al. [69] applied Methyl-TROSY to study interactions between 580kDa ClpB hexamer and 70kDa DnaK chaperone. In addition to valine, leucine and isoleucine, $^{13}CH_3$ methyl ε-groups of a methionine were used provide additional labels in the protein. Chemical shift perturbation analysis of NMR titration data with alternately $^{13}CH_3$ labeled ClpB hexamer and DnaK chaperone resulted in determination of the binding interface for both molecules. Moreover, the data was used to obtain the complex binding constant (K_d=25±3μM). Such low affinity value demonstrates the effectiveness of Methyl-TROSY technique in studying weak interactions between high-molecular weight systems.

Elimination of unneeded and misfolded proteins is one of the essential processes that are carried out in the living cells. The 20S CP archaeal proteasome is a barrel-like shaped protein which is responsible for selective degradation of damaged proteins. It consists of four heptameric units, $\alpha_7\beta_7\beta_7\alpha_7$, where α-subunit is responsible for interaction with effectors and provides a gate for substrate entry, while β-subunits create a central chamber that performs selective proteolysis. To determine dynamics and structural details of the 20S CP proteasome gate regulation, Religa et al. applied [70] Methyl-TROSY technique. The sample comprised of $^{13}CH_3$-methionine-labeled deuterated α-subunits and deuterated, unlabeled β-subunits of 20S CP proteosome was analyzed. Cross-peaks were assigned by creating single methionine-to-alanine mutations in 20S CP proteosome and comparing HMQC spectra of the mutant with the one obtained from the wild-type protein. Then, on the basis of the data obtained, the authors suggested that 20S CP proteasome exists in 3 states: major state (A) and

two minor states (B and C). Figure below demonstrates ^{1}H-^{13}C HMQC region of methionine residue introduced before N-termini methionine of wild-type sequence.

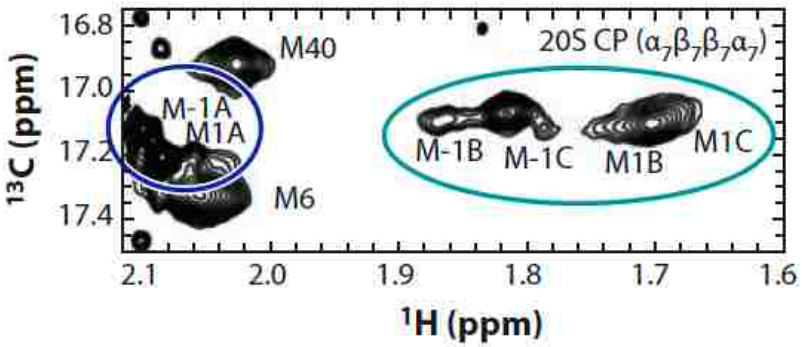

Figure 22. Methionine region of ^{1}H-^{13}C HMQC spectrum of wild-type 20S CP proteasome demonstrates peaks obtained from intrinsic (M1) and introduced by mutation (M-1) methionine residues of CP proteosome. Presence of several peaks from the same residue indicates equilibrium between several conformations. Reprinted from [70].

These states were later attributed to "in" and "out" state the N-termini residues of α-subunits. Additional analysis of HMQC spectra revealed that two out of seven N-termini of α-subunits exist in the "in" conformation, while five of them are in the "out" conformation, which demonstrates distinct conformations of the N-termini of each individual α-subunit, despite having the same protein sequence.

Finally, in 2011 Religa et al. published a paper where they demonstrated application of ^{13}C-methylsulfonylsulfanylmethane (^{13}C-MMTS) extrinsic labeling technique on α_7 ring of 20S CP archaeal proteasome [71]. ^{13}C-MMTS reacts with the exposed cysteines residues on the protein surface creating S-methylthiocysteine (MTC), methionine-like residues carrying $^{13}CH_3$ label.

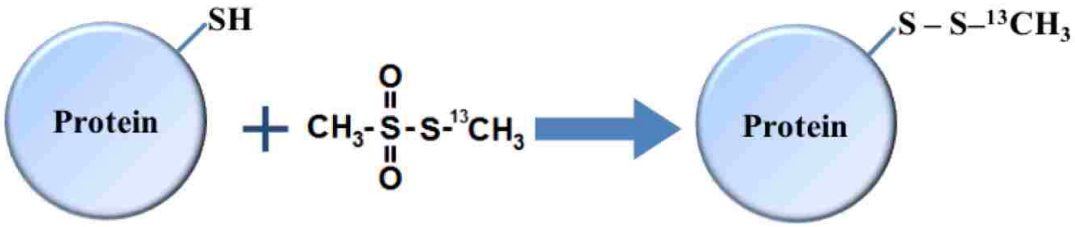

Figure 23. Labeling reaction with application of MMTS.

Using this labeling technique authors demonstrated that MTC-labels can be successfully used to probe conformation and dynamics of N-termini gating residues of 20S CP proteosome. As it was mentioned in the previous study they probed proteosome N-termini structure using artificially introduced methionine carrying $^{13}CH_3$ group at the beginning of the sequence. Religa et al. decided to check whether they will be able to obtain similar data by introducing MTC label at the same position while having other methionine labels untouched. Results of ^{1}H-^{13}C HMQC spectra comparison showed that that except for MTC label, peaks originating from other labels are superimposed, which indicates that label did not perturb chemical environment. Moreover, the pattern and population of the "in" and "out" states of the 20S CP proteosome N-termini were within 1% difference based on peaks obtained from ^{13}C-methionine and ^{13}C-MTC labels.

Thus, Methyl-TROSY with application of MMTS extrinsic labeling technique is sensitive instrument that can be used to probe protein dynamics of complex systems.

Paramagnetic Relaxation Enhancement

Effect of paramagnetism originates from unpaired electrons whose magnetic moment is three orders larger than that of protons; this phenomenon has found an application in nuclear magnetic resonance spectroscopy, remarkably this effect is evident at great

distances. Employment of paramagnetic labels at 2D NMR spectroscopy enables measurements of small paramagnetic effects on remote nuclear spins (spin-spin relaxation), effect appears as an increase of a peak line width due to increased transverse relaxation rates Γ_2 characterizing exponential signal decay. The effect from paramagnetic labels is measured by difference of transverse relaxation time at paramagnetic and diamagnetic conditions

Taking into account that total spin magnetization vector M of a spin in a presence of external magnetic field can be represented having two components: M_z (parallel to a external magnetic field which is conventionally oriented along the z-axis) and M_{xy}; change of the transverse magnetization with time can be described with the following equation:

$$M_{xy}(t) = M_{xy}(0)e^{-t/T_2}$$

, where $M_{xy}(0)$ – is initial magnetization in transverse plane; t – time and T_2 – transverse relaxation time ($1/\Gamma_2$). It should be emphasized that effect does not occur due to a change of orientation of a vector of magnetization, but because of dephasing.

Paramagnetic Relaxation Enhancement (PRE) was first observed by Solomon and Bloembergen in their work from 1950s [72]. In last decade PRE became increasingly popular method that provide long-range distances restraints which can be used to compliment NOE restraints., especially in studies of membrane proteins[73, 74]. PRE allows probing distance from 10 to 28 Å depending on the paramagnetic group used.

Two main mechanisms contribute to PRE: Solomon mechanism [72] and Curie spin mechanism [75]. Curie mechanism is predominant in cases when rotational diffusion (associated with nuclear relaxation) of the molecule is much slower compared to electron relaxation rates.

In Curie mechanism spins can be described by isotropic magnetic susceptibility χ_{iso}. Curie spin relaxation mechanism at high magnetic fields for slowly tumbling macromolecules can be represented by equation [76]:

$$\Gamma_2 = \frac{\gamma^2 B_0^2 \chi_{iso} \tau_c}{20\pi^2 r^6}$$

, where B_0 – external magnetic field strength; r is a distance between paramagnetic center and nuclear spin; γ is the nuclear gyromagnetic ratio; τ_c – molecular correlation time due to rotational freedom. For systems with rapidly relaxing electronic spins at high magnetic fields, transverse relaxation is predominantly due to Curie mechanism.

Solomon relaxation mechanism considers relaxation driven by limited electronic spin state lifetime and is the mechanism of relaxation for slowly tumbling molecules with a long electron spin states lifetimes. In 2000, Wagner et al proposed modified equation for biomolecular NMR for species relaxing predominantly by Solomon relaxation mechanism [77].

$$r = \left[\frac{K}{\Gamma_2}\left(4\tau_c + \frac{3\tau_c}{1+\omega_H^2\tau_c^2}\right)\right]^{1/6}$$

, where Γ_2 – transverse relaxation rate (determined by measuring signal broadening, specifically width of the peak at half-height); τ_c – molecular correlation time due to rotational freedom; ω- Larmour frequency of a nuclear spin (index H- stands for the proton in this case) at correspondence with the strength of external magnetic field; K is calculated as

$$K = \frac{1}{15} S(S+1)\gamma^2 g^2 \beta^2$$

, where γ is the nuclear gyromagnetic ratio, *g* is the electronic *g* factor, and β is the Bohr magneton. For calculating distances, the approximation was made that τ_c was equal to the global correlation time of the protein.

Recently, application of the Gd^{3+} labels became particularly popular; this can be explained by a nature of this paramagnetic label. Effect from the single paramagnetic center can be described using magnetic susceptibility tensor at three principle axis χ_x, χ_y, χ_z. If magnetic moment of paramagnetic center is different at three principles axis magnetic tensor χ is anisotropic it gives a rise to number of additional effects that needs to be considered such as pseudo-contacts shifts. Gd^{3+} ion has an isotropic magnetic tensor χ. Another positive trait of this ion is that its unpaired electron spins relax relatively slowly on the order of 10^{-8}s [78] given facts determines predominantly Solomon relaxation mechanism for Gd^{3+} ions, which are insensitive to cross-correlation between chemical shift anisotropy and dipolar shift anisotropy, which in turn facilitates data interpretation.

Liu and colleagues [79] applied residue specific PRE derived distance restraints together with chemical shift perturbation data to determine yeast Arf1 (Rho family GTPase-activating protein involved in the control of F-actin dynamics at the Golgi) interaction surface with Fapp1-PH on the membrane model of DOPC micelles using molecular docking software (HADDOCK).

Another example of application of nitroxide-spin labels was demonstrated by Rosenzweig et al. to determine binding interface between ClpB-DnaK complex [69]. The distances were measured between nitroxide-spin labels attached to ClpB and $^{13}C^{1}H_3$ methyl groups of methionine, leucine, isoleucine, and valine from DnaK (Figure 24).

The distance restraints obtained were used by molecular docking software (HADDOCK) to obtain structural model of the complex. Interestingly, the binding interface of DnaK determined from molecular docking, also being targeted by DnaK

cochaperon GrpE, and additional experiments revealed that ClpB and GrpE compete for DnaK binding.

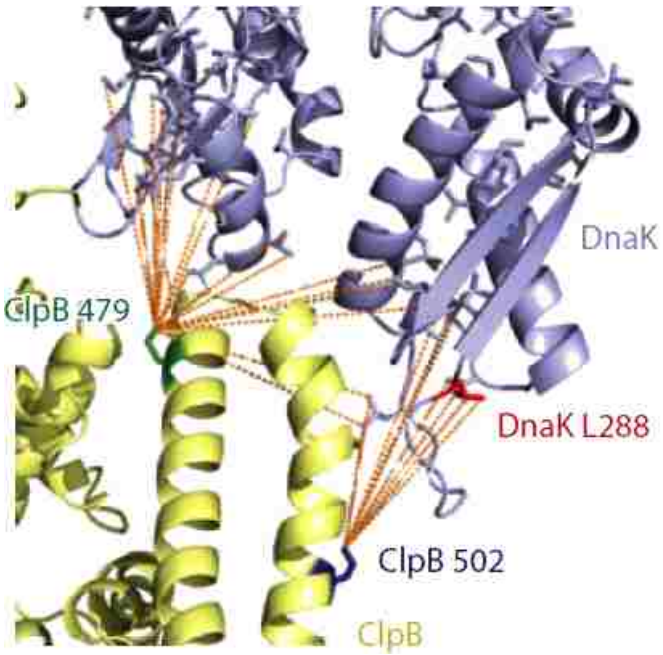

Figure 24. PRE distance measurements obtained from spin-labels for ClpB-DnaK complex.
Position of the labels: ClpB-479 (green); ClpB-502 (slate blue); DnaK-288 (red). Orange lines correspond to distances restraints obtained. Reprinted from [69].

It was demonstrated by Ikura's group [80] that solution NMR with application of paramagnetic labels might be applied to study proteins attached to nanodisc. Sample of Rheb protein, one of the member of Ras GTPases superfamily, was created attached to a 1,2-Dioleoyl-sn-glycero-3-phosphotidylcholine (DOPC) lipid nanodisc to study it's dynamics on the lipid bilayer by solution NMR. Using distance restraints obtained from membrane carrying gadolinium salt of 1,2-distearoyl-*sn*-glycero-3-phosphoethanolamine-N-diethylenetriaminepentaacetic acid (18:0 PE-DTPA (Gd)) paramagnetic label information on preferred orientation on the lipid surface was extracted depending on the nucleotide state of the protein.

Authors represented the PRE data obtained from $^{1}H - ^{15}N$ Rheb detected for each residues of GDP- (red) and GTP- (black) loaded states of Rheb as a ratio of resonance intensities obtained in paramagnetic (I*) and diamagnetic (I_0) conditions. Distance restraints obtained from this data were used in molecular docking software (HADDOCK) to evaluate conformation changes of a protein on lipid bilayer.

As final result, authors proposed a model of Rheb protein interaction with the lipid bilayer, where membrane acts as regulator, in Rheb with mTORC1 (Rheb effector). In addition to this it was suggested that membrane effect is correlated with GTPase cycle of a protein.

Fluorescence

Fluorescence techniques have proved to be a popular method in biochemistry. Presence of intrinsic fluorophore, such as tyrosine or tryptophan, in amino acid sequence of a protein, allows for the analysis of a protein in a native state. Though, in most cases, introduction of extrinsic fluorescent labels is required, and a great number of fluorophores are available in the field. The main advantage of the method is its great sensitivity; therefore, the amount of protein used in an experiment is small compared to other techniques. Currently, a number of techniques exist that are applied to study protein dynamics; fluorescence anisotropy is one of them.

Protein attached to a lipid bilayer can behave differently: it can be freely rotating or it can actually lie on the surface. Of course, the position of the protein will change its rotational correlation time. To address this property, we can label the protein with fluorophore and detect changes that the protein undergoes by detecting changes of fluorescence. One of such indicators is fluorescence anisotropy.

Fluorescence anisotropy principles

Fluorescence anisotropy measurements utilize the principle that a fluorophore preferably absorbs a photon, which has its electric vector aligned parallel to a transition moment of the fluorophore. Moreover, the photon emitted by a fluorophore will be polarized as well. But before emission from a fluorophore can occur it will take some time. During this time, the fluorophore will rearrange itself in solution due to its rotational freedom. This process will result in a fact that polarization of the emitted light will be changed by a displacement of the molecule in solution, so that the transition moment of the resulting emission that will no longer be parallel to the original polarization of the absorbed photon [81].

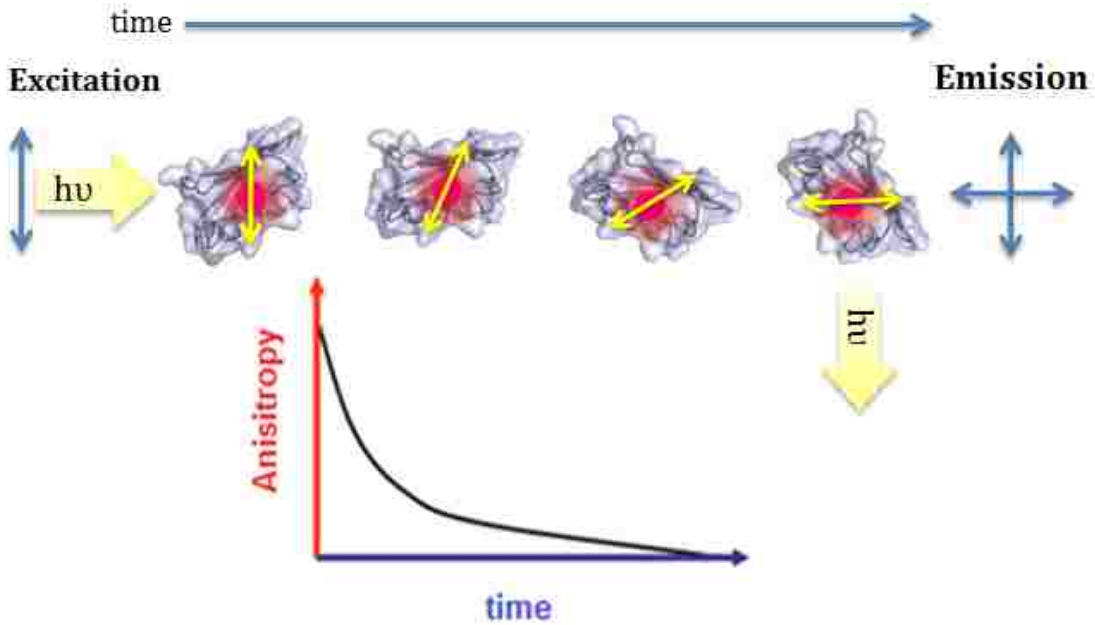

Figure 25. Schematic representation of the principle of polarization anisotropy measurements. Blue arrow represents polarized light either absorbed or emitted by a fluorophore. Yellow double arrow represents electric vector of polarized excitation of the fluorophore (magenta) within the protein (slate blue cartoon) and its evolution during the time. Lower panel demonstrates change of anisotropy as a function of time.

Polarization anisotropy – noted as r, is a measure of ratio between polarized light to overall intensity and calculated as follows

$$r = \frac{I_{VV} - GI_{VH}}{I_{VV} + 2GI_{VH}}$$

,where I_{VV} and I_{VH} are corresponding intensities of vertically and horizontally polarized emissions obtained from the sample excited with vertically polarized light [81]. While G-factor is the instrument sensitivity factor to differently polarized light, and is calculated as follows,

$$G = \frac{I_{HV}}{I_{HH}}$$

Polarization anisotropy is not a constant value; it decays with time. There are two reasons for that: first, intensity decays with the time due to a fluorescence lifetime of a fluorophore, second, due to a rotational freedom of the molecule.

Anisotropy decay follows exponential rules and can be fitted using exponential equation. Equation below is given for the species with several rotational correlation times θ, g_i – is weighted factor of each individual rotational correlation time and r_0 - is zero-time (initial) anisotropy [81]. Generally, number of rotational-correlation times determined during an experiment cannot exceed 3.

$$r(t) = r_0 \sum_{i=1}^{n} g_i \exp\left(-{}^{t}/_{\theta}\right)$$

This data can be used to calculate rotational correlation time of the molecule using Stokes–Einstein–Sutherland equation (below) to assess protein mobility and dynamics.

$$\theta = \frac{k_B T}{6\pi\eta R}$$

,where η is viscosity of the media, R – hydrodynamic radius of a protein, k_B – Boltzmann's constant and T is an absolute temperature in Kelvin [81].

It should be mentioned that fluorescence anisotropy measurements are depended on fluorescence lifetime τ – time molecule spends in an excited state before returning to a ground state level. The life-time of fluorescence should be comparable to rotational correlation time.

Application of polarization anisotropy measurements

Since peripheral membrane proteins are flexibly attached to a lipid bilayer surface, polarization anisotropy measurement is perfect tool to evaluate protein dynamics in proximity of a membrane.

To assess G-domain mobility on the membrane surface, semi-synthetic K-Ras4B and N-Ras GTPases rotational freedom of the molecules were studied as a function of lipid bilayer composition [82]. LUV and GUV were used as membrane models. Rotational correlation time of the samples was measured using chemically attached N-hydroxisuccinimide-modified BODIPY fluorophore (excitation λ = 473nm; emission λ = 505nm) to the lysine on the G-domain surface.

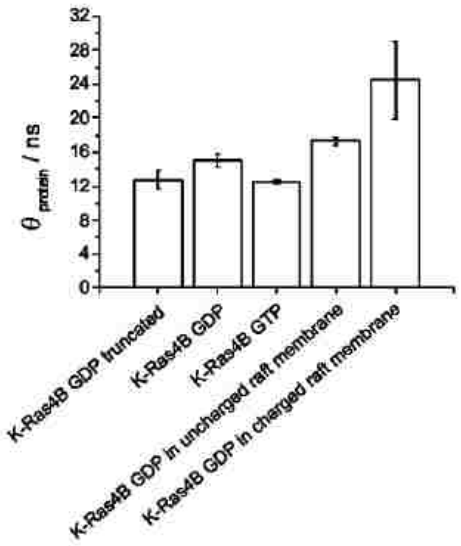

Figure 26. Rotational correlation times of semi-synthetic K-Ras. Reprinted from [82].

Semi-synthetic K-Ras4B was unaffected by the attachment of a lipid anchor in a bulk solution which was monitored by very small increase of rotational correlation time which is in within experimental error. Surprisingly, in the presence of uncharged lipid bilayer, rotational freedom of the G-domain did not decrease a lot compared to the free molecule in the solution. While in case of K-Ras4B attached to a charged raft-like lipid bilayer, G-domain significant increase of rotational correlation time was observed. This observation can be explained by the fact that K-Ras4B anchor region has six lysine residues, which create a significant positive charge in this part of the molecule. Negatively charged lipid rafts introduced in the last experiment created an additional mode interaction between protein and a lipid head groups leading to a better protein association with a lipid bilayer.

Interestingly, in the case of semi-synthetic N-Ras, which has two lipid anchors, a high level of association was observed already in the case of fluid membrane, which was monitored by 2-fold increase in rotational correlation time. No significant changes were seen in case of lipid rafts model. Slow rotational correlation time of a semi-

synthetic full-length N-Ras in a bulk solution was due to presence of two lipid anchors, which were driven together by hydrophobic effect. In K-Ras case this was not observed because of the repulsion of positively charged anchor regions of HVR.

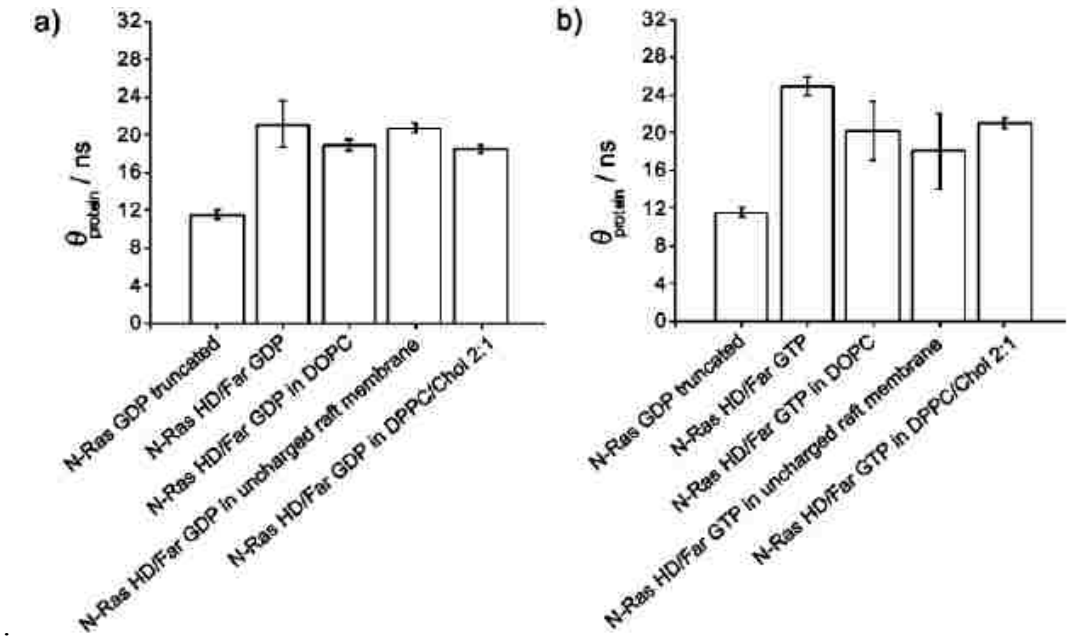

Figure 27. Rotational correlation times of semi-synthetic N-Ras in GDP (a) and GTP (b) bound states. Reprinted from [82].

Results presented in the paper demonstrate that polarization anisotropy measurements can be successfully applied to evaluate degree of association of peripheral membrane protein and lipid bilayer.

III. RESULTS AND DISCUSSION.

Membrane proteins play a vital role in a cell, serving as receptors, transporters and enzymes of high efficiency due to a high local concentration provided by a membrane coupling. The term itself points out the importance of the lipid bilayer for these biomolecules functions. At the same time, existence on the phase separation boundary makes them a complex system to study. Functions of membrane proteins depend on diverse interactions they experience on a membrane (Figure 28):

- Interaction with the lipid bilayer and correlation with its composition;
- Interaction with the small molecules present in the cytosol (signaling molecules, cofactors etc.);
- Dependence on the buffer properties such as pH, ionic strength etc.;
- Interaction with other proteins (downstream effectors, electron-transfer partners etc.);

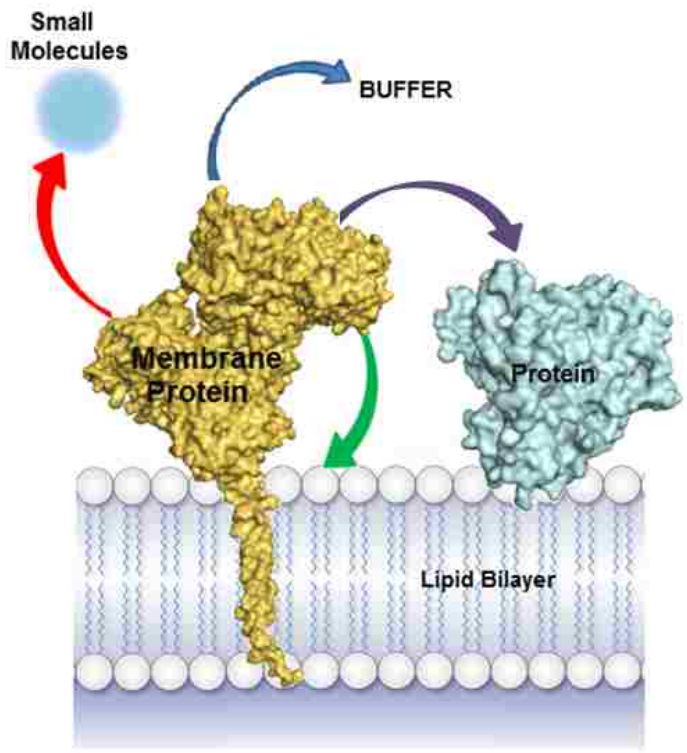

Figure 28. Interactions experienced by a membrane protein on a lipid bilayer.

Aforementioned facts create a challenge in an investigation of membrane proteins. The general approach that's going to be applied in our research is to address each interaction pattern separately to unambiguously determine the level of influence from each of them.

Two alternative research projects are outlined below. In the case of investigating propensity of Ras molecules to dimerization we plan to investigate protein-protein interactions separately. This will be done to determine whether it is a driving force of protein dimerization as it was suggested or presence of the lipid bilayer is required. For the part of the project that interrogates POR conformation changes during its redox cycle, we plan to develop a technique that will allow as to investigate complex lipoprotein system of POR associated with lipid nanodisc as a whole while altering different interactions in the system to determine their role in protein functions.

Project 1. Ras protein-protein interaction.

H-Ras stability at a different pH conditions.

In our study, we investigated Ras proteins in a solution and before we do that we need to determine what pH conditions to consider. Fluorescence anisotropy studies may require long acquisition time, which means stability of the sample is one of the major requirements of the experiment. More so, we also need to confirm that introduction of Mant-GDP fluorophore will not affect protein stability. To establish condition when the protein is the most stable, we explored H-Ras stability under different buffer conditions. To evaluate Ras G-domain stability we carried out fluorescence anisotropy thermal shift assay experiments involving buffers in pH 6-8 range. Since HVR is unstructured in a Ras protein, stability of the G-domain alone was studied. H-Ras C118S 1-166 protein was used as G-domain model. Buffer composition used in

the studies is shown in the table below. Sodium azide was used as biocide to preserve protein samples. Buffer 2 corresponds to the native cytosolic conditions.

Table 3. Buffer composition used in thermal shift assay.

Buffer 1	**Buffer2**	**Buffer 3**
MES pH=6.0 20mM	HEPES pH=7.2 20mM	TRIS pH=8.0 20mM
NaCl 150mM	NaCl 150mM	NaCl 150mM
DTT 1mM	DTT 1mM	DTT 1mM
NaN_3 1.5mM	NaN_3 1.5mM	NaN_3 1.5mM
$MgCl_2$ 1mM	$MgCl_2$ 1mM	$MgCl_2$ 1mM

In the thermal shift assay, stability of the protein is determined by melting temperature or denaturation midpoint T_m – temperature at which concentration of unfolded protein is equal to a folded one. Since Ras proteins are GTPases we applied MANT-GDP (excitation wavelength 360nm; emission wavelength 440nm) fluorescence label to monitor protein unfolding by anisotropy decay. Bound MANT-GDP will have rotation correlation time of the Ras protein in folded state. But then, as the protein unfolds, the fluorescent label is freed which leads to an increased rotational freedom and, as consequence, a decreased anisotropy value.

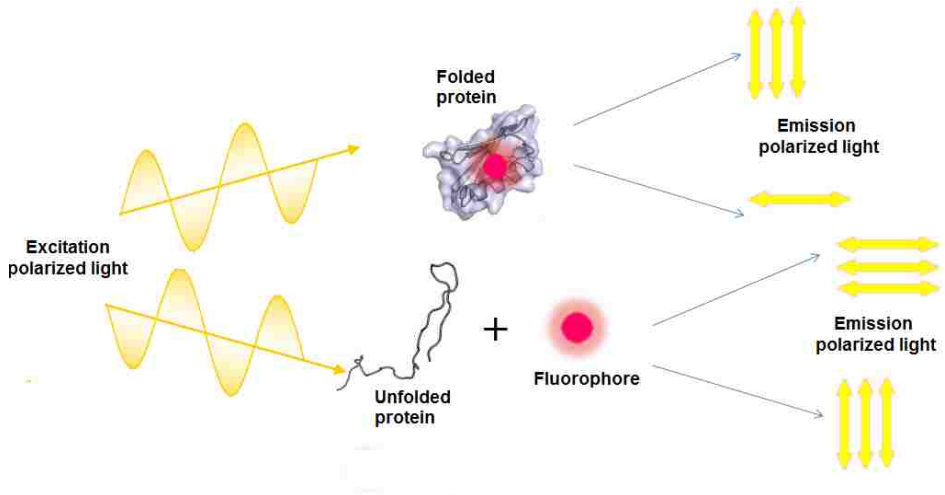

Figure 29. Schematic representation of the experiment design to evaluate G-domain stability.

H-Ras was subjected to nucleotide exchange from GDP to Mant-GDP [83]. Ras concentration after nucleotide exchange protocol was 10μM. To make sure that sample did not have any residual free Mant-GDP, the sample underwent size-exclusion chromatography using NAP5 column packed with G25 resin. Originally prepared sample was diluted 10-fold in the appropriate buffers. To demonstrate sample integrity, 2D fluorescence spectra was taken. On the Figure Figure 30 below simultaneous presence of two peaks corresponding to intrinsic Tyrosines (excitation 280nm/ emission 320nm) and Mant fluorescence (excitation 360nm/ emission 440nm) serves a proof of successful labeling.

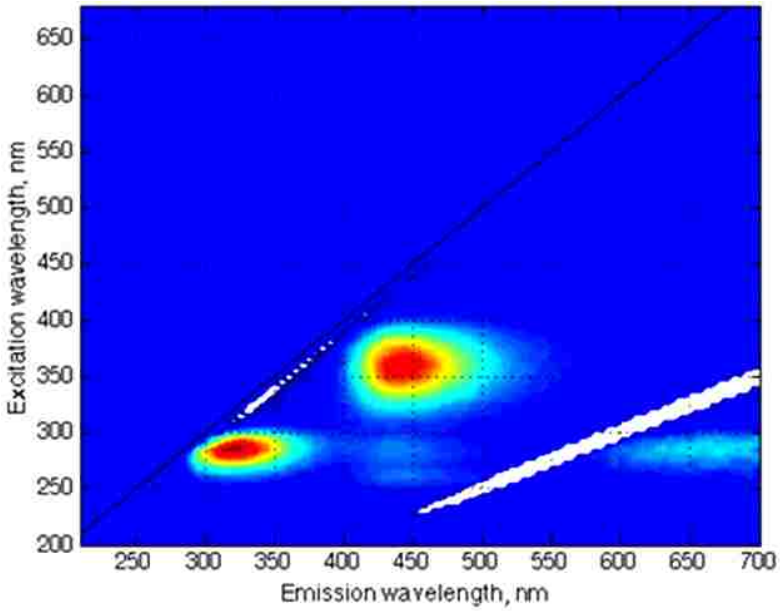

Figure 30. 2D spectra of a MANT-labeled H-Ras C118S -166 sample at pH 7.2 buffer

Temperature-dependent anisotropy profiles were recorded to obtain melting temperature T_m. As we expected the greatest stability was observed in the second buffer, which corresponds to cytosolic conditions of Ras. Data analysis resulted that change of the pH has destabilizing effect on G-domain; noticeably increase of the pH has less severe effect on H-Ras stability than increase of buffer acidity.

Table 4. Denaturation midpoints obtained for the H-Ras C118S 1-166 at pH 6.0-8.0

Buffer pH value	pH 6.0	pH 7.2	pH 8.0
Denaturation midpoint(T_m)	46.6 C	50.2 C	49.5 C

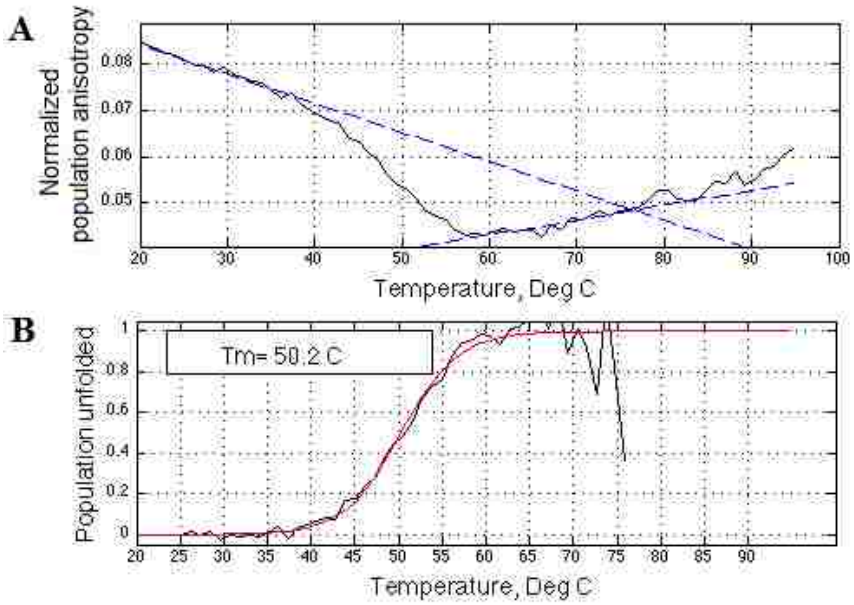

Figure 31. A. Normalized anisotropy MANT-labeled H-Ras C118S 1-166 sample at pH 7.2 buffer of the sample. Blue lines demonstrate linear regions selected for fitting. B. Denaturation curve of MANT-labeled H-Ras C118S 1-166 sample at pH 7.2 buffer of the sample. Red line represents fitted curve.

Propensity of G-Domain to form dimers.

Ras and its homologs function strictly as monomers in contrast to the mechanism of GADs (GTPases Activated by Dimerization) [84, 85]. In solution, dimerization of the Ras G domain (lacking C-terminal tail and lipidation) has never been reported; yet, in the past decade, several papers have been published that were discussing the ability of Ras molecules to form dimers through formation of salt bridges between two G-domains [34] [35]. It was stated that this fact may play a significant role in Ras-MAPK signal transduction pathway where one of the Ras downstream effectors Raf-1 can be activated by Ras dimerization [30].

The earliest proposal that Ras functions at the membrane in an oligomeric form came from observations of radiation inactivation (target size analysis) [86] . In the later cross-linking study by Inouye and others, Ras dimers were proposed to form on

liposomes and facilitate activation of Ras effector Raf-1 [30].

In both reports [34] [35], the membrane is thought to play a passive role of diffusional restraint—preventing translational diffusion in the direction normal to the membrane plane and increasing local concentration of the G domains. If this hypothesis is correct, one should be able to stimulate formation of Ras dimers by merely sequestering G domains close enough in space to remove the entropic penalty of translational diffusion of individual Ras molecules on the membrane.

Ability of Ras to form dimers on membrane surface would result in a different interpretation of the data on Ras mobility and functions on the lipid bilayer. In the following experiment, we evaluated the ability of the G-domain to form dimers utilizing fluorescence time-domain measurements. Since the presence of dimers will result in slower rotational freedom due to a doubled molecular mass of the species, we applied fluorescence anisotropy decay measurements to determine rotational correlation times.

To increase G-domain ability to form dimers, it was decided to use bis-maleimido linkers of a flexible length to increase local concentration. 1,8-bismaleimido-diethyleneglycol ($BM(PEG)_2$) (length 1.5nm) and 1,8-bismaleimido-undecoethyleneglycol ($BM(PEG)_{11}$) (length 5nm) were applied in this study to create an irreversible linkage between two Ras molecules carrying C-terminal cysteines. For clarity, in a further discussion conjugates will be referred to as Ras-11-Ras and Ras-2-Ras obtained in reaction of H-Ras C118S 1-181 with $BM(PEG)_{11}$ and $BM(PEG)_2$, respectively.

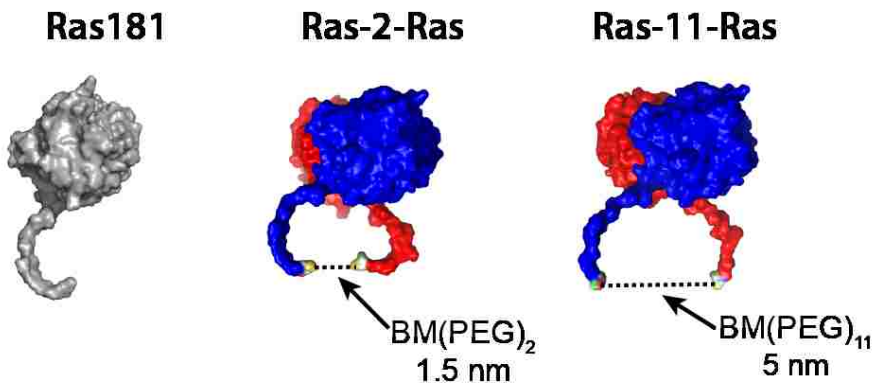

Figure 32. Protein models utilized in the study of Ras dimerization. Ras181, the cytosolic portion of the full-length H-Ras1-181; Ras-2- Ras and Ras-11-Ras, the inverted-tandem conjugates of two Ras181 molecules. The drawing is based on PDB ID 5P21 (residues 1-166; "crystallographic dimer") and 1Q21 (residues 1-171; no dimers). To create the full-length model of the "crystallographic dimer", two 1Q21 structures were aligned to the dimeric structure from 5P21. The unstructured C-terminal peptides, residues 172-181, were added to 1Q21 in Pymol and modeled in conformations to show that there are no steric restrictions to form the dimeric structure with either 1.5 or 5 nm linkages between C-terminal cysteines. The $BM(PEG)_n$ linkers are schematically shown with dashed lines.

To create high local concentration of the G domain, we tethered two Ras 1-181 proteins through their Cys181 side chains using the bis-maleimido crosslinkers $BM(PEG)_2$ and $BM(PEG)_{11}$ (producing "Ras-2-Ras" and "Ras-11-Ras" constructs, respectively). The resulting inverted-tandem conjugates restrict a pair of G domains in the close proximity of each other connected by a flexible unstructured chain comprising the residues 173-181 of two Ras181 molecules and the crosslinker. The C-termini of the two G domains in the "crystallographic dimer" are oriented in a V-shaped fashion towards one side of the dimer. The Ras-Ras conjugates with both 1.5 nm and 5 nm linker lengths allow for the "crystallographic" dimer conformation as well as other possible interaction modes. The linkage of cysteine side chains with bis-maleimide cross-linkers is irreversible[87].

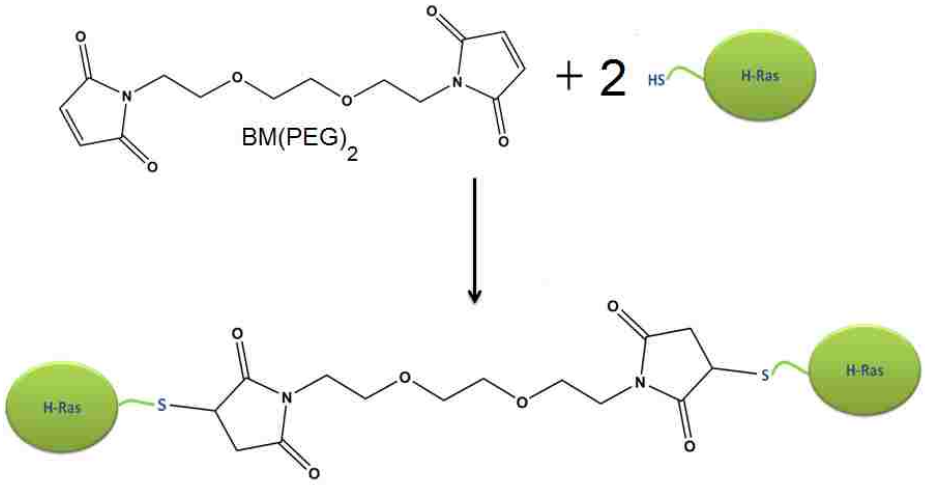

Figure 33. Demonstration of cross-linking of two Ras molecules using $BM(PEG)_2$.

Cross-linked conjugates were purified by size exclusion chromatography using Ultragel Aca54 XK16/40 column to assure sample purity see Figure 34.

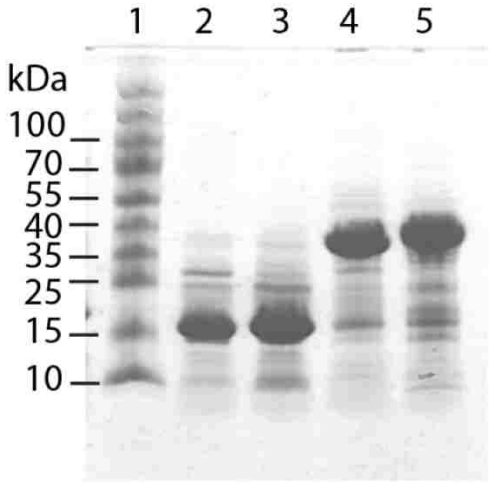

Figure 34. Purity of the samples analyzed with SDS-PAGE.
Lane 1, PageRuler Prestained Protein Ladder; lane 2, first preparation H-Ras C118S 1-181;
lane 3, second preparation H-Ras C118S 1-181; lane 4, Ras-2-Ras sample; lane 5, Ras-11-Ras sample.

Relative protein concentration determined by Bradford assay was 16µM for H-Ras C118S 1-181; 12µM for Ras-2-Ras and 18µM for Ras-11-Ras. Low protein

concentration was used in this study to assure presence of monomer species for H-Ras C118S 1-181 proteins for correct data comparison.

Each construct was tested under three temperatures (20°C, 25°C and 37°C) and in a three buffers of different ionic strengths. Ionic strength was changed by varying NaCl concentration from 0-300 mM. Since increased ionic strength has a destabilizing effect on the salt bridges we planned to see change of the rotational correlation times throughout the experiment in case.

As fluorescent label, we utilized Mant-GDP (excitation wavelength = 360nm; emission wavelength = 440nm) fluorophore that performs two tasks: small Mant group eliminates the possibility of fluorophore-driven self-association and additionally serves as GDP mimic. GDP mimic was utilized because dimerization was observed in GDP state in the original paper [34] by Guldenhaupt et al. Fluorescence anisotropy decay data was fitted using AniFit software (shared by Søren Preus; www.fluortools.com). We investigated only GDP-bound state of the protein since, in previous studies, dimerization was reported for GDP state of the protein [34].

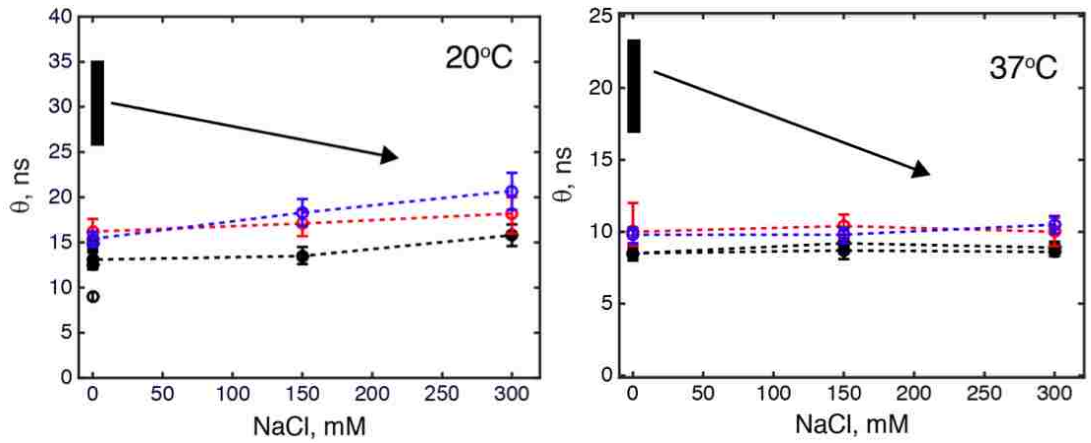

Figure 35. H-Ras rotational correlation time dependence on ionic strength of the buffer and temperature. Black bar represent expected θ of the Ras dimer. Black arrow demonstrates expected trend from increasing buffer ionic strength. Red series are

represent Ras-2-Ras data; Blue – Ras-11-Ras; Black corresponds to H-Ras C118S 1-181;

We noted that G-domain rotational freedom was practically unaffected by conjugation demonstrating that two G-domains tumble independently in a solution from each other [29]. We were expecting 2-2.7 -fold increase of rotation correlation time if the dimer species were present in the samples.

One would expect the rotational correlation time of the G domain in Ras conjugates to be greatest at the low salt concentration (due to enhanced stability of G domain dimers) and to gradually reduce with increasing ionic strength (due to a gradual shift of populations towards dissociated independently-tumbling G domains in Ras conjugates). But the results demonstrate that there is no decrease of rotational correlation time due to destabilization effect of the increasing ionic strength of the buffer on salt-bridges that provide the basis for dimer formation.

Generally expected trend is depicted as black arrow. We attribute small increase in θ at 20°C to an increased size of the solvation shell of the protein at higher salt concentrations.

In conclusion, based on our results we propose that G-domain alone is unable to form dimers through protein-protein interactions at physiological conditions independently of ionic strength. Thus, in our future experiments, where we will investigate protein tethered to a lipid bilayer, we do not need to worry that spatial proximity at the membrane surface may induce dimer formation. So, all changes in rotational freedom observed in future experiments will be due to presence of the lipid bilayer or protein lipid anchor region.

Recent publication by Groves et al. [88] demonstrated that Ras protein does not dimerize regardless of the nucleotide bound state, presence of the lipid bilayer and its

composition. These results demonstrates that in the future experiments interrogating Ras protein-protein, protein-lipid interactions and overall function on the surface of the lipid bilayer we can analyze data assuming it acts as a monomer on the membrane.

Project 2. POR dynamic interaction with lipid bilayer.

NADPH-cytochrome P450 reductase

POR plays a key role in mediating electron transfer to diverse cytochromes P450, known to be involved in vital processes in the organism such as drug, toxins and hormone metabolisms. It is noteworthy that, in humans, single POR provides electrons to forty-eight microsomal cytochrome P450[41] . Consequently, alteration of POR activity in living cells can lead to severe disease, identified as a POR Deficiency Syndrome. The disease symptoms are similar to Antley-Bixler Syndrome (ABS) which include: skeletal structure malformations (mainly affecting head), fusion of adjacent bones, bowing thigh bones, joints permanently flexed or extended, etc. But unlike ABS POR Deficiency Syndrome, it also involves symptoms related to steroid hormone metabolism, such as ambiguous genitalia. Due to the fact that ABS is related to mutations in *Fibroblast growth factor receptor 2*, thus a cause of the disease is different while symptoms are alike. In the literature, POR deficiency can be indicated as a specific case of ABS or another syndrome.

The electron transfer model of POR (Fig.1) based on the X-ray diffraction studies of the cytosolic region [41] (using a construct lacking 56 N-terminal residues —"Δ56 POR" in the following text) requires conformational exchange between two states of a molecule: a "closed" conformation which allows ET from NADPH to flavins and an open conformation to transfer electrons from FMN to cytochrome P450 and other ET

partners. Structural details of this process though are yet to be revealed. It should be noted that mammalian POR can only perform its function while being attached to the lipid bilayer which requires presence of a lipid bilayer mimic in an experiment, increasing the size of the system. The fact that the cytosolic portion of POR can interact with the non-native ET partner cytochrome c implies that presence of a lipid bilayer is not simply a local concentration effect. Liu and coworkers recently reported that activity of POR and coupling in POR-P450 complex in nanodiscs are enhanced when nanodiscs are made with the natural lipid preparations extracted from endoplasmic reticulum (ER) compared to the synthetic lipid mixtures mimicking ER composition[89]. This finding indicates that POR makes specific protein-lipid interactions modulating enzymatic activity of POR.

Moreover, a number of clinical studies reported on mutations that disrupt interaction with the specific isoform of cytochrome P450 while not affecting the others [90, 91]. The reason for how POR differentiates between different P450 has been elusive and we suggest that protein-lipid interaction between POR and lipid bilayer can be one of the factors.

Another challenge arises from the presence of an unpaired electron during ET cycle which leads to paramagnetic relaxation of signals which renders conventional techniques incapable to sense structural details.

Vincent et al. extensively characterized the conformational state of the isolated cytosolic portion of the protein, Δ56 POR, in its oxidized state but did not report any measurements on the reduced samples [92]. Interactions of a similar soluble construct Δ66 POR with heme oxygenase was also documented by NMR in the oxidized state [93] as well as interaction of the isolated FMN-binding domain with the cytochrome *c*

[94] and cytochrome P450 17A1 [95].

The goal of our research was to determine structural factors of POR protein-lipid interactions and dynamics on membrane. The work was done in collaboration with Dr. Jung-Ja Kim (Medical college of Wisconsin, Milwaukee, Wisconsin). In our research we utilized rat POR, a well-studied homolog of human POR. A BLAST [96] sequence alignment reveals 84% gene sequence identity between human and rat POR.

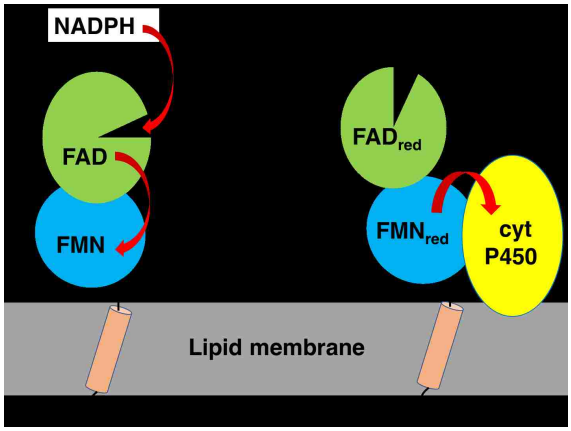

Figure 36. Schematic representation of conformational exchange experienced by POR during electron transfer cycle

To address those challenges, we utilized Methyl-TROSY technique in combination with extrinsic small-molecule-isotopic-labeling with S-methyl methanethiosulfonate (MMTS). Labels were attached to surface-exposed cysteines introduced by site-directed mutagenesis. Attachment of the label results in a methione-like side chain – methylthiocysteine (MTC). All native cysteines were first mutated to alanines and threonines (created by Dr. J Kim laboratory) to avoid non-specific labeling.

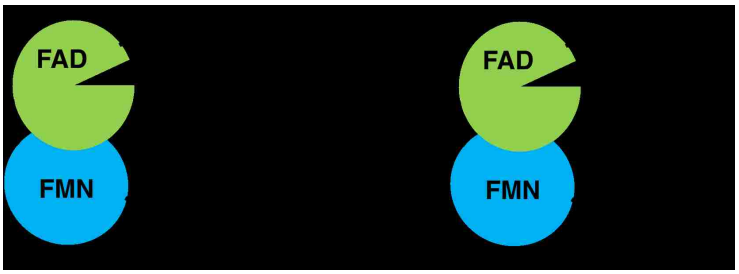

Figure 37. POR labeling scheme with MMTS

Mutation of the native cysteines does not alter the flavin content of the protein, as tested by a flavin content assay. This assay relies on the fact that fluorescence quantum yield of FAD is 9-times lower than that of FMN. FMN has low $K_D \sim 10^{-8}$M (unlike FAD with $K_D<10^{-9}$M) and it can be released from POR under high ionic strength condition. By comparing fluorescence before and after the addition of phosphodiesterase that converts FAD to FMN (Table 5), one can quantify flavin content.

Table 5. Flavin content of cys-less Δ56 POR, Δ56 POR carrying cysteines and labeled protein.

	Percentage cofactor content of a protein, %
Δ56 POR cysteine-less	95±3
Δ56 POR Q157C Q517C	96±4
Δ56 POR MTC-157,517	92±3

On the other hand, activity of the protein towards reduction of cytochrome c is impaired by mutation. Specifically, deletion of cysteine in the position 630 results in a ~50-fold decrease in activity compared to the wild type protein. However, introduction of additional cysteines (those investigated in our research) and their labeling with MMTS does not further affect protein activity.

Table 6. Activities of cys-less Δ56 POR, Δ56 POR carrying cysteines and labeled protein.

	Specific protein activity, mol cyt c reduced/ min×mol POR	Percentage of WT protein activity, %
Δ56 POR cysteine-less	78 ±2	2.65
Δ56 POR Q157C Q517C	75 ±4	2.50
Δ56 POR MTC-157,517	77 ±3	2.56

To test whether MTC labels will be sensitive to different redox states of the protein, we selected five strategically chosen locations on cytosolic portion of POR lacking transmembrane region (Δ56 POR). Figure 38 shows localization of the five mutations E127C, Q157C, N271C, S308C, and Q517C (after the labeling producing MTC-127, MTC-271, MTC-308, MTC-157 and MTC-517 respectively) introduced in cytosolic portion of POR based on what kind of redox/structural information they can probe in full-length protein attached to lipid bilayer. The MTC127 occurs at the membrane-facing region of the FMN domain and is relatively distant from the FMN cofactor, while MTC-157 is farther from the membrane and closer to the FMN, therefore sensitive to the redox state. The MTC-517 will be sensitive to the redox state of both flavins as well as the domain closing. It is also located near a putative interface of the POR-P450 complex. The MTC-308 and MTC-271 are localized far from the cofactors and are unlikely to be significantly affected by the enzyme redox status, open/closing transition or binding of the P450. In the full-length protein, however, the MTC-308 and MTC-271 may experience a dramatic change in the distance to the membrane upon closing transition, thus becoming possible reporters of the conformational changes in POR, providing two probes 2 Å away from each other. The membrane distance for MTC-127 is expected to be relatively invariable in the open and closed POR conformations because of its location on FMN domain that is interacting with cytochromes P450.

Protein redox state can be monitored by the changes in absorbance spectra. Figure 39 demonstrates absorbance spectra recorded immediately after NMR spectra acquisition. Oxidized POR flavins (red trace) are characterized by absorption bands at 380 and 450 nm while protein reduction with NADPH leads to a decrease in absorbance at those wavelengths and gives rise to a new broad absorption band at 550-650nm (blue trace). Comparison of our absorbance spectra from NADPH-reduced samples with the one in the work of Rwere et al [97] here they report on dithionite-reduced POR (infeasible in our research due to the nature of the labeling process) suggests that both FAD and FMN are in the semiquinone state. This di-semiquinone state was stably maintained in our samples for, at least, 4 h needed for a typical NMR experiment. The UV–Visible absorption spectra were recorded after every NMR measurement to verify the sample redox state.

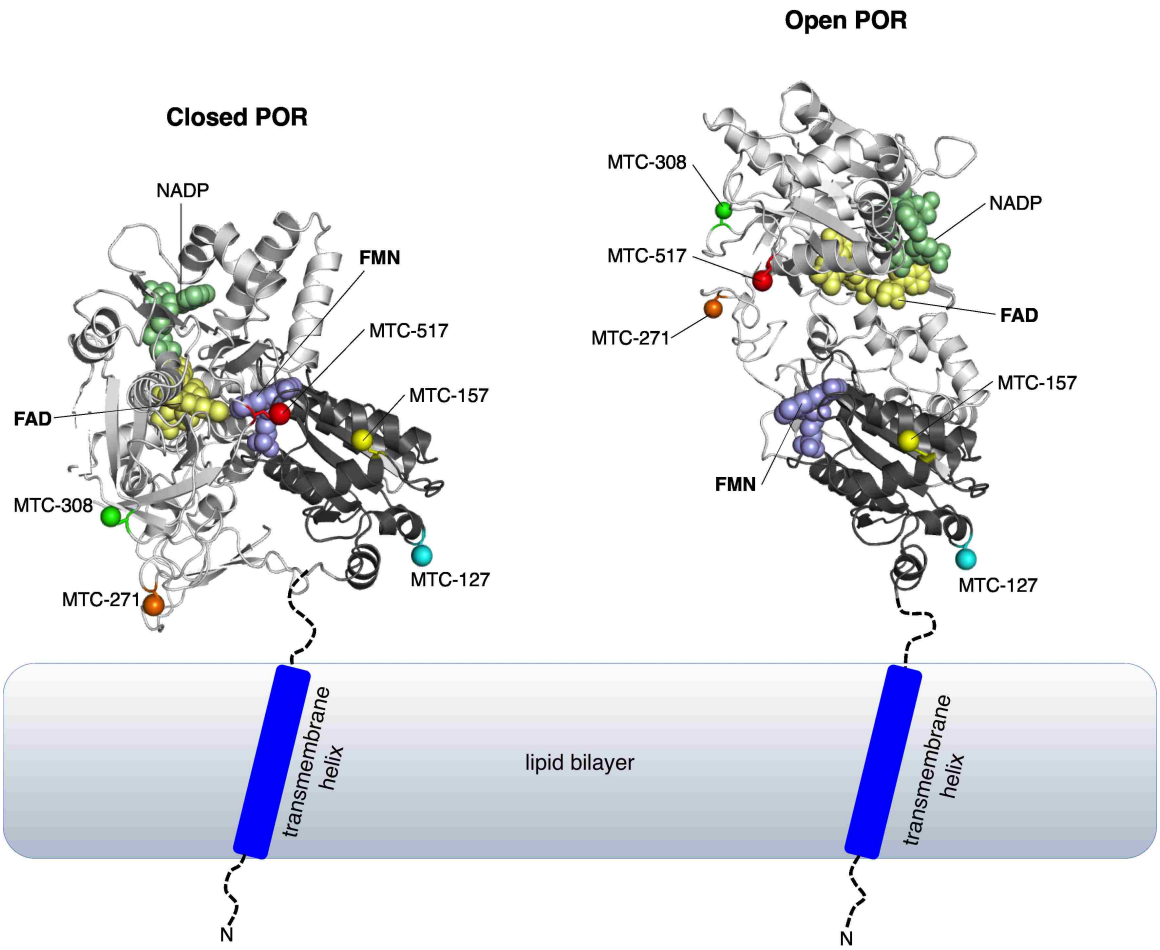

Figure 38. Localization of the methyl probes shown on a model of the membrane-bound open (left) and closed (right) conformations of POR (based on Δ56 POR crystal structures 3SE9 and 1AMO). Cartoon model of FAD-binding domain is colored light grey; FMN-binding domain—black; FAD, FMN, and NADP are shown as spheres in wheat, pale violet, and pale green, respectively. The lipid bilayer is schematically shown as a gray rectangle. The cytosolic unstructured portions of the N-terminal peptide (residues 1–56 absent from the crystal structures) are depicted as a dotted line. A purple rectangle stands for a transmembrane region of the N-terminal peptide containing a tilted helix [based on the solid-state NMR data. The γ-atoms of residues 127, 157, 271, 308, and 517 are shown as colored spheres. The particular orientations of the cytosolic portion of POR relative to the membrane surface was never structurally resolved, and only chosen in this model to emphasize differential membrane proximity of the labeled sites.

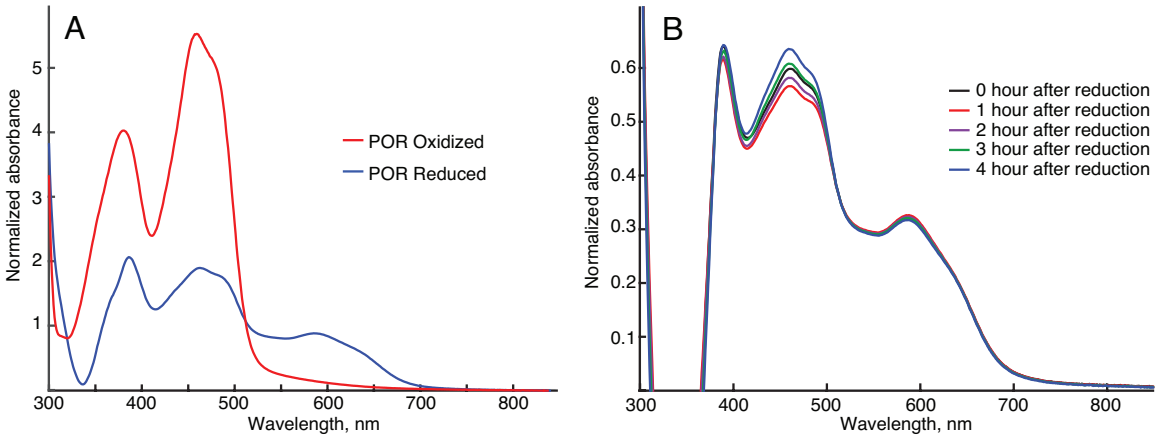

Figure 39. UV–Visible absorbance spectra of the POR flavins. A. Representative spectra of Q157C/Q517C Δ56 POR labeled with ^{13}C-MMTS oxidized with ferricyanide, red trace, and reduced with excess NADPH, blue-trace. Reduced trace (blue) is distorted in the wavelength range shorter than 400 nm due to incomplete compensation of the NADPH absorbance in the reduced sample by a reference NADPH solution. B. The time evolution of absorbance in a typical NMR sample reduced with NADPH. The sample was prepared the same way as if making a POR sample for NMR, but it was sealed in the optical cell instead of a Shigemi tube to allow for the repeated absorbance measurements.

Protein expression, purification and characterization results

Expression and purification of the cytosolic portion of POR (Δ56 POR) were set up in our lab. To obtain purified protein, cell lysate centrifuged and its supernatant was passed through Ni-affinity column followed by 2',5'-ADP Sepharose column. Purified protein yield was ~50mg from 1L of expression culture which is sufficient for 3 NMR samples with 300μM concentration of each.

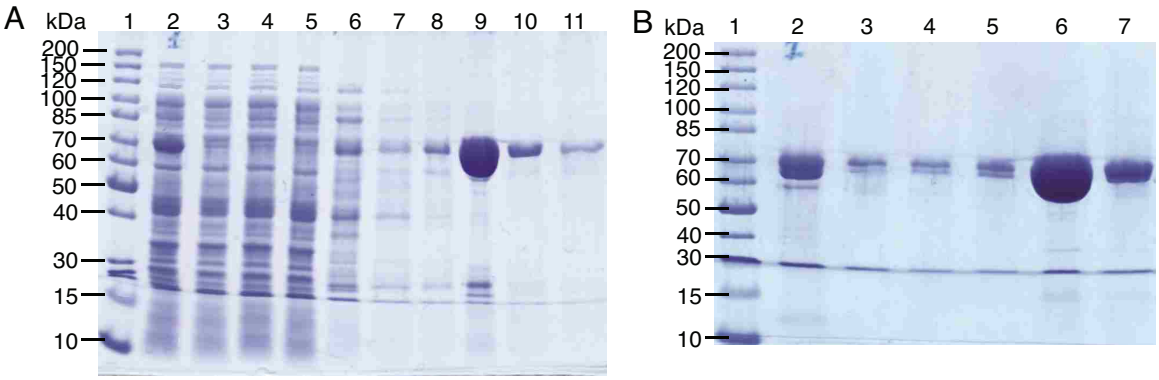

Figure 40 Analysis of Δ56 POR expression level and its purification quality by SDS-PAGE. A**.** PageRuler™ Unstained Protein Ladder (ThermoFisher, 26614) (lane 1). Cell lysate of induced (lane 2) and non-induced (lane 3) expression culture; lysate SN after ultracentrifugation of induced (lane 4) and non-induced (lane 5) expression culture. His60 NiSuperflow column flow-through (lanes 6,7), wash (8) and elution from the column (lanes 9-11). B. PageRuler™ Unstained Protein Ladder (ThermoFisher, 26614) (lane 1). 2',5'-ADP Sepharose 4B column injection (lane 2); flow-through (lanes 3-5) and elution from the column (lanes 6,7).

Protein concentration was determined using specific absorption at 450nm due to the presence of flavin cofactors as well as Bradford assay based on protein staining by Coomassie reagent. As it was mentioned before, activity assay and flavin content assay was performed for each sample. Protein molecular weight can only be estimated on the base of the SDS-PAGE. To confirm the integrity of the protein and its molecular weight, we additionally utilized MALDI-TOF mass spectrometry targeting proteins with molecular weight greater than 30kDa which was set up in our lab. Figure 41 demonstrates greater sensitivity of the technique utilizing complex α-CHCA/DHB matrix compared to standard sinapinic acid for 72kDa Δ56 POR which allowed us to confirm that purified protein has expected molecular weight.

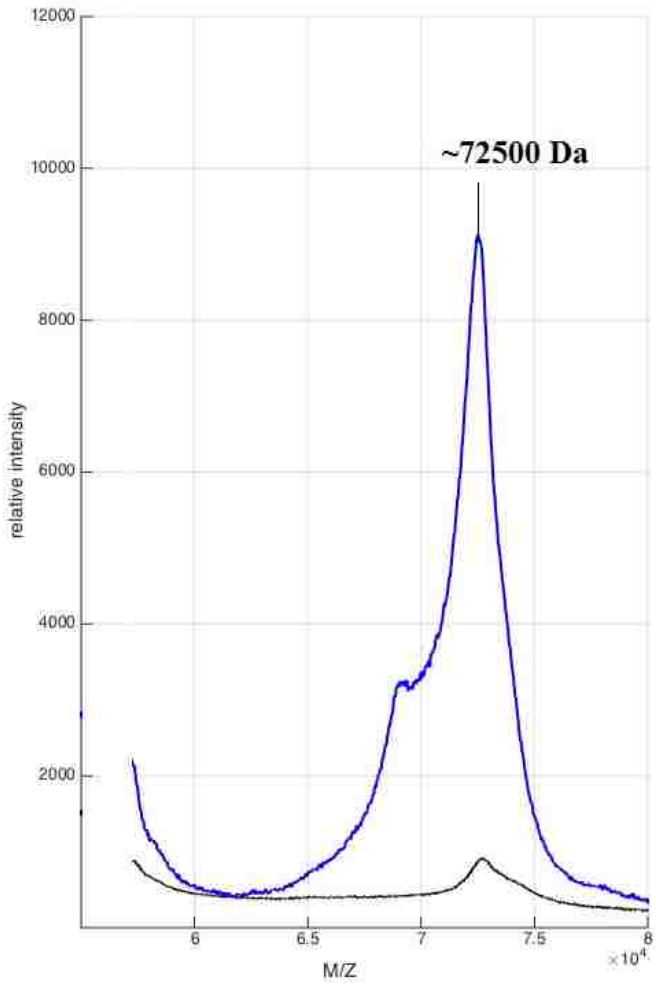

Figure 41. Comparison of MADI-TOF mass-spectra POR Δ56 Q157C Q517C obtained using SA and α-CHCA/DHB matrices. Black trace corresponds to the data obtained using SA matrix; blue – data from application α-CHCA/DHB matrix.

Differential redox sensitivity of MTC-labels

Purified Δ56 POR mutants had their thiols modified with ^{13}C-MMTS and acquired ^{1}H-^{13}C HMQC spectra. Single cysteines mutants in case of E127C, Q157C, S308C, Q517C and double-mutant for Q157C/N271C were used to do resonance assignment. Figure 42 shows that these sites are spectrally resolved and their surface localization attenuated paramagnetic relaxation—MTC signals are detected even in the reduced POR. Each mutant spectrum contained two peaks: the specific resonance (labeled in

the figure) and the broad peak seen in the center of the spectral region (later in the text referred to as middle peak).

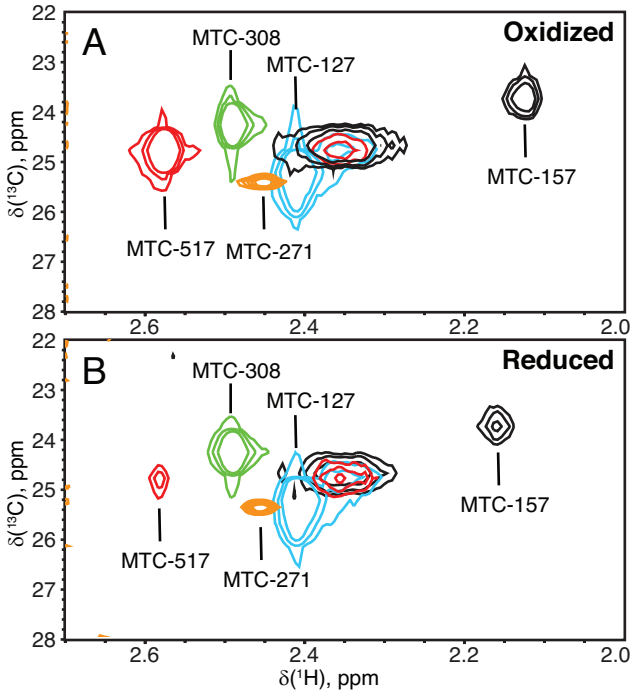

Figure 42. Overlay of ^{1}H-^{13}C HMQC spectra of the five single-cysteine mutants of Δ56 POR in the oxidized (A) and reduced (B) states. Contour levels were adjusted to account for the differences in NMR sample concentration.

Despite the presence of the middle peak, the specific resonance assignments are unambiguous, and the signals are well resolved to allow the use of multiple-cysteine mutants to significantly cut costs and experimental time. Differential sensitivity of resonances was in agreement with the experimental design. Probes positioned at residues 127, 271 and 308 are too far from the redox centers (flavin cofactors) neither they are located at conformational hotspots showing no sensitivity towards protein reduction. Specific signals from MTC-157 and MTC-517 (presented separately on Figure 44) demonstrate sensitivity towards protein reduction, specifically MTC-517 that resides in the cleft between POR domains (with 20Å to cofactors) is significantly

affected by this process, resulting in strong paramagnetic line broadening (decrease of peak intensity). Both MTC-157 and MTC-517 experience chemical shift perturbation which may either be the result of a change in the chemical environment suggesting conformational changes or may be due to paramagnetic pseudocontact shift effect from semiquinone flavin cofactors due to anisotropy of semiquinone magnetic susceptibility tensors. Since MTC-157 is positioned on the surface of FMN domain and far away from interaction interface with FAD domain, therefore it is not expected to undergo any conformational changes, the effect must originate purely from a pseudocontact shift. MTC-517 on the other hand is harder to interpret since it is positioned between FAD and FMN domains hence will be affected by opening and closing of POR. But since magnetic susceptibility tensors of FAD and FMN in a context of POR are yet to be known, it is impossible to make a clear explanation of the phenomenon observed.

It is hypothesized in the literature [98] that indole ring of Trp677 located between flavin moiety of FAD and nicotinamide moiety of NADPH acts as a lid controlling hydride transfer. In the existing structures obtained by X-ray crystallography, nicotinamide ring of NADP is located outside binding pocket and requires displacement of Trp677 indole ring that may trigger allosteric process within POR. Therefore $NADP^+$ titration was performed on a sample with the probes in the position 157 and 517 demonstrated to be sensitive towards protein reduction and possibly conformational changes without a change of redox state. Unfortunately, Figure 43 demonstrated lack of any effect on the two labels towards $NADP^+$ addition. It should be noted though, that one of the reasons might be that labels are located on the surface are insensitive to conformational changes within the protein.

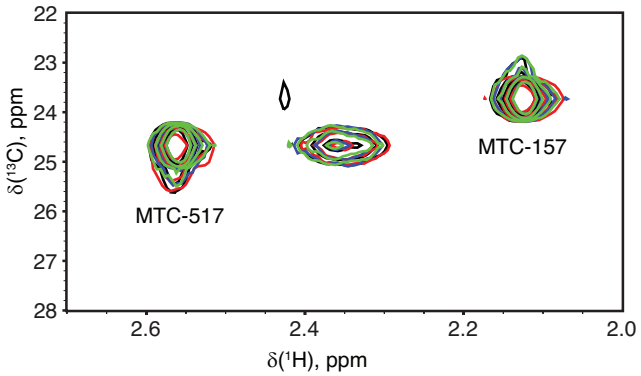

Figure 43. ^{1}H-^{13}C HMQC spectra from Δ56 POR MTC-157,517 incubated with 1.5- (red), 3- (blue), and 5-fold (green) excess of $NADP^{+}$.

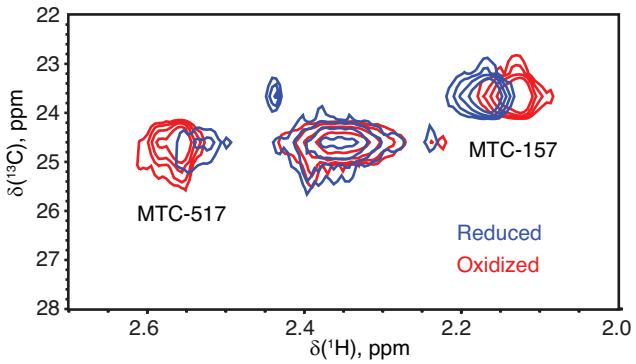

Figure 44. Effect of protein reduction. ^{1}H-^{13}C HMQC spectra at 600 MHz of the Q157C/Q517C Δ56 POR in the oxidized (red) and reduced (blue) forms.

Differential conformational constraint sensitivity.

To gain an additional insight into the opening-closing transition in POR, we employed a conformationally restrained Δ56 POR construct where the loop connecting FAD- and FMN-binding domains was shortened by removal of the four-residue sequence TGEE at the positions 236–239. In our research, we referred to the construct as "ΔTGEE" in contrast to "full loop" mutant which maintained all amino acids of POR cytosolic portion. This modification made cytosolic portion of POR to adopt an "open" conformation observed in a structure derived by X-ray crystallography (Figure 12.B). It has been hypothesized in the original work that this structure corresponds to

POR conformation when it interacts with cytochrome P450 to perform electron transfer. Despite the fact the structure obtained by X-ray crystallography does not allow inter-flavin electron transfer, this construct is susceptible to reduction, moreover as it can be seen from the absorbance spectra obtain from the samples subjected to the same reduction protocol as a "full loop" constructs, both flavins adopt semiquinone state similar to the full loop counterpart (Figure 45 C and D). Small differences in the reduced spectrum are due to incomplete consideration of NADPH presence in the background (λ_{abs}=340nm).

Figure 45 demonstrates the effect of loop deletion on the chemical shifts of the two most sensitive residues, MTC157 and MTC517, in the oxidized Δ56 POR. Position of the MTC-157 is far away from conformational center and it overlays perfectly with the resonance from "full loop" construct unlike the resonance of MTC-517. Since the distance from MTC517 to the loop deletion site is around 45Å, perturbation of MTC-517 can only occur due to a transition between "open" and "closed" states. Since, it is not straightforward to convert the chemical shift change into the amplitude of a structural rearrangement, we will restrict ourselves to a statement that the oxidized ΔTGEE Δ56 POR conformation in solution is distinct from the conformation of oxidized full-loop Δ56 POR.

POR reduction produces an interesting effect on signals from the probes MTC-157 and MTC-517 in case of ΔTGEE construct demonstrating an emergence of signal splitting for both probes which is in case of MTC-517 is unresolved. In both cases one resonance remains close to the original position of oxidized ΔTGEE Δ56 POR while a new resonance rises at the position near the one from the reduced full loop Δ56 POR. Since presence of two signals from each label cannot be resulted by difference in the level of reduction (reduction level is the same according to absorbance spectra), this

phenomenon must arise from slow exchange conformational equilibrium between two distinct magnetically and chemically non-equivalent open and closed states.

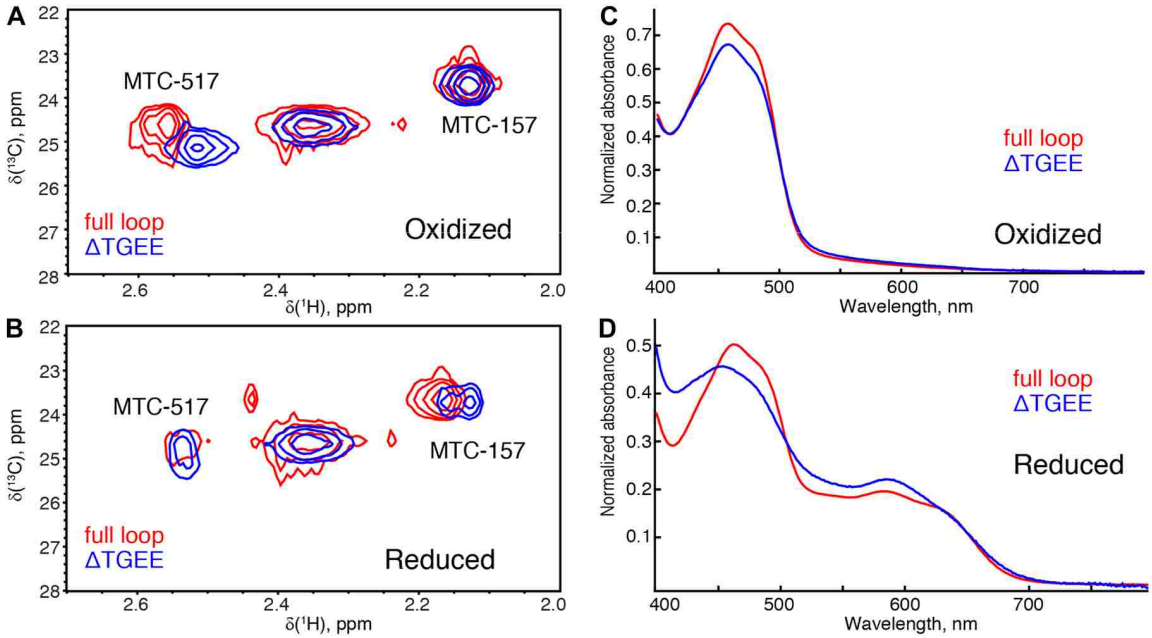

Figure 45. Effect of the loop deletion (^{236}TGEE^{239}) on chemical shifts of Q157C/Q517C Δ56 POR in the oxidized (A) and reduced (B) states. Absorbance spectra of the oxidized (C) and reduced (D) NMR samples (recorded immediately after acquisition).

The four amino acids deletion in the hinge region is expected to destabilize the inter-domain motion since ΔTGEE construct adopts open conformation in a crystal structure while being capable to FMN reduction. This results a slow frequency conformational fluctuation motion between open and closed states of ΔTGEE construct. The peak separation of MTC517 signals is approximately 0.4 ppm in ^{13}C dimension (corresponding to $\Delta\omega = 377\ s^{-1}$), and for MTC157 — 0.025 ppm in ^{1}H dimension ($\Delta\omega = 94\ s^{-1}$). To observe the two conformer signals with this separation requires the exchange rate constant, k_{ex}, to be much smaller than 100 s^{-1} ($k_{ex} << \Delta\omega$). It is remarkable that the new resonances of the ΔTGEE POR in the reduced state have chemical shifts similar to the ones of the reduced full-loop POR. This implies that

both proteins adopt similar conformations in the NADPH-saturated reduced state, despite they were in distinct oxidized conformations. Moreover, the fact that full-loop POR demonstrates only single resonance while ΔTGEE POR two resonance under reduced conditions suggests that loop deletion is affecting the structure of the protein in reduced state. If protein reduction resulted in a conformational change to an open state for full-loop construct, we would have observed only single resonance for ΔTGEE version of the protein, since loop deletion makes open conformation a more favorable one. Hence, the loop deletion leads to a slower exchange between reduced conformational state compared to the closed full-loop POR, suggesting that protein assumes closed conformation in the reduced state. Though it still might be different than that of the oxidized Δ56 POR crystal structure, due changes that might occur in the domain interaction interface.

Nevertheless, we cannot state that chemical shift perturbation of the signals observed has only paramagnetic nature since redox status of the flavins can affect structure of the protein without assuming an open conformation.

Non-specific resonance from MMTS-labeling

As our next goal, we decided to perform detailed investigation of the non-specific resonance observed in our sample. It should be note that the peak has complex structure and represents a cluster of a smaller peaks with similar chemical shifts.

We also observed that the proportion of spectral intensity observed as the middle peak widely varies among different mutants and different preparations of the same mutant (see Table 7).

Table 7. Evaluation of intensity of the middle peak in different Δ56 POR preparations. Ratio of intensities of specific signals and the middle peak in ^{1}H -^{13}C HMQC was measured and a magnitude of the middle peak was expressed a as a percentage of the specific peak intensity.

Labeling Site	Redox State	Specific signal, S/N	Middle peak, S/N	Middle/Specific, %
MTC-127	Oxidized	409	24	6%
	Air*	219	17	8%
	Reduced	356	30	8%
MTC-157	Oxidized	120	60	50%
	Air*	243	44	18%
	Air**	43	8	19%
	Reduced	98	40	41%
MTC-308	Oxidized	406	10	2%
	Air*	508	15	3%
	Reduced	263	9	3%
MTC-517	Oxidized	102	60	59%
	Air*	330	44	13%
	Air**	51	8	16%
	Reduced	13	40	308%

The original proposal for the source of the non-specific resonance peak was non-specific labeling with MMTS. To test this hypothesis, we expressed and purified cysteine-less Δ56 POR construct and subjected to the same labeling protocol as we did for the other samples. Figure 46 demonstrates absence of any signals in the region interest confirming that MMTS labeling is highly specific for cysteines and the label is not retained non-specifically by the protein or flavins. Therefore, we conclude that the "middle peak" must originate from a reaction with the same cysteine that gives rise to the specific resonance.

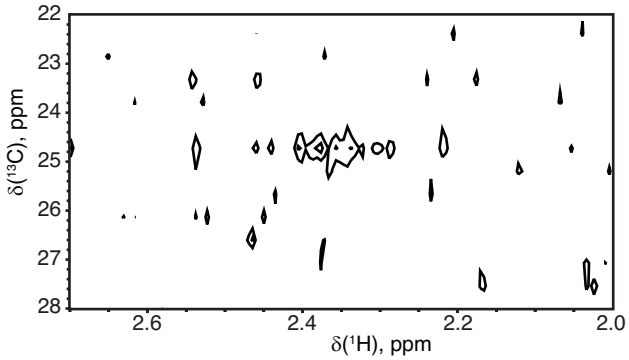

Figure 46. ^{1}H-^{13}C HMQC spectra from Δ56 POR cysteine-less construct incubated with ^{13}C-MMTS. Contour level was lowered to the noise floor to demonstrate the absence of signals.

Similarity of the chemical shifts of the middle peaks in case of all mutants that are located in the different positions across the protein suggested similarity in the structural environment. One explanation for this fact would be hydrolytic degradation or unfolding followed by non-specific aggregation of POR. To test this hypothesis, we performed size-exclusion chromatography (SEC) on Superose6 Increase 10/300 GL (GE Healthcare) of the NMR sample to separate Δ56 POR MTC-157,517 sample from possible degradation products or large unfolded aggregates. Elution peak maxima was taken and sample ^{1}H-^{13}C HMQC spectra was recorded immediately after the SEC without additional concentration step to exclude concentration effect on protein degradation. Lower counter level of the sample after SEC is explained by dilution effect of the column. Results obtained revealed no significant change in relative intensities of all three peaks (Figure 47).

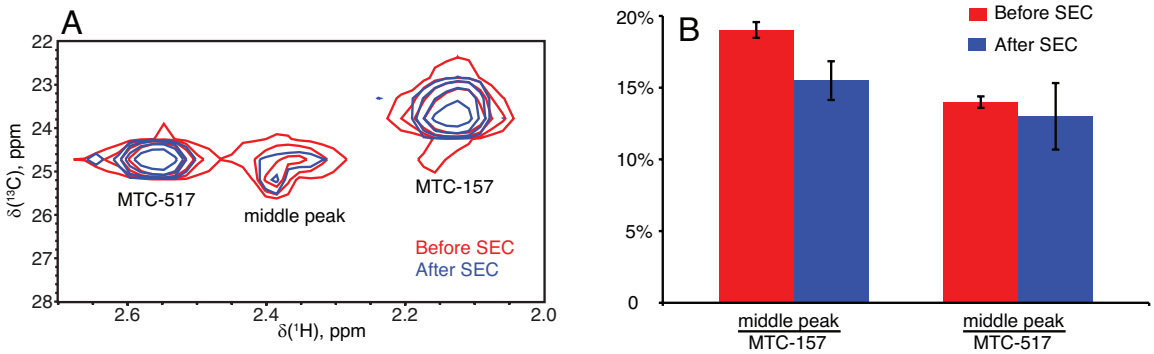

Figure 47. "Middle peak" species are not removed by SEC. **A** ^{1}H-^{13}C HMQC spectra obtained from Δ56 POR MTC-157,517 before (red) and after (blue) SEC. **B** Relative intensity of the middle peak as a percentage of MTC-517 and MTC-157 intensities before (red) and after (blue) the size-exclusion chromatography.

This result indicates that non-specific resonance signal originates from a monomeric fully folded Δ56 POR molecule where all MTC labels experience similar magnetic environment. One of such cases will be when MTC side chain adopts conformation where it is extended into a solvent, while the specific peaks correspond to side chains

interacting with the protein surface. On the other hand, magnetic environment of such conformation should be similar to the methylthiocysteine (MTC) in a solution. Cysteine was dissolved in water and labeled with MMTS followed by ^{1}H-^{13}C HMQC NMR experiment. Since sample dialysis was impossible, byproducts of cysteine labeling were observed on the spectra. However, results obtained from the 2mM MTC in solution demonstrated that chemical shift of the MTC signal (MTC – 2.24ppm 22.44ppm) is different from that of the middle peak thus providing evidence against our hypothesis.

Our original assumption was based on the fact that the middle peak is neither product of non-specific labeling nor signal originating from degraded/aggregated protein. We observe both specific resonance and middle peak while signal separation for MTC-157 and non-specific resonance is approximately 0.25 ppm in ^{1}H dimension (corresponding to $\Delta\omega = 942\ s^{-1}$) which signifies that interconversion, if it exists, has to be in slow exchange kinetic regime. To determine whether specific resonance and middle peak come from the same species we decided to carry out ZZ-exchange experiment, also known as exchange spectroscopy (EXSY). The main idea of this experiment is to allow sample to undergo conformational exchange while carrying magnetization. At the start of experiment magnetization is being transferred on separate conformation S and P but instead of recording spectra right away, long evolution time is applied to allow some of the conformation S to turn into P and vice versa and only then FID acquisition occurs. This process creates cross-peaks on the spectra between two resonances in a slow exchange regime (Figure 48 A).

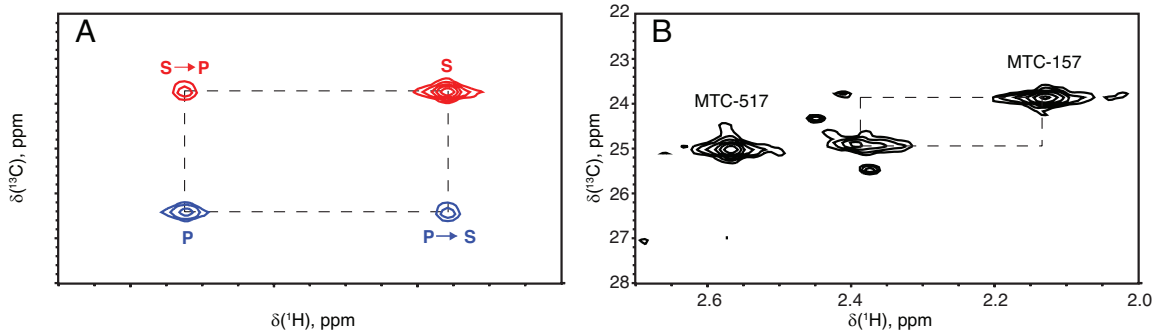

Figure 48. A. Expected cross-peaks in a ZZ-exchange experiment for two conformations S and P that are in a slow exchange regime. B. Exchange spectroscopy to ZZ-exchange NMR experiment demonstrates absence of cross-peaks for specific resonance of MTC-157 and "middle peak". Dashed line intersections specify positions of the expected cross-peaks.

Figure 48.B clearly demonstrates the absence of cross-peaks between non-specific resonance and MTC-157 indicating no conformational exchange between the source of those two signals. Thus, results of the ZZ-exchange experiment suggest sample heterogeneity which cannot be removed with size-exclusion chromatography.

Thus, to sum up our observations, presence of the middle peak in different mutants suggests similar magnetic and hence chemical environment for the labeled cysteines. Moreover, non-specific resonance was insensitive towards protein reduction and conformation constraints suggesting that origin of those species is a misfolded, inactive, monomeric Δ56 POR molecule.

Since misfolded protein cannot be removed by SEC and cannot be detected by SDS-PAGE gel, MALDI-TOF spectrometry, absorbance spectroscopy, we concentrated our efforts on modification of protein purification protocol to provide homogenous and active Δ56 POR. Figure 49 shows the result of modified protein purification protocol that relies on higher hydrophobicity of the misfolded protein providing homogenous NMR samples.

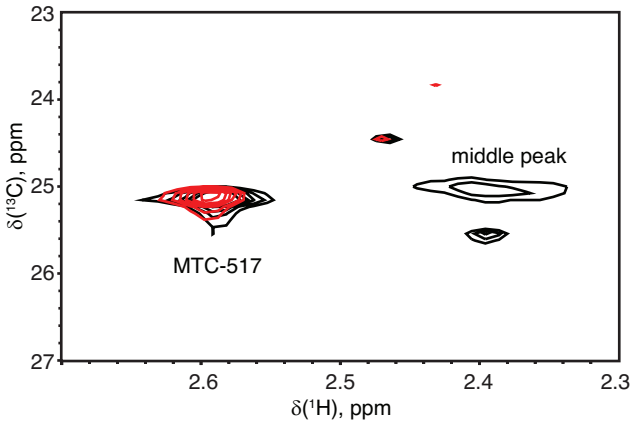

Figure 49. Removal of the middle peak species from the sample Δ56 POR. Overlay of ^{1}H-^{13}C HMQC spectra of the Δ56 POR MTC-517 in the oxidized states purified using standard (black) and modified (red) protocol.

After visually comparing homogeneous Δ56 POR NMR samples with heterogeneous one, we observed lower stability of the heterogeneous sample (sample was prone aggregation after 3 hours within the NMR tube), due to this fact we weren't able to isolate misfolded species. Another interesting observation was that heterogeneous sample is prone to auto-reduction within 2 days in the absence of oxidizing agents.

It has to be noted that flavin content assay demonstrated complete cofactor loading for the samples where total protein concentration was controlled by Bradford assay. So, we can hypothesize that presence of cofactors serves as a stabilizing core for misfolded Δ56 POR molecule preventing it from aggregation.

Table 8. Activities of Δ56 POR with and without misfolded species

	Specific protein activity, mol cyt c reduced/ min×mol POR	Percentage of WT protein activity, %
Δ56 POR MTC-157,517	78 ±2	2.65
Δ56 POR MTC-157,517 with 46% of misfolded species present	45 ±3	1.50

Results of the cytochrome c activity assay demonstrated that misfolded protein is indeed inactive as it was suspected. Percentage of misfolded species was calculated from the volume of the middle peak relative to the sum of peak volume of middle peak and specific resonance. But since in our approach we utilized modified protein, loss in activity was associated with modification introduced in the protein complicating the problem detection. However, NMR techniques are capable to investigate those species separately since they provide their own signals; on the other hand, misfolded protein cannot be detected by any other analytical techniques such as small-angle X-ray scattering, DEER spectroscopy or fluorescence and as a result providing data that can be easily misinterpreted.

However, we shouldn't disregard the data obtained in our experiment from misfolded species as an error in sample preparation. Despite the fact the protein in our experiment was overexpressed and then purified from *E. coli*, presence of the misfolded POR stabilized by flavin cofactors in our experiments may have physiological importance not only for POR but other cofactor-containing proteins in vivo. One of such examples would be amyloidosis where amyloid fibrils are building up in the tissues due to protein misfolding. Several studies have shown that soluble misfolded oligomers are more toxic than final fiber aggregation [99]. And presence of the some of small molecules in a cytosol (non-native cofactors) can serve as stabilizing cores for such species.

Matrix Scaffold Protein expression and purification

It has been successfully demonstrated that MMTS-labeling coupled with Methyl-TROSY technique can be utilized to probe reduction of Δ56 POR and effect of introduction of conformational restraints. To extend this approach onto full-length

protein we first need to consider the lipid membrane mimic that was utilized in our study. A number of existing lipid mimetic systems were introduced in Chapter 2 and the one which provides a lipid bilayer surface without introduction of detergents and allows application of NMR technique to study lipid-protein dynamics is a lipid nanodisc. Nanodiscs are soluble discoidal structures mimicking the flat surface of the cellular membranes where the area of the lipid bilayer is surrounded by a matrix scaffold protein. The size of a lipid nanodiscs can vary, depending on MSP protein construct selected. For our preliminary research, we selected MSP1D1 protein which, upon assembly, provides nanodisc with 10nm disc diameter and 8nm diameter of a lipid bilayer surface. This area is sufficient to incorporate a full-length POR molecule. Nanodisc application provides an additional control to reproduce a system where one POR molecule is attached to one nanodisc, defining solution composition and preventing generation of one nanodisc with multiple POR molecules which may affect protein-interaction.

Expression and purification of His-tagged MSP1D1 was performed in our lab with protein yield of ~30mg from 1L of expression culture which is sufficient for 6 NMR samples with 300μM concentration of empty nanodiscs. After purification, the protein sample was characterized by absorbance spectroscopy, SDS-PAGE, Bradford assay and MALDI-TOF spectrometry.

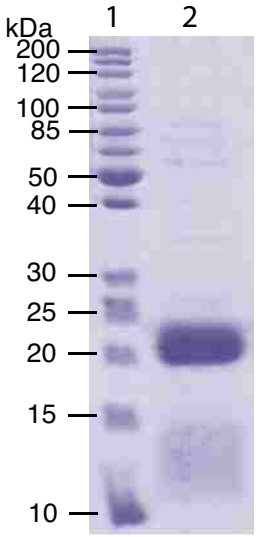

Figure 50. SDS-PAGE gel demonstrating molecular weight and purity (>95%) of the purified MSP1D1 protein sample (lane 2) after all purification steps and His-tag cleavage against PageRuler^{TM} Unstained Protein Ladder (ThermoFisher, 26614)(lane 1).

Empty DOPC/DOPG lipid nanodisc

Empty nanodisc assembly was carried out as described in Chapter 4. It has been reported that lipid composition can affect reduction potential of the protein. It was reported earlier that the redox potential of POR is modulated by a lipid composition of the bilayer [44, 100].

Lipid composition was selected to be 15% DOPG and 85% DOPC which mimics the surface charge of the endoplasmic reticulum in rat liver [101] (15% - negatively charged lipids, 73% - uncharged lipids). After nanodisc assembly, sample was injected into gel-filtration column Superose 6 Increase to provide homogenous mixture of 10-nm nanodiscs. This step also served to provide a gel-filtration profile of a nanodisc system and ensure that its elution volume corresponds to hydrodynamic volume of the species (~160 kDa). To demonstrate that nanodiscs are not nonspecifically labeled by MMTS, we subjected empty nanodisc sample to the same

labeling protocol as for Δ56 POR. Figure 51 proves specificity of MMTS label; major peaks on the full spectra are originating from lipids within nanodisc.

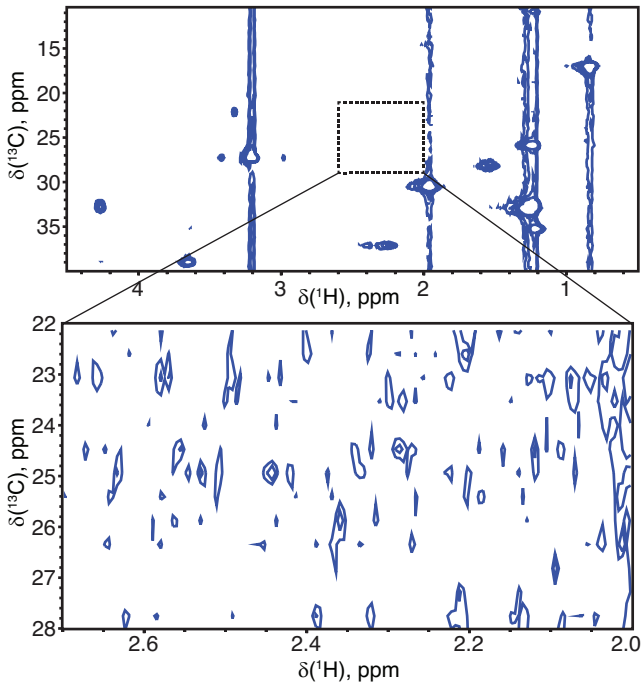

Figure 51. 13C-MMTS does not bind to nanodiscs. ^{1}H - ^{13}C HMQC spectra obtained from a nanodisc sample incubated with MMTS in the absence of POR. (Top) Full spectral range showing signals of the nanodisc lipids and the matrix scaffold protein. (Bottom) Enlarged spectral region where MTC signals are typically observed. Contour level was lowered to the noise floor.

Another advantage of the application of lipid nanodiscs is ability to utilize it in MALDI-TOF mass spectrometry. MALDI-TOF is very demanding to a sample preparation and does not tolerate the presence of detergents. Detergents are required to be present during full-length membrane protein purification to solubilize membrane-binding portion of membrane proteins. By assembling sample onto a lipid nanodisc and subjecting it to MALDI-TOF spectrometery allows us to determine protein molecular weight even for a membrane proteins.

Full-length NADPH-cytochrome P450 oxidoreductase

The expression and purification of the His-tagged full-length POR mutants which was more complex and demanding than that of a cytosolic POR was set up in our lab. His-tag was engineered to be non-cleavable to be later utilized during protein-nanodisc complex purification. Cleavage of the His-tag will require absence of protease inhibitors in the solution which makes a sample venerable towards cleavage if cytosolic portion of the protein from the nanodisc complex. Protein expression levels are high but amount of the extractable protein is smaller compared to the cytosolic portion. In addition, purification scheme is more complex and time-consuming since it requires significant dilution during purification to solubilize full-length POR. Moreover, protein is unstable, requires presence of detergent and extremely susceptible to proteolysis. Purified protein yield was ~5mg from 1L of expression culture, 2 L of expression culture are sufficient for 1 NMR samples with 100μM concentration of each (protein alone without considering losses during nanodisc complex assemble).

It should be noted that due to a nature of purification from misfolded protein, which relies on its hydrophobicity, it cannot be applied for a full-length protein because of the presence of hydrophobic membrane-binding domain of the protein that requires presence of detergents rendering established purification protocol incapable of getting rid of misfolded protein.

Purified protein was subjected to the same characterization techniques which were applied to cytosolic POR. Similar results were observed for full-length protein: complete flavin loading, reduction activity by NADPH, recording of the absorbance spectra and cytochrome c activity assay (results obtained for FL POR Q157C Q517C were 65±3 mol cyt c reduced/ min×mol POR).

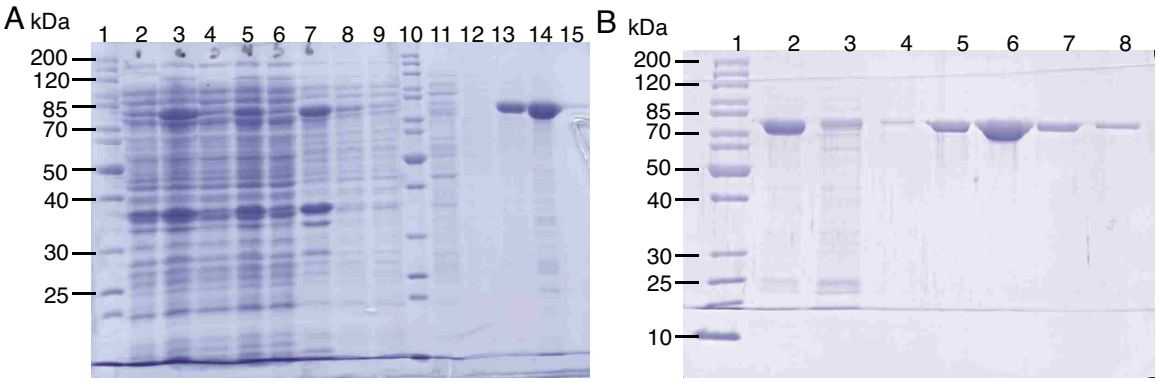

Figure 52. Analysis of full-length POR expression level and its purification by SDS-PAGE. A PageRuler^{TM} Unstained Protein Ladder (ThermoFisher, 26614) (lane 1,10). Cell lysate of non-induced (lane 2) and induced (lane 3) expression culture; lysate SN after first centrifugation of non-induced (lane 4) and induced (lane 5) expression culture. After first centrifugation induced lysate SN was subjected to ultracentrifugation resulting SN (lane 6) and pellet (lane 7). Pellet was solubilized, incubated with detergent and ultracentrifuged again providing SN (lane 8) loaded into the His60 NiSuperflow column. His60 NiSuperflow column flow-through (lanes 9); wash (11,12) and elution from the column (lanes 13-15). B PageRuler^{TM} Unstained Protein Ladder (ThermoFisher, 26614) (lane 1). 2',5'-ADP Sepharose 4B column injection (lane 2); flow-through (lanes 3,4) and elution from the column (lanes 5-8).

Nanodisc assembly

NMR studies of membrane proteins integrated in the lipid bilayers are very challenging due the presence of the lipid environment. Solution NMR studies of membrane proteins were made possible utilizing soluble lipid bilayer mimics such as bicelles and, in particular, lipid nanodiscs. But, the FL POR, due to its large molecular weight and more so paramagnetic nature of electron transfer process, remained recalcitrant to NMR analysis either in the solution and solid states.

We incorporated full-length POR Q157C Q517C into a 10-nm nanodisc following established protocol reported in Materials and Methods (Chapter 4). Dual mutant FL POR Q157C Q517C was selected as a primary sample due to those probes' sensitivity towards the protein reduction. FL POR labeling was performed after its insertion into nanodisc as it was done for soluble cytosolic POR.

Figure 53 shows ^{1}H-^{13}C HMQC spectra obtained from 0.1mM oxidized (A, red) and reduced (B,blue) full-length POR incorporated into a nanodisc acquired at 600MHz instrument under protonated conditions. Remarkably, chemical shift perturbation observed from MTC-157 and MTC-517 probes in case of the protein-nanodisc complex was similar to that of a soluble cytosolic domain of the protein alone. This observation is in agreement with distance of the labels location to a lipid bilayer surface and their position on potential cytochrome P450 interaction surface. Signal linewidth broadening effect is shown on Figure 54 correlates with the increase in rotational correlation time of the protein-nanodisc complex compared to the soluble cytosolic portion while considering the relative flexible nature of the anchoring of POR on a lipid bilayer.

A peak in the lower right corner is a product of the full-length POR degradation (as judged by increasing intensity with the age of this sample).

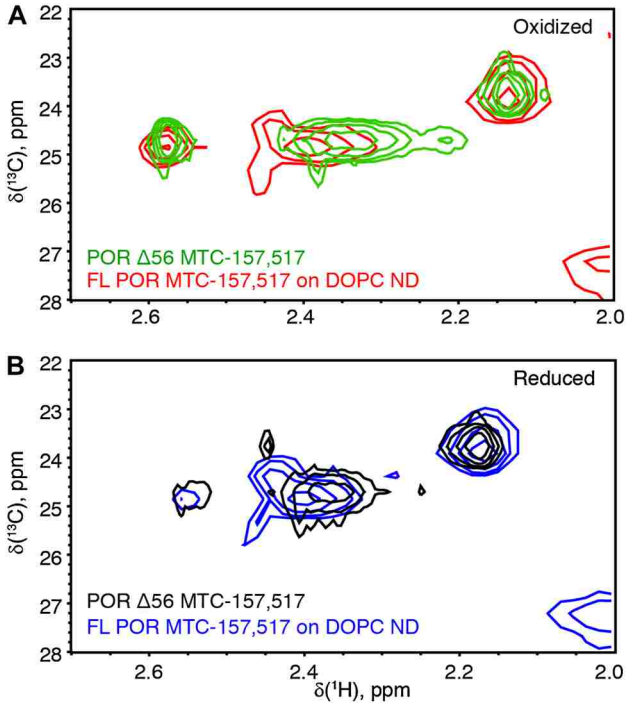

Figure 53. Protonated POR-nanodisc methyl-TROSY (^{1}H-^{13}C HMQC) spectra. A The air-oxidized full-length Q157C/Q517C POR in a lipid nanodisc (red) overlaid with

the Δ56 POR (green). B The same sam- ples reduced with the excess NADPH under anaerobic conditions: the full-length POR-nanodisc (blue); the Δ56 POR (black).

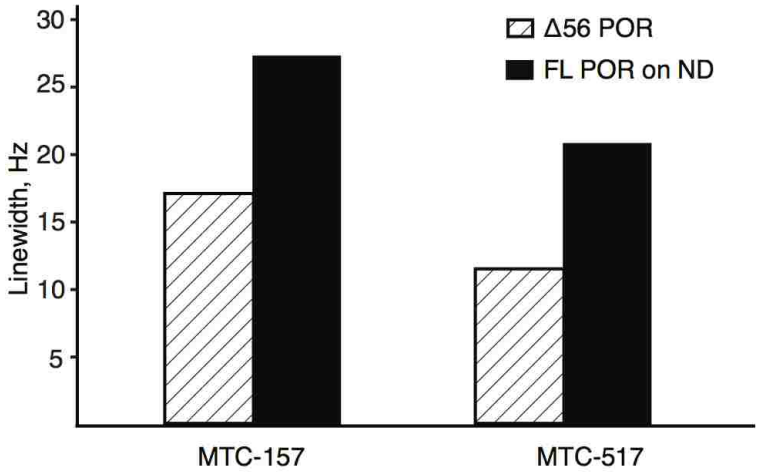

Figure 54. Effect of linewidth broadening of the MTC-labels due to increase of hydrodynamic volume of the complex.

Future research

In conclusion, we utilized 600 MHz instrument and obtained signals from extrinsically labeled 240 kDa lipid-protein complex in the presence of paramagnetic centers under protonated conditions. Signals demonstrated to be differentially sensitive to protein reduction and revealed behavior similar to cytosolic domain of POR. Application of Methyl-TROSY detection, one could monitor the redox reaction in POR and, possibly, even measure the redox potentials of individual flavins by following the MTC signals from FAD- and FMN-binding domains in a titration of POR with NADPH while varying lipid composition of the bilayer.

Another future prospect is to obtain distance restraints from the labels to a membrane surface is to apply PRE measurement by incorporating lipid carrying Gd^{3+} ion into bilayer of a nanodisc. Using this approach, one can investigate protein-lipid dynamics of POR attached to nanodisc as a function of lipid composition and redox state of the

protein cofactors. Moreover, utilizing the fact that lipids within nanodisc are dynamic equilibrium with each other [102]; we can titrate the sample with Gd^{3+} -labeled nanodisc achieving gradual increase in paramagnetic label concentration on the surface bilayer providing us with the set of distance restraints that will be used to calculate POR dynamics on the lipid bilayer surface depending on state of the protein, conformational restraints and lipid bilayer composition. And finally, one can introduce cytochrome P450 into the model and investigate protein structure and dynamics depending on the P450 isoform and parameters investigated previously for the POR alone. But it should be noted that the presence of native paramagnetic centers in both POR (semiquinone) and P450 (heme) cases might make data interpretation challenging.

IV. MATERIALS AND METHODS

DNA sequencing

To ensure that gene nucleotide sequence is correct, DNA sequencing was performed by Functional Biosciences Inc., Madison, WI.

H-RAS expression and purification

Ampicillin resistant pET43.1b plasmid containing H-Ras C118S 1-166 and H-Ras C118S 1-181 genes were transformed into E.coli BL21 (DE3) strains. H-Ras C118S 1-181 protein was expressed in a MJ minimal medium with uniform ^{15}N-labeling to enable both fluorescence and NMR measurements on the protein originating from the same preparation. At the same time H-Ras C118S 1-166 was expressed in Luria Broth media at 37°C for ~ 8hours at 0.1mg/ml Ampicillin concentration (same conditions for the minimal media). In both cases protein overexpression was induced by addition of isopropyl β-D-1-thiogalactopyranoside (IPTG) (OMEGA Biotek) to 1mM final concentration. Cells were allowed to grow for three hours, after that the cell culture was span at 500rpm for 15min to obtain cell pellet that was later resuspended in 20mM TRIS pH8.0 buffer for cell lysis. Resuspended cell mixture was subjected to lysis by sonication on Branson Sonifier 450. Pellet, obtained after cell lysate was centrifuged at 5000rpm for 15min, underwent solubilizations in 6M urea, 20mM TRISpH8.0, 10mM $MgCl_2$ solution for 3 hours, followed by protein refolding in the buffer containing 20mM TRIS pH8.0, 5mM $MgCl_2$, 0.3mM GDP, 1mM DTT. Solution containing refolded protein was centrifuged for 15min at 16,000rpm.

Supernatant obtained was dialyzed against 20x volume of 20mM TRIS pH8.0, 5mM $MgCl_2$, 50mM NaCl, 1.5mM NaN_3, 1mM DTT buffer and injected into XK16/40 ion-exchange column packed with Q HyperCel resin (Pall Life Sciences) preliminary equilibrated with the dialysis buffer. H-Ras protein was eluted at 290mM NaCl concentration.

Purified samples were concentrated with Amicon Ulra-15 centrifugal filter concentrator (Milipore) and were characterized with SDS-PAGE, Bradford assay, UV-vis spectroscopy and MALDI-TOF spectrometry.

Preparation of conjugated constructs

Purified ^{15}N-labeled H-Ras C118S 1-181 protein sample was incubated with 5mM dithiothreitol **(**DTT) (VWR Life Science AMRESCO) over-night. DTT was removed from the protein sample by passing through XK16/40 size-exclusion column packed with Ultrogel Aca54 (Sigma Aldrich) equilibrated with the 20mM HEPES pH 7.2, 1mM MgCl2, and 150mM NaCl buffer. H-Ras C118S 1-181 protein sample was eluted with the maxima at ~36 ml. Half of the elution peak maxima was used in the reaction with bismaleimido cross-linkers $BM(PEG)_2$/$BM(PEG)_{11}$ (Thermo Fisher Scientific/ Conju-Probe, respectively) in a 3:1 ratio (protein : $BM(PEG)_n$) to obtain Ras-11-Ras and Ras-2-Ras conjugates. Another half of the elution maximum was used as representative monomeric protein. Reaction was carried overnight at 4°C under nitrogen atmosphere and stopped by addition of 2mM DTT. To ensure stability of the potion of H-Ras C118S 1-181 that was not involved in cross-linking reaction, DTT was added to 1mM final concentration. After that samples were concentrated with Milipore

The conjugated constructs, Ras181-BM$(PEG)_2$-Ras181 ("Ras-2-Ras") and Ras181-BM$(PEG)_{11}$-Ras181 ("Ras-11-Ras"), were isolated from the reaction mixtures using the Ultrogel Aca54 size-exclusion column. Samples were characterized by MALDI-TOF mass-spectrometry to demonstrated that sample indeed corresponds to conjugated constructs: ^{15}N-labeled Ras-2-Ras conjugate had a mass of 41,700 ± 30 Da, which is consistent with the theoretical value of 41,668 Da; ^{15}N-labeled Ras-11-Ras conjugate exhibited molecular mass of 42,229 ± 40 Da with the theoretical value of 42,205 Da. Results of SDS-PAGE were in agreement with MALDI-TOF mass spectroscopy, taking into consideration an anomalous electrophoretic mobility of the Ras monomer due to its acidic pI of 5.0 . Unfortunately, the yield of Ras-11-Ras was significantly smaller compared to the final yield of 3 mg for the Ras-2-Ras conjugate. Protein concentrations were determined using Bradford assay.

MANT-GDP exchange

Protein samples were concentrated to ~10-30μM (Ras monomer units). GDP nucleotide associated with the protein was replaced by (2'-(or-3')-O-(N-methylanthraniloyl) guanosine 5'-diphosphate (Mant-GDP) (Life Technologies) using ethylenediaminetetraacetic acid (EDTA) to assist the nucleotide exchange. Nucleotide exchange was initiated by addition of EDTA to 6mM, Mant-GDP to 0.8mM and DTT to 10mM concentrations in the final reaction. Reaction mixtures were incubated for 30-60 minutes at room temperature and separated by Nap-5 Columns (Manufacturer: GE Healthcare Life Sciences) packed with G-25 size-exclusion resin. Bradford assay was used to determine final protein concentration to be 0.34 mg/ml (16μM) for Ras181, 0.26 mg/ml (12μM monomers) for Ras-2-Ras, and 0.11 mg/ml (5 μM monomers) and 0.40 mg/ml (18 μM) for two separate preparations of Ras-11-Ras.

Ionic strength of the buffer solution was change by addition of the equivalents of 5M NaCl stock solution (ionic strength effect on pH was found to be negligible).

The same procedure was applied for G-domain stability evaluation experiment to give Mant-GDP H-Ras C118S 1-166 concentration of 1.3 mg/ml (68μM). Equivalents of Mant-GDP labeled H-Ras C118S 1-166 were added to the series of buffers with a different pH in 1:10 (proteinsolution:buffer) ratio to 100μL of total volume:

- 20mM 2-(N-Morpholino)ethanesulfonic acid hydrate (MES) pH 6.0, 150mM NaCl, 1mM $MgCl_2$, 1.5mM NaN_3, 1mM DTT
- 20mM 4-(2-Hydroxyethyl)piperazine-1-ethanesulfonic acid (HEPES) pH 7.2, 150mM NaCl, 1mM $MgCl_2$, 1.5mM NaN_3, 1mM DTT
- 20mM 2-amino-2-(hydroxymethyl)-1,3-propanediol (TRIS) pH 8.0, 150mM NaCl, 1mM $MgCl_2$, 1.5mM NaN_3, 1mM DTT

POR expression and purification

Δ56 POR

Kanamycin resistant pET28.a plasmid containing POR genes carrying His-Tag was transformed into E.coli C41 (DE3) strains. Cell culture was allowed to grow in Luria Broth media at 37°C for 3 hours. Then protein overexpression was induced by addition of IPTG and riboflavin-5'-phosphate sodium salt (Bio-Rad) to 0.5 mM and 0.05 μM final concentration, respectively. The cell mixture was grown in the dark for 20 hours at room temperature and pelleted at 5000 g for 10 min. The cell pellet was resuspended in PBS buffer pH 7.4 (1 mM KH_2PO_4, 10 mM Na_2HPO_4, 137 mM NaCl, and 2.7 mM KCl) and sonicated on ice using Branson Sonifier 450. Supernatant obtained after cell lysate was centrifuged at 5000 g for 15 min and passed through

5mL His60 Ni Superflow resin (Clontech Lab) equilibrated with PBS buffer pH 7.4. Protein was eluted with 0.5 M imidazole in PBS buffer pH 7.4. Eluate was dialyzed vs PBS pH 7.4 with addition of 2 mM TCEP and passed through 2',5'-ADP Sepharose 4B (GE Healthcare Life Science) gravity column equilibrated with PBS buffer pH 7.4 (2mM DTT was used instead of TCEP). Protein was eluted using with PBS pH 7.4 buffer containing 20mM 2'(3')-AMP (Santa Cruz Biotechnology).

Purified sample was characterized with SDS-PAGE, UV-vis spectroscopy, cytochrome c assay, flavin quantification assay, Bradford assay and MALDI-TOF spectrometry.

Full-length POR

Ampillicin resistant pOR263 plasmid containing full-length POR genes and carrying His-Tag was transformed into E.coli C41 (DE3) cells. Cell culture was grown on Terrific Broth media at 37°C for 3 hours. Protein overexpression was induced by addition of IPTG to 0.5 mM final concentration and cell mixture was grown in the dark for 20 hours at 18°C. Cell culture was centrifuged at 5000 g and the cell pellet that was resuspended in 25 mM phosphate buffer pH 7.7, 100 mM NaCl, 10% glycerol with addition of one tablet of EDTA-free Complete Roche protease inhibitor (1836170) (using one tablet per each 1000 ml). Cells were lysed in the presence of 30 µg/ml lysozyme at 4°C for an hour followed by sonication on ice. The cell lysate was centrifuged at 5000g for 15min and obtained supernatant was centrifuged at 30,000 g for one hour. Pellet from second centrifugation was resuspended in 25 mM phosphate buffer pH 7.7, 100 mM NaCl, 0.3% Triton X-100, 10% glycerol, 2 mM TCEP, 1 mM PMSF with addition of the protease inhibitor and incubated overnight at 4°C to allow for detergent extraction of POR. Further purification was carried out according to the

procedure described above for Δ56 version of a protein. After the final step, to replace Triton X-100 in the POR sample with sodium cholate (necessary for nanodisc assembly), the final eluate was passed through Ni Superflow column, which was washed with 25mM sodium cholate (Alfa Aesar) and eluted with 0.5 M imidazole and 25mM sodium cholate.

Preparation of reduced and oxidized POR

Sample oxidation and reduction was carried out by adding 4-fold molar excess of $K_3[Fe(CN)_6]$ or NADPH, respectively. The concentrations of NADPH and $K_3[Fe(CN)_6]$ solutions were determined by specific absorption at ε (340 nm) = 6,220 M^{-1} cm^{-1} and ε (420 nm) = 1,040 M^{-1} cm^{1} , respectively[103, 104]. Preparation of reduced NMR samples was performed anaerobically in a glovebag (Glas-Col) filled with nitrogen gas.

POR-nanodisc preparation

Nanodisc assembly was performed according to the established protocols (see http://sligarlab.life.uiuc.edu/nanodisc/protocols.html). Briefly, a dry lipid mixture containing 15% 1,2-dioleoyl-*sn*-glycero-3-phospho-(1'-*rac*-glycerol) and 85% of 1,2-dioleoyl-*sn*-glycero-3-phosphocholine was dissolved in 100 mM sodium cholate, 100 mM phosphate, 50 mM NaCl pH 7.4 solution. The solution was sonicated and combined with aliquots of concentrated matrix scaffold protein MSP1D1 and His-tagged full-length Q157C/Q517C POR. Molar excess of MSP1D1 over POR (8:1) was used to ensure that most POR-nanodisc complexes will have one POR molecule per nanodisc. A buffer aliquot was added to adjust the cholate concentration to 20 mM in the final assembly mixture. To trigger nanodisc assembly, the detergent was

removed by dialysis in the presence of Amberlite XAD-2 beads (Sigma-Aldrich) added to the solvent outside of the dialysis bag (2 g of damp beads per each milliliter of assembly reaction mixture). To remove empty nanodiscs (without POR), the dialyzate was passed through

His60 Ni-Superflow resin. The POR-nanodisc complexes were eluted with 0.5 M imidazole and centrifuged 5 min at 15,000 g. The nanodisc preparation was passed through the Superose 6 Increase 10/300 column. The peak fractions corresponding to the molecular weight near 240 kDa were collected and concentrated.

POR flavin cofactor quantification assay

POR flavin cofactor quantification assay was performed as described in [101]. Specifically, 300µL of 5µM POR sample were incubated in AccuBlock digital dry bath (Labnet Inc) at 100 °C for 10 minutes. To ensure flavin stability Eppendorf tube was wrapped with aluminum foil. After that sample was centrifuged at 15000g for 10min at 4°C and supernatant was taken. UV-vis spectrum of the sample was recorded before and after denaturation and centrifugation steps. 100µL of the flavin cofactor solution were loaded into FCA3 cuvette (StarnaCel Inc) and sample fluorescence was recorded (slit size 2nm; λ_{ex}=450nm; λ_{em}=480-610nm). This was followed by addition of 3µL phosphodiesterase 1 (PDE) from *Crotalus adamanteus* venom (Millipore-SIGMA) with unit concentration of 2mU/µL and incubation in dark for 15 minutes and another step of fluorescence spectra acquisition. Fluorescence intensity at 525nm before (F_0) and after incubation (F_{fin}) with PDE was recorded and equation below was used to calculate FMN to FAD ratio(r).

$$r = \frac{10 \times \frac{F_{fin}}{F_0} - 10}{10 - \frac{F_{fin}}{F_0}}$$

Procedure was repeated at least 3 times for each protein sample and average value was calculated.

POR cytochrome c activity assay

POR cytochrome c activity assay was performed as described in [105] . Specifically, mixture containing 80µL of 0.5mM cytochrome c from horse heart (Crescent Chemical Co. inc), 10µL of 10µM POR sample and 900µL of 0.3M K_2HPO_4 (pH 7.7) was prepared. The mixture was used as an absorbance baseline at 550nm. After that 10µL of 10µM freshly prepared NADPH solution was added to the mixture and mixed thoroughly followed by recording of the reaction mixture absorbance at 550nm as a function of the time for 3min. Change in absorbance at 550nm (ΔA_{550}) was calculated for the first minute of acquisition and equation bellow was used to calculate specific activity of POR sample.

$$S = \frac{\Delta A_{550}}{0.021 \ {}^{au}/_{nmol\ cyt\ c} \times 0.1}$$

Relative protein activity was calculated on as a percentage of a specific activity of the wild-type POR activity (3000 nmol of cyt c reduced per min per nmol of POR [106]). After Procedure was repeated at least 3 times for each protein sample and average value was calculated

Bradford assay

Bradford assay was performed using kit Pierce™ Coomassie Plus (Bradford) Assay Kit (ThermoFisher). In the Eppendorf tube 4µL of the protein sample was mixed with

200µL of Coomassie reagent after that mixture was vortexed for 15 seconds and incubated on the bench for 10min. After that absorbance at 595nm wavelength was recorded on . Protein concentration was calculated using calibration curve that was built based on Bovine serum albumin solutions standard concentrations. Procedure was repeated at least 3 times for each protein sample and average value was calculated.

MSP protein expression and purification

Protein expression and purification protocol was performed as described in [63]. Specifically, kanamycin resistant pET28.a plasmid containing MSP1D1 or MSP1E3D1 genes carrying His-Tag with TEV-cleavage site was transformed into E.coli BL21(DE3) strains. Cell culture was allowed to grow in Luria Broth media at 37°C for 3 hours. Then protein overexpression was induced by addition of IPTG to 1 mM final concentration. The cell mixture was grown for 3-4 hours at 37°C and pelleted at 5000 g for 15 min. The cell pellet was resuspended in 20mM TRIS pH 8.0, 1mM PMSF, 0.5mM TCEP, 1% Triton X100 buffer for cell lysis and sonicated on ice using Branson Sonifier 450. Supernatant obtained after cell lysate was centrifuged at 15000 g for 1 hour and passed through 5mL His60 Ni Superflow resin (Clontech Lab) equilibrated with lysis buffer pH 8.0. Column was washed with 50mL of Wash Buffer 1, pH 8.0 (20 mM TRIS, 0.5mM TCEP, 500mM NaCl, 1% Triton) followed by 50mL of Wash Buffer 2, pH 8.0 (20 mM TRIS, 0.5mM TCEP, 500mM NaCl, 50mM Sodium Cholate) and 50mL of Wash Buffer 3, pH 8.0 (20 mM TRIS pH 8.0, 0.5mM TCEP, 500mM NaCl, 50mM imidazole). Protein was eluted with elution buffer containing 0.5 M imidazole, TRIS pH 8.0, 500mM NaCl. Eluate was dialyzed vs 20 mM TRIS pH 8.0, 200mM NaCl and injected into XK16/40 column packed with

Aca54 gel-filtration resin (Pall Life Sciences) preliminary equilibrated with the dialysis buffer and eluted using dialysis buffer at expected elution volume corresponding to MSP protein hydrodynamic radius. Eluate was concentrated with Amicon Ulra-15 centrifugal filter concentrator (Milipore) and incubated in a presence of TEV protease for 16 hours at 4°C. After that sample was passed through the His60 Ni Superflow resin (Clontech Lab) equilibrated with 20 mM TRIS pH 8.0, 200mM NaCl solution and column flow-through containing MSP protein lacking His-tag was collected. Purified protein samples were concentrated with Amicon Ulra-15 centrifugal filter concentrator (Milipore) and were characterized with SDS-PAGE, Bradford assay, UV-vis spectroscopy and MALDI-TOF spectrometry.

MALDI-TOF mass-spectrometry

MALDI-TOF mass spectra were recorded on a Voyager-DE ProBioSpectrometryTM workstation PerSeptive Biosystems with sinapinic acid (SA) (Fluka) as matrix for the proteins with molecular weight less than 30kDa.

To obtain MALDI-TOF mass spectra for proteins with molecular weight >40kDa, 1:1 mixture of dihydroxybenzoic acid (DHB) (TCI) α-Cyano-4-hydroxycinnamic acid (α-CHCA) (Fluka) was prepared. Before matrix-protein mixture was applied, MALDI-TOF plate was preliminary covered with the thin layer of saturated α-CHCA matrix solution to increase signal to noise ratio.

Polyacrylamide gel electrophoresis

SDS-PAGE was performed by using phastgel gradient 8-25 gels (GE Healthcare Life Sciences) on PhastSystem for Automated Electrophoresis(Pharmacia) or Mini-PROTEAN Electrophoresis cell (Biorad) powered PowerEase500 (Invitrogen Life

Technologies) with a prepared 10% and 15% SDS-PAGE gels (AA Hoefer Inc) . Gels were stained by Coomassie Brilliant Blue stain (Thermo Scientific).

Fast Protein Liquid chromatography (FPLC)

FPLC purifications were performed on a High Pressure/ Fast Protein Liquid Chromatography station (Shimadzu): CBM-20A(Controller), LC-20AT (Pump), DGU-20A5(Degasser), FCV-12AH(Valve), SPD-M20A(Detector), FRC-10A(Fraction collector).

Fluorescence measurements

Fluorescence polarization anisotropy

General parameters

Fluorescence 2D spectra acquisition and polarization anisotropy measurements were performed in a QuantaMaster™ 400 Research Fluorometer (PTI) equipped with PicoMaster 1 TCSPC and Peltier-based Turret 400 for a temperature control. Samples were loaded into 3mm microcells (StarnaCells Inc). For polarization anisotropy MANT-GDP fluorophore was excited using 365nm LED, while the emission was detected at 440 nm with 24nm slit widths. The polarized fluorescence decays were recorded with the Glan-Thompson polarizers and the emission slits at 24 nm with TCSPC counting rate kept below 2%. To measure a G-factor at 440 nm steady-state Xenon lamp excitation was used, while the instrument response functions (IRF) were recorded from a investigated protein solution.

Fluorescence 2D spectra

2D fluorescence spectra were obtained by acquiring series of fluorescence emission scans in 5nm step for 250nm to 700nm range. Scans were set up in the way that the first emission scan 250-700nm was acquired for 700nm excitation wavelength; next emission was recorded for 260-695nm range for 695nm excitation wavelength and so on. The slits width for both excitation and emission was set to 5nm.

Raw traces obtained from the series of emission scans were converted to 2D fluorescence spectra with Fluorescence2D software[107].

Details of the experiment on G-domain propensity to form dimers

Experiments were repeated multiple times with 30-60 min for one acquisition time per position of emission polarizer. The runs were averaged during data processing. Polarization anisotropy decays were collected for 3 three temperatures (20, 25, and 37$_o$C) and three NaCl concentrations and three (0, 150, and 300 mM).

To analyze anisotropy decays, AniFit software (kindly shared by Søren Preus; available from www.fluortools.com) was used to apply a global fitting of differently polarized components of emission to anisotropy decay laws. Scattering of the light was included in fitting procedure by addition of a adjustable coefficient. Fitting procedure involved single and double-exponential anisotropy decay laws, although there was no significant difference observed for slow rotational correlation time between those two fitting procedures.

Details of G-domain stability investigation

Polarization anisotropy decay traces were acquired for temperature range from 20°C to 100°C. To do that the temperature ramp was applied as 1°C/min. Experiment was repeated twice for each buffer conditions.

Anisotropy decay data was analyzed by matlab script ptiFitMeltCurve.m (written by Dr. E. Kovrigin) to provide normalized denaturation curves that were fitted to van't Hoff's equation to result denaturation midpoints values.

NMR spectroscopy

2D ^{15}N-^{1}H Heteronuclear Single-Quantum Correlation (HSQC) and ^{13}C-^{1}H Heteronuclear Multiple-Quantum Correlation (HMQC) NMR spectra will be recorded on 600 MHz Varian VNMR-S spectrometer with the Crio Probe installed. To allow NMR spectrometer locking 10%D_2O will be added to the protein samples and loaded into a Shigemi tubes. Spectra will be processed with NMRPipe [108] and Sparky[109] software. ^{15}N-^{1}H HSQC signal assignments for H-Ras G-domain will be performed by overlaying with a wild-type H-Ras, residues 1-166, GDP-loaded spectra assigned previously. ^{13}C-^{1}H HMQC MTC-labels signal assignment will be performed by overlaying "cys-less" POR variant with single-cysteine mutants.

$^{13}CH_3$- MMTS-labeling

Purified protein sample was incubated with 5mM dithiothreitol **(**DTT) (VWR Life Science AMRESCO) overnight in phosphate-buffered saline (PBS, 1 mM KH_2PO_4, 10mM Na_2HPO4, 137mM NaCl, and 2.7mM KCl, pH 7.4) and dialyzed using Slide-A-Lyzer Dialysis Cassettes, 10000 MCWO, 0.5-3 mL (Thermo Scientific) against degassed 50 mM potassium phosphate, pH 7.5, 1 mM EDTA at 4°C. Then sample was concentrated with Vivaspin®2 Centrifugal Concentrator 10000 MCWO, 0.4-2mL

(GE Healthcare Life) to 300µL volume. After that 100mM $^{13}CH_3$- MMTS (Thermo Scientific) DMSO stock solution (stored at -20°C) was added in 50% molar excess to a protein solution and incubated overnight at 4°C. Reaction was stopped by dialysis against PBS using Slide-A-Lyzer Dialysis Cassettes, 5000 MCWO, 0.1-0.5mL. It is important to remove any agent capable of reducing disulfide bond, such as DTT, from buffers.

V. SUMMARY

Increasing number of attention is being paid to macromolecular systems such membrane proteins. Membrane proteins experience numerous interactions on the membrane surface that play a vital role in determining the behavior. Therefore, investigating these interactions is very important but challenging process; our approach allows to address challenges of those systems.

Systems containing peripheral membrane proteins that demonstrate high level of mobility cannot be studied by X-ray spectroscopy. The most common way to study macromolecular systems like that by means of solid state NMR for now still remains state of the art technique.

In my dissertation we demonstrated how one can investigate those interaction separately (Ras dimerization hypothesis) or in a complex system (conformational changes in NADPH-cytochrome P450 oxidoreductase during its redox cycle) by means of solution NMR and fluorescence studies.

In the first project, we investigated the hypothesis of Ras dimerization on the membrane surface due to protein--protein interaction. First of all, we researched the buffer conditions we planed to perform our further experiments in and also confirmed that fluorescence labeling will not affect stability of the protein. After that, we utilized polarization anisotropy to evaluate the propensity of Ras G-domain to form dimer by cross-linking two Ras molecules and measuring it rotational correlation times. The conclusion that was drawn was that G-domain does not drive dimerization of Ras protein as it has been hypothesized and all observations in the literature were either due to presence of the membrane or experimental setup.

In our second project we proposed a technique that can be used to reveal structural details of a membrane protein interactions and conformational changes it undergoes during its cycle.

As the object of our study we selected NADPH-cytochrome P450 oxidoreductase (POR) that is involved in electron transport chain and transfers electrons to cytochrome P450 and other oxygenazes. We demonstrated that extrinsic labels introduced on the surface of the protein were differentially sensitive towards protein reduction and conformational changes on the soluble version of the protein. After that we utilized extrinsic labeling technique in combination with Methyl-TROSY NMR spectroscopy on the full-length protein imbedded on the lipid nanodisc and observed detectable signals. Moreover, signals demonstrated similar behavior as in a soluble construct. Thus, we have shown that our approach can be further applied to investigate protein-protein and protein-lipid interactions on a challenging protein-lipid complexes even in the presence of unpaired electrons.

One of the greatest advantages is that our approach doesn't require sample deuteration this significantly decreases the cost. Moreover, in our case signals were obtained on 600MHz instrument that can be considered a standard system in any institution that has projects investigating biomolecular systems while generally higher field instrument such 800 or 900 MHz are typically used in a most of researches.

REFERENCES

1. Luckey, M., *Membrane Structural Biology with Biochemical and Biophysical Foundations*2011, Cambridge: Cambridge University Press. 332.

2. van Meer, G. and A.I. de Kroon, *Lipid map of the mammalian cell.* J Cell Sci, 2011. **124**(Pt 1): p. 5-8.

3. Bitounis, D., et al., *Optimizing Druggability through Liposomal Formulations: New Approaches to an Old Concept.* ISRN Pharm, 2012. **2012**: p. 738432.

4. Marsh, D., *Handbook of lipid bilayers*. 2nd ed2013, Boca Raton, FL.: CRC Press, Taylor & Francis Group. xxvii, 1,145 p.

5. Singer, S.J. and G.L. Nicolson, *The fluid mosaic model of the structure of cell membranes.* Science, 1972. **175**(4023): p. 720-31.

6. Nicolson, G.L., *The Fluid-Mosaic Model of Membrane Structure: still relevant to understanding the structure, function and dynamics of biological membranes after more than 40 years.* Biochim Biophys Acta, 2014. **1838**(6): p. 1451-66.

7. Thomas, S., et al., *Analysis of lipid rafts in T cells.* Mol Immunol, 2004. **41**(4): p. 399-409.

8. Saslowsky, D.E., et al., *Placental alkaline phosphatase is efficiently targeted to rafts in supported lipid bilayers.* J Biol Chem, 2002. **277**(30): p. 26966-70.

9. Palade, G.E., *Fine structure of blood capillaries.* Journal of Applied Physics, 1953. **24**: p. 1424.

10. Pike, L.J., *The challenge of lipid rafts.* J Lipid Res, 2009. **50 Suppl**: p. S323-8.

11. Anchisi, L., et al., *Cholesterol homeostasis: a key to prevent or slow down neurodegeneration.* Front Physiol, 2012. **3**: p. 486.

12. Lehninger, A.L., D.L. Nelson, and M.M. Cox, *Lehninger principles of biochemistry*. 4th ed2005, New York: W.H. Freeman.

13. Testi, R., *Sphingomyelin breakdown and cell fate.* Trends Biochem Sci, 1996. **21**(12): p. 468-71.

14. Prior, I.A., et al., *GTP-dependent segregation of H-ras from lipid rafts is required for biological activity.* Nature Cell Biology, 2001. **3**(4): p. 368-375.

15. Lin, Q. and E. London, *Ordered raft domains induced by outer leaflet sphingomyelin in cholesterol-rich asymmetric vesicles.* Biophys J, 2015. **108**(9): p. 2212-22.

16. Krogh, A., et al., *Predicting transmembrane protein topology with a hidden Markov model: application to complete genomes.* J Mol Biol, 2001. **305**(3): p. 567-80.

17. Overington, J.P., B. Al-Lazikani, and A.L. Hopkins, *Opinion - How many drug targets are there?* Nature Reviews Drug Discovery, 2006. **5**(12): p. 993-996.

18. Downward, J., *Targeting ras signalling pathways in cancer therapy.* Nature Reviews Cancer, 2003. **3**(1): p. 11-22.

19. Voice, J.K., et al., *Four Human Ras Homologs Differ in Their Abilities to Activate Raf-1, Induce Transformation, and Stimulate Cell Motility 10.1074/jbc.274.24.17164.* J. Biol. Chem., 1999. **274**(24): p. 17164-17170.

20. Shima, F. and T. Kataoka, *Critical role of posttranslational modification of Ras proteins in effector activation.* Seikagaku, 2005. **77**(6): p. 519-526.

21. Reiss, Y., et al., *Inhibition of purified p21ras farnesyl:protein transferase by Cys-AAX tetrapeptides.* Cell, 1990. **62**(1): p. 81-8.

22. Dai, Q., et al., *Mammalian prenylcysteine carboxyl methyltransferase is in the endoplasmic reticulum.* J Biol Chem, 1998. **273**(24): p. 15030-4.

23. Apolloni, A., et al., *H-ras but Not K-ras Traffics to the Plasma Membrane through the Exocytic Pathway.* Mol. Cell. Biol., 2000. **20**(7): p. 2475-2487.

24. Scheffzek, K. and M. Ahmadian, *GTPase activating proteins: structural and functional insights 18 years after discovery.* Cellular and Molecular Life Sciences, 2005. **62**(24): p. 3014-3038.

25. Melkonian, K.A., et al., *Role of Lipid Modifications in Targeting Proteins to Detergent-resistant Membrane Rafts. MANY RAFT PROTEINS ARE ACYLATED, WHILE FEW ARE PRENYLATED 10.1074/jbc.274.6.3910.* J. Biol. Chem., 1999. **274**(6): p. 3910-3917.

26. Vogel, A., et al., *Interaction of the human N-Ras protein with lipid raft model membranes of varying degrees of complexity.* Biological Chemistry, 2014. **395**(7-8): p. 779-789.

27. Niv, H., et al., *Activated K-Ras and H-Ras display different interactions with saturable nonraft sites at the surface of live cells.* Journal of Cell Biology, 2002. **157**(5): p. 865-872.

28. Hancock, J.F., *Ras Proteins: Different Signals from Different Locations.* Nature Reviews Molecular Cell Biology, 2003. **4**(5): p. 373-385.

29. Werkmuller, A., *Rotational and Translational Dynamics of Ras Proteins upon Binding to Model Membrane Systems.* ChemPhysChem, 2013. **14**: p. 3698 – 3705.

30. Inouye, K., et al., *Formation of the Ras Dimer Is Essential for Raf-1 Activation.* J. Biol. Chem., 2000. **275**(6): p. 3737-3740.

31. Kang, P.J., et al., *The Rsr1/Bud1 GTPase interacts with itself and the Cdc42 GTPase during bud-site selection and polarity establishment in budding yeast.* Mol Biol Cell, 2010. **21**(17): p. 3007-16.

32. Wittmann, J.G. and M.G. Rudolph, *Crystal structure of Rab9 complexed to GDP reveals a dimer with an active conformation of switch II.* FEBS Letters, 2004. **568**(1-3): p. 23-29.

33. Rajakulendran, T., et al., *A dimerization-dependent mechanism drives RAF catalytic activation.* Nature, 2009. **461**(7263): p. 542-U114.

34. Guldenhaupt, J., et al., *N-Ras Forms Dimers at POPC Membranes.* Biophysical Journal, 2012. **103**(7): p. 1585-1593.

35. Lin, W.-C., et al., *H-Ras forms dimers on membrane surfaces via a protein–protein interface.* Proceedings of the National Academy of Sciences, 2014. **111**(8): p. 2996-3001.

36. Muratcioglu, S., et al., *GTP-Dependent K-Ras Dimerization.* Structure, 2015. **23**(7): p. 1325-1335.

37. Fetics, S.K., et al., *Allosteric Effects of the Oncogenic RasQ61L Mutant on Raf-RBD.* Structure, 2015. **23**(3): p. 505-516.

38. Bertz, R.J. and G.R. Granneman, *Use of in vitro and in vivo data to estimate the likelihood of metabolic pharmacokinetic interactions.* Clin Pharmacokinet, 1997. **32**(3): p. 210-58.

39. Iyanagi, T., C. Xia, and J.J. Kim, *NADPH-cytochrome P450 oxidoreductase: prototypic member of the diflavin reductase family.* Arch Biochem Biophys, 2012. **528**(1): p. 72-89.

40. Huang, R., et al., *Probing the Transmembrane Structure and Dynamics of Microsomal NADPH-cytochrome P450 oxidoreductase by Solid-State NMR.* Biophysical Journal, 2014. **106**(10): p. 2126-2133.

41. Waskell, L. and J.-J.P. Kim, *Electron Transfer Partners of Cytochrome P450*, in *Cytochrome P450. Structure, Mechanism, and Biochemistry* P.R. Ortiz de Montellano, Editor 2015, Springer Cham Heidelberg New York Dordrecht London. p. 33-68.

42. Hamdane, D., et al., *Structure and function of an NADPH-cytochrome P450 oxidoreductase in an open conformation capable of reducing cytochrome P450.* J Biol Chem, 2009. **284**(17): p. 11374-84.

43. Gilep, A.A., et al., *An enzymatically active chimeric protein containing the hydrophilic form of NADPH-cytochrome P450 reductase fused to the membrane-binding domain of cytochrome b5.* Biochem Biophys Res Commun, 2001. **284**(4): p. 937-41.

44. Das, A. and S.G. Sligar, *Modulation of the cytochrome P450 reductase redox potential by the phospholipid bilayer.* Biochemistry, 2009. **48**(51): p. 12104-12.

45. Narayanasami, R., P.M. Horowitz, and B.S. Masters, *Flavin-binding and protein structural integrity studies on NADPH-cytochrome P450 reductase are consistent with the presence of distinct domains.* Arch Biochem Biophys, 1995. **316**(1): p. 267-74.

46. Shen, A.L. and C.B. Kasper, *Differential contributions of NADPH-cytochrome P450 oxidoreductase FAD binding site residues to flavin binding and catalysis.* J Biol Chem, 2000. **275**(52): p. 41087-91.

47. Gutierrez, A., et al., *Trp-676 facilitates nicotinamide coenzyme exchange in the reductive half-reaction of human cytochrome P450 reductase: properties of the soluble W676H and W676A mutant reductases.* Biochemistry, 2000. **39**(51): p. 15990-9.

48. Hubbard, P.A., et al., *NADPH-cytochrome P450 oxidoreductase. Structural basis for hydride and electron transfer.* J Biol Chem, 2001. **276**(31): p. 29163-70.

49. Xia, C., et al., *Conformational changes of NADPH-cytochrome P450 oxidoreductase are essential for catalysis and cofactor binding.* J Biol Chem, 2011. **286**(18): p. 16246-60.

50. Shen, A.L., et al., *Structural analysis of the FMN binding domain of NADPH-cytochrome P-450 oxidoreductase by site-directed mutagenesis.* J Biol Chem, 1989. **264**(13): p. 7584-9.

51. Takashi Iyanagi , R.M., F. Koichi Anan, *Studies on the microsomal mixed-function oxidase system: mechanism of action of hepatic NADPH-cytochrome P-450 reductase.* Biochemistry, 1981. **20**(7): p. 1722-1730.

52. Sevrioukova, I.F., et al., *Structure of a cytochrome P450-redox partner electron-transfer complex.* Proc Natl Acad Sci U S A, 1999. **96**(5): p. 1863-8.

53. Shen, A.L. and C.B. Kasper, *Role of acidic residues in the interaction of NADPH-cytochrome P450 oxidoreductase with cytochrome P450 and cytochrome c.* J Biol Chem, 1995. **270**(46): p. 27475-80.

54. Jang, H.H., et al., *Beta sheet 2-alpha helix C loop of cytochrome P450 reductase serves as a docking site for redox partners.* Biochim Biophys Acta, 2010. **1804**(6): p. 1285-93.

55. Wei-Cheng Huang, J.E., Peter C.E. Moody, Emma L. Raven, , Gordon C.K. Roberts, *Redox-Linked Domain Movements in the Catalytic Cycle of Cytochrome P450 Reductase.* Structure, 2013. **21**(9): p. 1581-1589.

56. Brenner, S., et al., *Inter-flavin electron transfer in cytochrome P450 reductase - effects of solvent and pH identify hidden complexity in mechanism.* FEBS J, 2008. **275**(18): p. 4540-57.

57. Gutierrez, A., et al., *Relaxation kinetics of cytochrome P450 reductase: internal electron transfer is limited by conformational change and regulated by coenzyme binding.* Biochemistry, 2002. **41**(14): p. 4626-37.

58. Bayburt, T.H. and S.G. Sligar, *Membrane protein assembly into Nanodiscs.* FEBS Lett, 2010. **584**(9): p. 1721-7.

59. Bayburt, T.H., Y.V. Grinkova, and S.G. Sligar, *Self-assembly of discoidal phospholipid bilayer nanoparticles with membrane scaffold proteins.* Nano Lett, 2002. **2**: p. 853-856.

60. Hagn, F., et al., *Optimized Phospholipid Bilayer Nanodiscs Facilitate High-Resolution Structure Determination of Membrane Proteins.* J Am Chem Soc, 2013. **135**: p. 1919-1925.

61. Nath, A., W.M. Atkins, and S.G. Sligar, *Applications of Phospholipid Bilayer Nanodiscs in the Study of Membranes and Membrane Proteins.* Biochemistry, 2007. **46**(8): p. 2059-2069.

62. Denisov, I.G., et al., *Cooperativity in cytochrome P450 3A4: linkages in substrate binding, spin state, uncoupling, and product formation.* J Biol Chem, 2007. **282**(10): p. 7066-76.

63. Denisov, I.G. and S.G. Sligar, *Cytochromes P450 in Nanodiscs.* Biochimica et Biophysica Acta (BBA) - Proteins & Proteomics, 2011. **1814**(1): p. 223-229.

64. Kobashigawa, Y., et al., *Phosphoinositide-incorporated lipid-protein nanodiscs: A tool for studying protein-lipid interactions.* Anal Biochem, 2011. **410**(1): p. 77-83.

65. Pervushin, K., et al., *Attenuated T-2 relaxation by mutual cancellation of dipole-dipole coupling and chemical shift anisotropy indicates an avenue to NMR structures of very large biological macromolecules in solution.* Proceedings of the National Academy of Sciences of the United States of America, 1997. **94**(23): p. 12366-12371.

66. Tugarinov, V., et al., *Cross-correlated relaxation enhanced H-1-C-13 NMR spectroscopy of methyl groups in very high molecular weight proteins and protein complexes.* Journal of the American Chemical Society, 2003. **125**(34): p. 10420-10428.

67. Ollerenshaw, J.E., V. Tugarinov, and L.E. Kay, *Methyl TROSY: explanation and experimental verification.* Magnetic Resonance in Chemistry, 2003. **41**(10): p. 843-852.

68. Kay, L.E., *NMR studies of protein structure and dynamics.* Journal of Magnetic Resonance, 2005. **173**(2): p. 193-207.

69. Rosenzweig, R., et al., *Unraveling the mechanism of protein disaggregation through a ClpB-DnaK interaction.* Science, 2013. **339**(6123): p. 1080-3.

70. Religa, T.L., R. Sprangers, and L.E. Kay, *Dynamic regulation of archaeal proteasome gate opening as studied by TROSY NMR.* Science, 2010. **328**(5974): p. 98-102.

71. Religa, T.L., et al., *Site-directed methyl group labeling as an NMR probe of structure and dynamics in supramolecular protein systems: applications to the proteasome and to the ClpP protease.* J Am Chem Soc, 2011. **133**(23): p. 9063-8.

72. Solomon, I., *Relaxation Processes in a System of Two Spins.* Physical Review, 1955. **99**: p. 559– 565.

73. Cook, G.A. and S.J. Opella, *Secondary structure, dynamics, and architecture of the p7 membrane protein from hepatitis C virus by NMR spectroscopy.* Biochim Biophys Acta, 2011. **1808**(6): p. 1448-53.

74. Wang, S., et al., *Paramagnetic relaxation enhancement reveals oligomerization interface of a membrane protein.* J Am Chem Soc, 2012. **134**(41): p. 16995-8.

75. Gueron, M., *Nuclear relaxation in macromolecules by paramagnetic ions—novel mechanism.* Journal of Magnetic Resonance, 1975. **19**: p. 58-66.

76. Bertini, I., et al., *Cross correlation between the dipole-dipole interaction and the Curie spin relaxation: the effect of anisotropic magnetic susceptibility.* J Magn Reson, 2001. **152**(1): p. 103-8.

77. Battiste, J.L. and G. Wagner, *Utilization of site-directed spin labeling and high-resolution heteronuclear nuclear magnetic resonance for global fold determination of large proteins with limited nuclear overhauser effect data.* Biochemistry, 2000. **39**(18): p. 5355-65.

78. Pintacuda, G., et al., *Site-specific labelling with a metal chelator for protein-structure refinement.* J Biomol NMR, 2004. **29**(3): p. 351-61.

79. Liu, Y.Z., R.A. Kahn, and J.H. Prestegard, *Dynamic structure of membrane-anchored Arf center dot GTP.* Nature Structural & Molecular Biology, 2010. **17**(7): p. 876-U128.

80. Mazhab-Jafari, M.T., et al., *Membrane-Dependent Modulation of the mTOR Activator Rheb: NMR Observations of a GTPase Tethered to a Lipid-Bilayer Nanodisc.* Journal of the American Chemical Society, 2013. **135**(9): p. 3367-3370.

81. Lakowicz, J.R., *Principles of Fluorescence Spectroscopy*. 3rd ed2010: Springer. 954.

82. Werkmuller, A., et al., *Rotational and Translational Dynamics of Ras Proteins upon Binding to Model Membrane Systems.* Chemphyschem, 2013. **14**(16): p. 3698-3705.

83. Ahmadian, M.R., A. Wittinghofer, and C. Herrmann, *Fluorescence methods in the study of small GTP-binding proteins.* Methods Mol Biol, 2002. **189**: p. 45-63.

84. Wittinghofer, A. and I.R. Vetter, *Structure-Function Relationships of the G Domain, a Canonical Switch Motif*, in *Annual Review of Biochemistry*, R.D. Kornberg, et al., Editors. 2011, Annual Reviews: Palo Alto. p. 943-971.

85. Zent, E. and A. Wittinghofer, *Human septin isoforms and the GDP-GTP cycle.* Biological Chemistry, 2014. **395**(2): p. 169-180.

86. Santos, E., et al., *Oligomeric Structure of p21 Ras Proteins as Determined by Radiation Inactivation.* Journal of Biological Chemistry, 1988. **263**(20): p. 9853-9858.

87. Smyth, D.G., O.O. Blumenfeld, and W. Konigsberg, *Reaction of N-ehtylmaleimide with peptides and amino acids.* Biochemical Journal, 1964. **91**: p. 589.

88. Chung, J.K., et al., *K-Ras4B Remains Monomeric on Membranes over a Wide Range of Surface Densities and Lipid Compositions.* Biophysical Journal, 2018. **114**(1): p. 137-145.

89. Liu, K.C., et al., *Liver microsomal lipid enhances the activity and redox coupling of colocalized cytochrome P450 reductase-cytochrome P450 3A4 in nanodiscs.* Febs Journal, 2017. **284**(14): p. 2302-2319.

90. Riddick, D.S., et al., *NADPH-cytochrome P450 oxidoreductase: roles in physiology, pharmacology, and toxicology.* Drug Metab Dispos, 2013. **41**(1): p. 12-23.

91. Fluck, C.E., C. Nicolo, and A.V. Pandey, *Clinical, structural and functional implications of mutations and polymorphisms in human NADPH P450 oxidoreductase.* Fundam Clin Pharmacol, 2007. **21**(4): p. 399-410.

92. Vincent, B., et al., *The closed and compact domain organization of the 70-kDa human cytochrome P450 reductase in its oxidized state as revealed by NMR.* J Mol Biol, 2012. **420**(4-5): p. 296-309.

93. Spencer, A.L.M., et al., *Protein/Protein Interactions in the Mammalian Heme Degradation Pathway. Heme Oxygenase-2, Cytochrome P450 Reductase, and Bileverdin Reductase.* Journal of Biological Chemistry, 2014. **289**(43): p. 29836-29858.

94. Huang, R., et al., *Kinetic and structural characterization of the interaction between the FMN binding domain of cytochrome P450 reductase and cytochrome c.* J Biol Chem, 2015. **290**(8): p. 4843-55.

95. Estrada, D.F., J.S. Laurence, and E.E. Scott, *Cytochrome P450 17A1 Interactions with the FMN Domain of Its Reductase as Characterized by NMR.* J Biol Chem, 2016. **291**(8): p. 3990-4003.

96. Zhang, Z., et al., *A greedy algorithm for aligning DNA sequences.* J Comput Biol, 2000. **7**(1-2): p. 203-14.

97. Rwere, F., et al., *Mutants of Cytochrome P450 Reductase Lacking Either Gly-141 or Gly-143 Destabilize Its FMN Semiquinone.* Journal of Biological Chemistry, 2016. **291**(28): p. 14639-14661.

98. Elmore, C.L. and T.D. Porter, *Modification of the Nucleotide Cofactor-binding Site of Cytochrome P-450 Reductase to Enhance Turnover with NADH in Vivo.* Journal of Biological Chemistry, 2002. **277**(50): p. 48960-48964.

99. Verma, M., A. Vats, and V. Taneja, *Toxic species in amyloid disorders: Oligomers or mature fibrils.* Annals of Indian Academy of Neurology, 2015. **18**(2): p. 138-145.

100. Barnaba, C., et al., *The catalytic function of cytochrome P450 is entwined with its membrane-bound nature.* F1000Research, 2017. **6:662**.

101. Aliverti, A., B. Curti, and M.A. Vanoni, *Identifying and Quantitating FAD and FMN in Simple and in Iron-Sulfur-Containing Flavoproteins*, in *Flavoprotein Protocols*, S.K. Chapman and G.A. Reid, Editors. 1999, Humana Press: Totowa, NJ. p. 9-23.

102. Ritchie, T.K., et al., *Chapter 11 - Reconstitution of membrane proteins in phospholipid bilayer nanodiscs.* Methods Enzymol, 2009. **464**: p. 211-31.

103. Fruscione, F., et al., *Differential role of NADP(+) and NADPH in the activity and structure of GDP-D-mannose 4,6-dehydratase from two chlorella viruses.* Journal of Biological Chemistry, 2008. **283**(1): p. 184-193.

104. Appleby, C.A. and R.K. Morton, *Lactic Dehydrogenase and Cytochrome B2 of Bakers Yeast - Enzymic and Chemical Properties of the Crystalline Enzyme.* Biochemical Journal, 1959. **73**: p. 539-550.

105. Guengerich, F.P., et al., *Measurement of cytochrome P450 and NADPH-cytochrome P450 reductase.* Nat Protoc, 2009. **4**(9): p. 1245-51.

106. Guengerich, F.P. and M.V. Martin, *Purification of cytochrome P-450, NADPH-cytochrome P-450 reductase, and epoxide hydratase from a single preparation of rat liver microsomes.* Archives of Biochemistry and Biophysics. **205**(2): p. 365-379.

107. Kovrigin, E.L., *Fluorescence2D: Software for Accelerated Acquisition and Analysis of Two-Dimensional Fluorescence Spectra.* PLoS One, 2014. **9**(7): p. e101227.

108. Delaglio, F., et al., *NMRPipe: a multidimensional spectral processing system based on UNIX pipes.* J Biomol NMR, 1995. **6**(3): p. 277-93.

109. Goddard, T.D. and D.G. Kneller, *SPARKY 3;* http://www.cgl.ucsf.edu/home/sparky/, University of California, San Francisco.

APPENDIX

Protein sequences

H-Ras C118S 1-166 amino acid sequence

```
        10          20          30          40          50          60
MTEYKLVVVG AGGVGKSALT IQLIQNHFVD EYDPTIEDSY RKQVVIDGET CLLDILDTAG

        70          80          90         100         110         120
QEEYSAMRDQ YMRTGEGFLC VFAINNTKSF EDIHQYREQI KRVKDSDDVP MVLVGNKSDL

       130         140         150         160
AARTVESRQA QDLARSYGIP YIETSAKTRQ GVEDAFYTLV REIRQH
```

H-Ras C118S 1-181 amino acid sequence

```
        10          20          30          40          50          60
MTEYKLVVVG AGGVGKSALT IQLIQNHFVD EYDPTIEDSY RKQVVIDGET CLLDILDTAG

        70          80          90         100         110         120
QEEYSAMRDQ YMRTGEGFLC VFAINNTKSF EDIHQYREQI KRVKDSDDVP MVLVGNKSDL

       130         140         150         160         170         180
AARTVESRQA QDLARSYGIP YIETSAKTRQ GVEDAFYTLV REIRQHKLRK LNPPDESGPG

C
```

His-tagged MSP1D1 amino acid sequence

```
        10          20          30          40          50          60
MGHHHHHHHD YDIPTTENLY FQGSTFSKLR EQLGPVTQEF WDNLEKETEG LRQEMSKDLE

        70          80          90         100         110         120
EVKAKVQPYL DDFQKKWQEE MELYRQKVEP LRAELQEGAR QKLHELQEKL SPLGEEMRDR

       130         140         150         160         170         180
ARAHVDALRT HLAPYSDELR QRLAARLEAL KENGGARLAE YHAKATEHLS TLSEKAKPAL

       190         200         210
EDLRQGLLPV LESFKVSFLS ALEEYTKKLN TQ
```

His-tagged MSP1E3D1 amino acid sequence

```
        10          20          30          40          50          60
MGHHHHHHHD YDIPTTENLY FQGSTFSKLR EQLGPVTQEF WDNLEKETEG LRQEMSKDLE

        70          80          90         100         110         120
EVKAKVQPYL DDFQKKWQEE MELYRQKVEP LRAELQEGAR QKLHELQEKL SPLGEEMRDR

       130         140         150         160         170         180
ARAHVDALRT HLAPYLDDFQ KKWQEEMELY RQKVEPLRAE LQEGARQKLH ELQEKLSPLG

       190         200         210         220         230         240
EEMRDRARAH VDALRTHLAP YSDELRQRLA ARLEALKENG GARLAEYHAK ATEHLSTLSE

       250         260         270
KAKPALEDLR QGLLPVLESF KVSFLSALEE YTKKLNTQ
```

His-tagged POR 56-678 cysless amino acid sequence

```
        10          20          30          40          50          60
MGSSHHHHHH SSGLVPRGSH MIQTTAPPVK ESSFVEKMKK TGRNIIVFYG SQTGTAEEFA
```

```
        70          80          90         100         110         120
NRLSKDAHRY GMRGMSADPE EYDLADLSSL PEIDKSLVVF AMATYGEGDP TDNAQDFYDW

       130         140         150         160         170         180
LQETDVDLTG VKFAVFGLGN KTYEHFNAMG KYVDQRLEQL GAQRIFELGL GDDDGNLEED

       190         200         210         220         230         240
FITWREQFWP AVAEFFGVEA TGEESSIRQY ELVVHEDMDV AKVYTGEMGR LKSYENQKPP

       250         260         270         280         290         300
FDAKNPFLAA VTANRKLNQG TERHLMHLEL DISDSKIRYE SGDHVAVYPA NDSALVNQIG

       310         320         330         340         350         360
EILGADLDVI MSLNNLDEES NKKHPFPTPT TYRTALTYYL DITNPPRTNV LYELAQYASE

       370         380         390         400         410         420
PSEQEHLHKM ASSSGEGKEL YLSWVVEARR HILAILQDYP SLRPPIDHLL ELLPRLQARY

       430         440         450         460         470         480
YSIASSSKVH PNSVHITAVA VEYEAKSGRV NKGVATSWLR AKEPAGENGG RALVPMFVRK

       490         500         510         520         530         540
SQFRLPFKST TPVIMVGPGT GIAPFMGFIQ ERAWLREQGK EVGETLLYYG ARRSDEDYLY

       550         560         570         580         590         600
REELARFHKD GALTQLNVAF SREQAHKVYV QHLLKRDREH LWKLIHEGGA HIYVAGDARN

       610         620         630         640
MAKDVQNTFY DIVAEFGPME HTQAVDYVKK LMTKGRYSLD VWS
```

His-tagged POR 56-678 cysless E127C amino acid sequence

```
        10          20          30          40          50          60
MGSSHHHHHH SSGLVPRGSH MIQTTAPPVK ESSFVEKMKK TGRNIIVFYG SQTGTAEEFA

        70          80          90         100         110         120
NRLSKDAHRY GMRGMSADPE EYDLADLSSL PCIDKSLVVF AMATYGEGDP TDNAQDFYDW

       130         140         150         160         170         180
LQETDVDLTG VKFAVFGLGN KTYEHFNAMG KYVDQRLEQL GAQRIFELGL GDDDGNLEED

       190         200         210         220         230         240
FITWREQFWP AVAEFFGVEA TGEESSIRQY ELVVHEDMDV AKVYTGEMGR LKSYENQKPP

       250         260         270         280         290         300
FDAKNPFLAA VTANRKLNQG TERHLMHLEL DISDSKIRYE SGDHVAVYPA NDSALVNQIG

       310         320         330         340         350         360
EILGADLDVI MSLNNLDEES NKKHPFPTPT TYRTALTYYL DITNPPRTNV LYELAQYASE

       370         380         390         400         410         420
PSEQEHLHKM ASSSGEGKEL YLSWVVEARR HILAILQDYP SLRPPIDHLL ELLPRLQARY

       430         440         450         460         470         480
YSIASSSKVH PNSVHITAVA VEYEAKSGRV NKGVATSWLR AKEPAGENGG RALVPMFVRK

       490         500         510         520         530         540
SQFRLPFKST TPVIMVGPGT GIAPFMGFIQ ERAWLREQGK EVGETLLYYG ARRSDEDYLY

       550         560         570         580         590         600
REELARFHKD GALTQLNVAF SREQAHKVYV QHLLKRDREH LWKLIHEGGA HIYVAGDARN
```

```
       610         620         630         640
MAKDVQNTFY DIVAEFGPME HTQAVDYVKK LMTKGRYSLD VWS
```

His-tagged POR 56-678 cysless Q157C amino acid sequence

```
        10          20          30          40          50          60
MGSSHHHHHH SSGLVPRGSH MIQTTAPPVK ESSFVEKMKK TGRNIIVFYG SQTGTAEEFA

        70          80          90         100         110         120
NRLSKDAHRY GMRGMSADPE EYDLADLSSL PEIDKSLVVF AMATYGEGDP TDNAQDFYDW

       130         140         150         160         170         180
LCETDVDLTG VKFAVFGLGN KTYEHFNAMG KYVDQRLEQL GAQRIFELGL GDDDGNLEED

       190         200         210         220         230         240
FITWREQFWP AVAEFFGVEA TGEESSIRQY ELVVHEDMDV AKVYTGEMGR LKSYENQKPP

       250         260         270         280         290         300
FDAKNPFLAA VTANRKLNQG TERHLMHLEL DISDSKIRYE SGDHVAVYPA NDSALVNQIG

       310         320         330         340         350         360
EILGADLDVI MSLNNLDEES NKKHPFPTPT TYRTALTYYL DITNPPRTNV LYELAQYASE

       370         380         390         400         410         420
PSEQEHLHKM ASSSGEGKEL YLSWVVEARR HILAILQDYP SLRPPIDHLL ELLPRLQARY

       430         440         450         460         470         480
YSIASSSKVH PNSVHITAVA VEYEAKSGRV NKGVATSWLR AKEPAGENGG RALVPMFVRK

       490         500         510         520         530         540
SQFRLPFKST TPVIMVGPGT GIAPFMGFIQ ERAWLREQGK EVGETLLYYG ARRSDEDYLY

       550         560         570         580         590         600
REELARFHKD GALTQLNVAF SREQAHKVYV QHLLKRDREH LWKLIHEGGA HIYVAGDARN

       610         620         630         640
MAKDVQNTFY DIVAEFGPME HTQAVDYVKK LMTKGRYSLD VWS
```

His-tagged POR 56-678 cysless Q157C N271C amino acid sequence

```
        10          20          30          40          50          60
MGSSHHHHHH SSGLVPRGSH MIQTTAPPVK ESSFVEKMKK TGRNIIVFYG SQTGTAEEFA

        70          80          90         100         110         120
NRLSKDAHRY GMRGMSADPE EYDLADLSSL PEIDKSLVVF AMATYGEGDP TDNAQDFYDW

       130         140         150         160         170         180
LCETDVDLTG VKFAVFGLGN KTYEHFNAMG KYVDQRLEQL GAQRIFELGL GDDDGNLEED

       190         200         210         220         230         240
FITWREQFWP AVAEFFGVEA TGEESSIRQY ELVVHEDMDV AKVYTGEMGR LKSYCNQKPP

       250         260         270         280         290         300
FDAKNPFLAA VTANRKLNQG TERHLMHLEL DISDSKIRYE SGDHVAVYPA NDSALVNQIG

       310         320         330         340         350         360
EILGADLDVI MSLNNLDEES NKKHPFPTPT TYRTALTYYL DITNPPRTNV LYELAQYASE

       370         380         390         400         410         420
PSEQEHLHKM ASSSGEGKEL YLSWVVEARR HILAILQDYP SLRPPIDHLL ELLPRLQARY

       430         440         450         460         470         480
YSIASSSKVH PNSVHITAVA VEYEAKSGRV NKGVATSWLR AKEPAGENGG RALVPMFVRK
```

```
       490         500         510         520         530         540
SQFRLPFKST TPVIMVGPGT GIAPFMGFIQ ERAWLREQGK EVGETLLYYG ARRSDEDYLY

       550         560         570         580         590         600
REELARFHKD GALTQLNVAF SREQAHKVYV QHLLKRDREH LWKLIHEGGA HIYVAGDARN

       610         620         630         640
MAKDVQNTFY DIVAEFGPME HTQAVDYVKK LMTKGRYSLD VWS
```

His-tagged POR 56-678 cysless S308C amino acid sequence

```
        10          20          30          40          50          60
MGSSHHHHHH SSGLVPRGSH MIQTTAPPVK ESSFVEKMKK TGRNIIVFYG SQTGTAEEFA

        70          80          90         100         110         120
NRLSKDAHRY GMRGMSADPE EYDLADLSSL PEIDKSLVVF AMATYGEGDP TDNAQDFYDW

       130         140         150         160         170         180
LQETDVDLTG VKFAVFGLGN KTYEHFNAMG KYVDQRLEQL GAQRIFELGL GDDDGNLEED

       190         200         210         220         230         240
FITWREQFWP AVAEFFGVEA TGEESSIRQY ELVVHEDMDV AKVYTGEMGR LKSYENQKPP

       250         260         270         280         290         300
FDAKNPFLAA VTANRKLNQG TERHLMHLEL DICDSKIRYE SGDHVAVYPA NDSALVNQIG

       310         320         330         340         350         360
EILGADLDVI MSLNNLDEES NKKHPFPTPT TYRTALTYYL DITNPPRTNV LYELAQYASE

       370         380         390         400         410         420
PSEQEHLHKM ASSSGEGKEL YLSWVVEARR HILAILQDYP SLRPPIDHLL ELLPRLQARY

       430         440         450         460         470         480
YSIASSSKVH PNSVHITAVA VEYEAKSGRV NKGVATSWLR AKEPAGENGG RALVPMFVRK

       490         500         510         520         530         540
SQFRLPFKST TPVIMVGPGT GIAPFMGFIQ ERAWLREQGK EVGETLLYYG ARRSDEDYLY

       550         560         570         580         590         600
REELARFHKD GALTQLNVAF SREQAHKVYV QHLLKRDREH LWKLIHEGGA HIYVAGDARN

       610         620         630         640
MAKDVQNTFY DIVAEFGPME HTQAVDYVKK LMTKGRYSLD VWS
```

His-tagged POR 56-678 cysless Q517C amino acid sequence

```
        10          20          30          40          50          60
MGSSHHHHHH SSGLVPRGSH MIQTTAPPVK ESSFVEKMKK TGRNIIVFYG SQTGTAEEFA

        70          80          90         100         110         120
NRLSKDAHRY GMRGMSADPE EYDLADLSSL PEIDKSLVVF AMATYGEGDP TDNAQDFYDW

       130         140         150         160         170         180
LQETDVDLTG VKFAVFGLGN KTYEHFNAMG KYVDQRLEQL GAQRIFELGL GDDDGNLEED

       190         200         210         220         230         240
FITWREQFWP AVAEFFGVEA TGEESSIRQY ELVVHEDMDV AKVYTGEMGR LKSYENQKPP

       250         260         270         280         290         300
FDAKNPFLAA VTANRKLNQG TERHLMHLEL DISDSKIRYE SGDHVAVYPA NDSALVNQIG

       310         320         330         340         350         360
EILGADLDVI MSLNNLDEES NKKHPFPTPT TYRTALTYYL DITNPPRTNV LYELAQYASE
```

```
       370        380        390        400        410        420
PSEQEHLHKM ASSSGEGKEL YLSWVVEARR HILAILQDYP SLRPPIDHLL ELLPRLQARY

       430        440        450        460        470        480
YSIASSSKVH PNSVHITAVA VEYEAKSGRV NKGVATSWLR AKEPAGENGG RALVPMFVRK

       490        500        510        520        530        540
SCFRLPFKST TPVIMVGPGT GIAPFMGFIQ ERAWLREQGK EVGETLLYYG ARRSDEDYLY

       550        560        570        580        590        600
REELARFHKD GALTQLNVAF SREQAHKVYV QHLLKRDREH LWKLIHEGGA HIYVAGDARN

       610        620        630        640
MAKDVQNTFY DIVAEFGPME HTQAVDYVKK LMTKGRYSLD VWS
```

His-tagged POR 56-678 cysless Q157C Q517C amino acid sequence

```
        10         20         30         40         50         60
MGSSHHHHHH SSGLVPRGSH MIQTTAPPVK ESSFVEKMKK TGRNIIVFYG SQTGTAEEFA

        70         80         90        100        110        120
NRLSKDAHRY GMRGMSADPE EYDLADLSSL PEIDKSLVVF AMATYGEGDP TDNAQDFYDW

       130        140        150        160        170        180
LCETDVDLTG VKFAVFGLGN KTYEHFNAMG KYVDQRLEQL GAQRIFELGL GDDDGNLEED

       190        200        210        220        230        240
FITWREQFWP AVAEFFGVEA TGEESSIRQY ELVVHEDMDV AKVYTGEMGR LKSYENQKPP

       250        260        270        280        290        300
FDAKNPFLAA VTANRKLNQG TERHLMHLEL DISDSKIRYE SGDHVAVYPA NDSALVNQIG

       310        320        330        340        350        360
EILGADLDVI MSLNNLDEES NKKHPFPTPT TYRTALTYYL DITNPPRTNV LYELAQYASE

       370        380        390        400        410        420
PSEQEHLHKM ASSSGEGKEL YLSWVVEARR HILAILQDYP SLRPPIDHLL ELLPRLQARY

       430        440        450        460        470        480
YSIASSSKVH PNSVHITAVA VEYEAKSGRV NKGVATSWLR AKEPAGENGG RALVPMFVRK

       490        500        510        520        530        540
SCFRLPFKST TPVIMVGPGT GIAPFMGFIQ ERAWLREQGK EVGETLLYYG ARRSDEDYLY

       550        560        570        580        590        600
REELARFHKD GALTQLNVAF SREQAHKVYV QHLLKRDREH LWKLIHEGGA HIYVAGDARN

       610        620        630        640
MAKDVQNTFY DIVAEFGPME HTQAVDYVKK LMTKGRYSLD VWS
```

His-tagged POR 56-678 cysless Q157C Q517C Δ[236]TGEE[239] amino acid sequence

```
        10         20         30         40         50         60
MGSSHHHHHH SSGLVPRGSH MIQTTAPPVK ESSFVEKMKK TGRNIIVFYG SQTGTAEEFA

        70         80         90        100        110        120
NRLSKDAHRY GMRGMSADPE EYDLADLSSL PEIDKSLVVF AMATYGEGDP TDNAQDFYDW

       130        140        150        160        170        180
LCETDVDLTG VKFAVFGLGN KTYEHFNAMG KYVDQRLEQL GAQRIFELGL GDDDGNLEED

       190        200        210        220        230        240
FITWREQFWP AVAEFFGVEA SSIRQYELVV HEDMDVAKVY TGEMGRLKSY ENQKPPFDAK
```

```
       250         260         270         280         290         300
NPFLAAVTAN RKLNQGTERH LMHLELDISD SKIRYESGDH VAVYPANDSA LVNQIGEILG

       310         320         330         340         350         360
ADLDVIMSLN NLDEESNKKH PFPTPTTYRT ALTYYLDITN PPRTNVLYEL AQYASEPSEQ

       370         380         390         400         410         420
EHLHKMASSS GEGKELYLSW VVEARRHILA ILQDYPSLRP PIDHLLELLP RLQARYYSIA

       430         440         450         460         470         480
SSSKVHPNSV HITAVAVEYE AKSGRVNKGV ATSWLRAKEP AGENGGRALV PMFVRKSCFR

       490         500         510         520         530         540
LPFKSTTPVI MVGPGTGIAP FMGFIQERAW LREQGKEVGE TLLYYGARRS DEDYLYREEL

       550         560         570         580         590         600
ARFHKDGALT QLNVAFSREQ AHKVYVQHLL KRDREHLWKL IHEGGAHIYV AGDARNMAKD

       610         620         630
VQNTFYDIVA EFGPMEHTQA VDYVKKLMTK GRYSLDVWS
```

His-tagged full-length POR cysless Q157C Q517C amino acid sequence

```
        10          20          30          40          50          60
MKKTAIAIAV ALAGFATVAQ AHHHHHHGDS HEDTSATMPE AVAEEVSLFS TTDMVLFSLI

        70          80          90         100         110         120
VGVLTYWFIF RKKKEEIPEF SKIQTTAPPV KESSFVEKMK KTGRNIIVFY GSQTGTAEEF

       130         140         150         160         170         180
ANRLSKDAHR YGMRGMSADP EEYDLADLSS LPEIDKSLVV FAMATYGEGD PTDNAQDFYD

       190         200         210         220         230         240
WLCETDVDLT GVKFAVFGLG NKTYEHFNAM GKYVDQRLEQ LGAQRIFELG LGDDDGNLEE

       250         260         270         280         290         300
DFITWREQFW PAVAEFFGVE ATGEESSIRQ YELVVHEDMD VAKVYTGEMG RLKSYENQKP

       310         320         330         340         350         360
PFDAKNPFLA AVTANRKLNQ GTERHLMHLE LDISDSKIRY ESGDHVAVYP ANDSALVNQI

       370         380         390         400         410         420
GEILGADLDV IMSLNNLDEE SNKKHPFPTP TTYRTALTYY LDITNPPRTN VLYELAQYAS

       430         440         450         460         470         480
EPSEQEHLHK MASSSGEGKE LYLSWVVEAR RHILAILQDY PSLRPPIDHL LELLPRLQAR

       490         500         510         520         530         540
YYSIASSSKV HPNSVHITAV AVEYEAKSGR VNKGVATSWL RAKEPAGENG GRALVPMFVR

       550         560         570         580         590         600
KSCFRLPFKS TTPVIMVGPG TGIAPFMGFI QERAWLREQG KEVGETLLYY GARRSDEDYL

       610         620         630         640         650         660
YREELARFHK DGALTQLNVA FSREQAHKVY VQHLLKRDRE HLWKLIHEGG AHIYVAGDAR

       670         680         690         700
NMAKDVQNTF YDIVAEFGPM EHTQAVDYVK KLMTKGRYSL DVWS
```

MALDI-TOF protein mass spectra

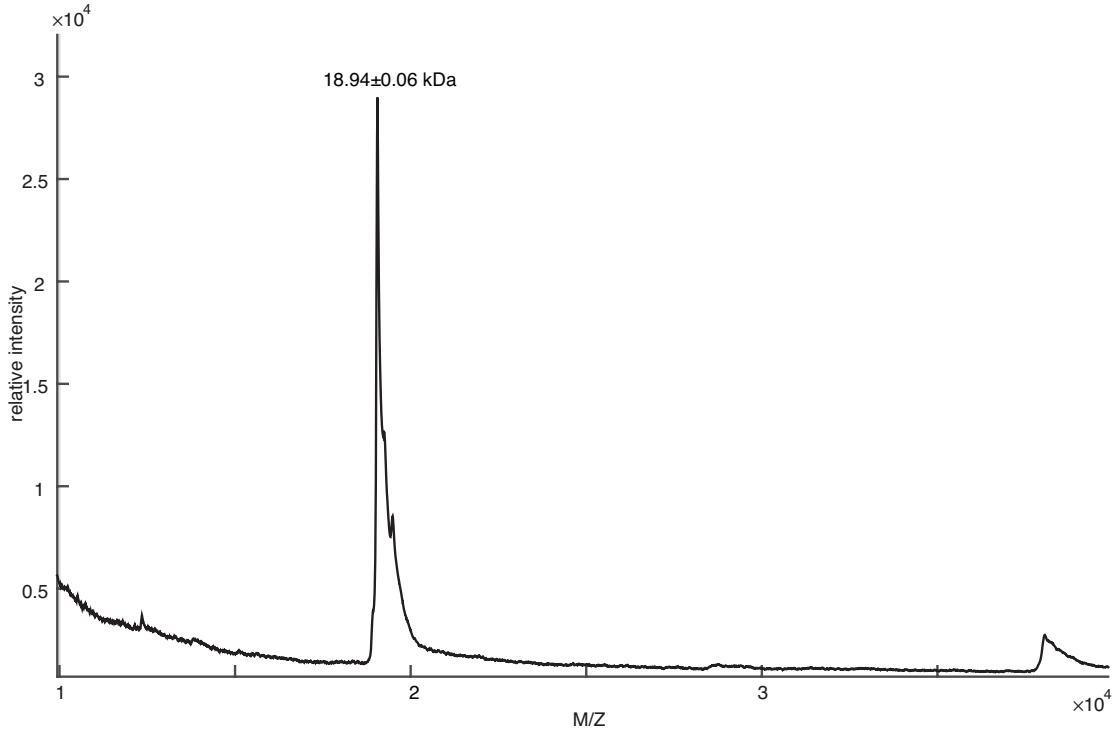

Figure 55. MALDI-TOF mass spectra H-Ras 1-166 ($Mw_{theoretical}$=18837 Da)

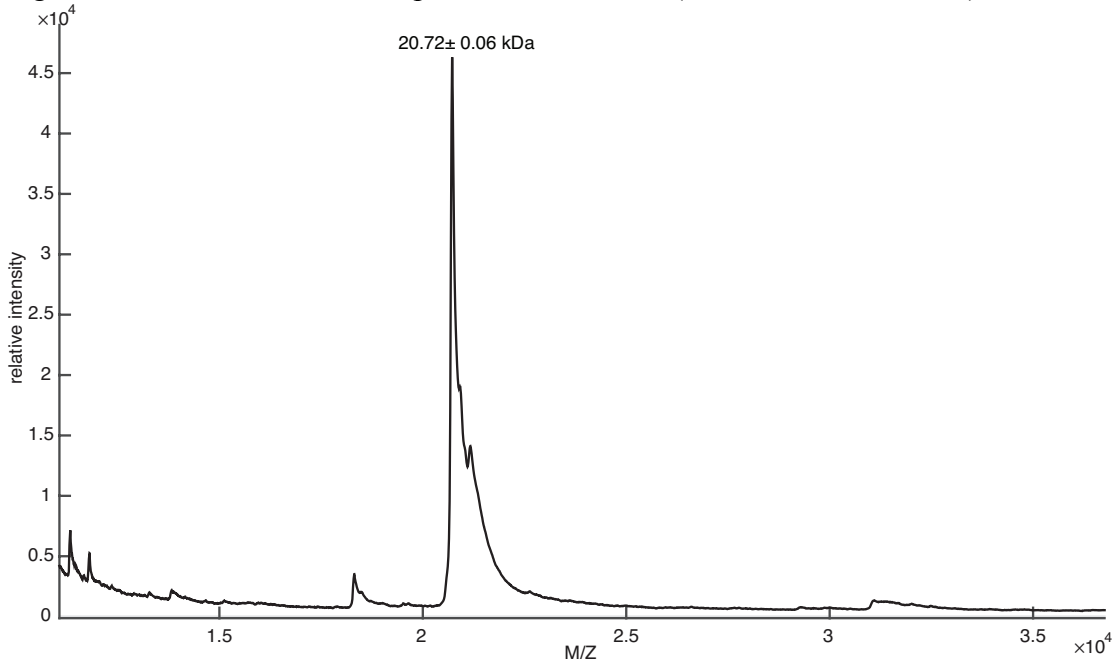

Figure 56. MALDI-TOF mass spectra H-Ras 1-181 ($Mw_{theoretical}$=20678 Da)

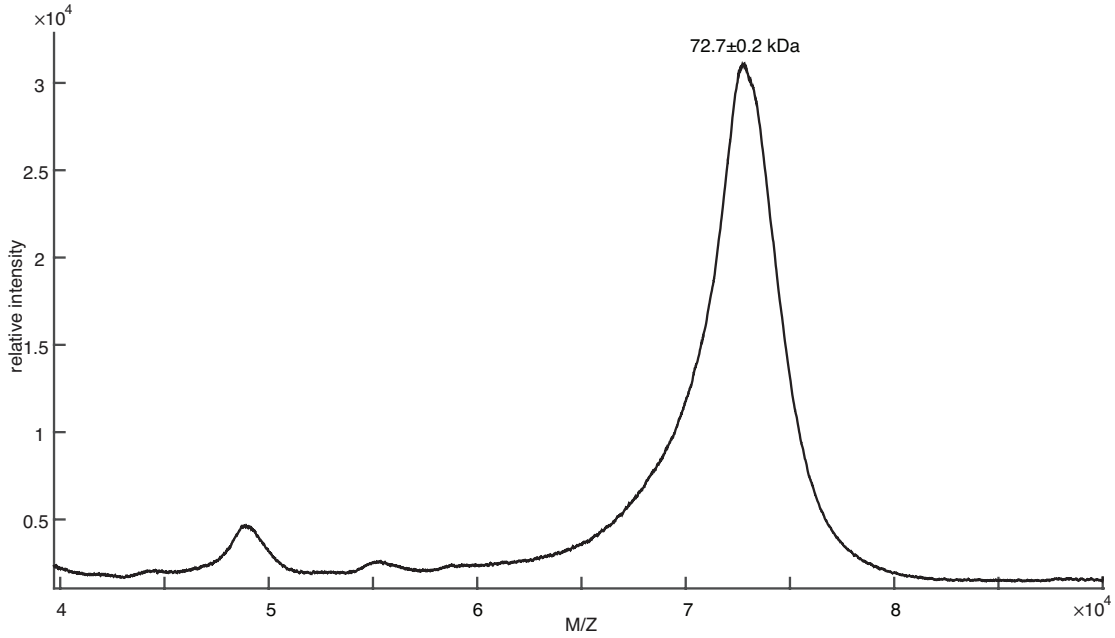

Figure 57. MALDI-TOF mass spectra His-tagged POR 56-678 cysless ($Mw_{theoretical}$=72764 Da)

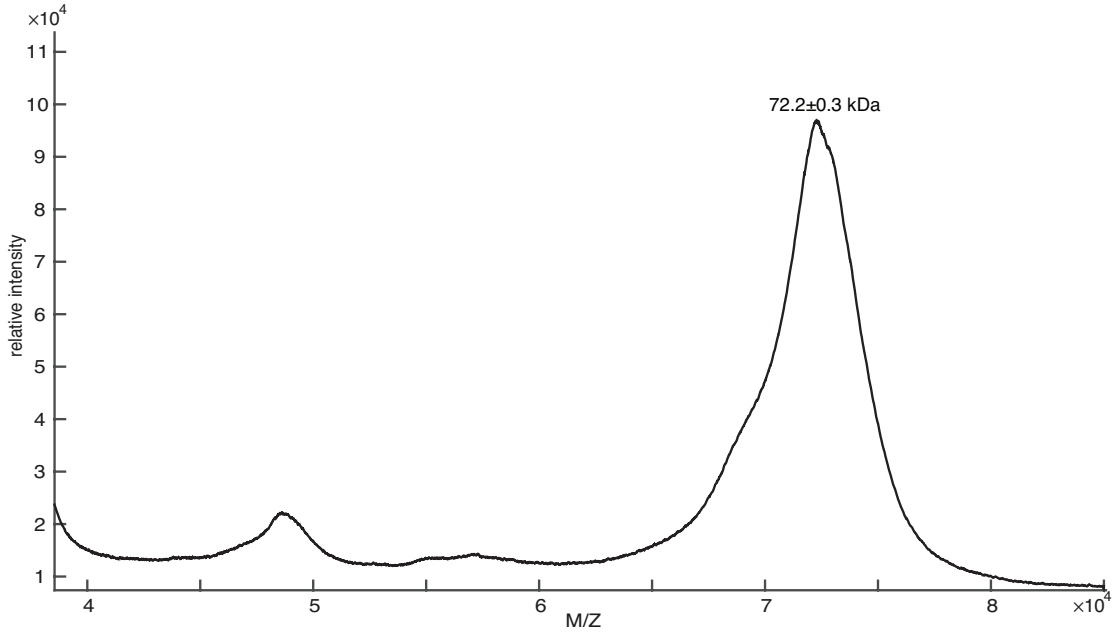

Figure 58. MALDI-TOF mass spectra His-tagged POR 56-678 Δ^{236}TGEE^{239} cysless Q157C Q517C ($Mw_{theoretical}$=72297Da)

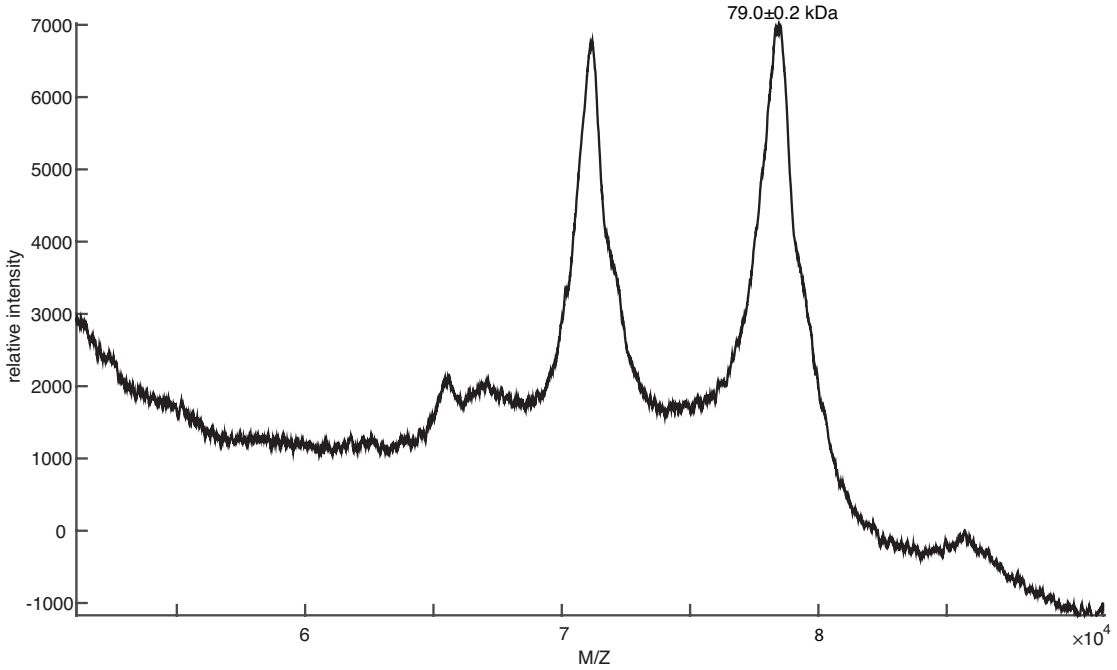

Figure 59. MALDI-TOF mass spectra of His-tagged full-length POR cysless Q157C Q517C incorporated into a DOPC nanodisc acquired after NMR experiment. ($Mw_{theoretical}$=79511 Da)

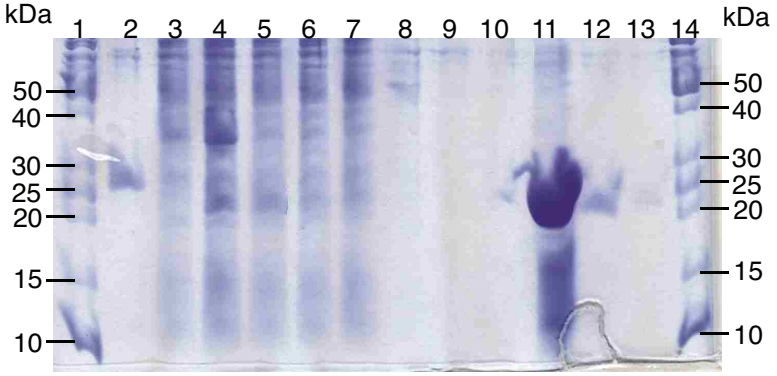

Figure 60. Analysis of MSP1D1 expression level and its purification by SDS-PAGE. PageRuler™ Unstained Protein Ladder (ThermoFisher, 26614) (lane 1,14). Purified TEV protease (lane 2). Cell lysate of non-induced (lane 3) and induced (lane 4) expression culture; lysate SN after centrifugation of induced (lane 5) expression culture that loaded into the His60 NiSuperflow column. His60 NiSuperflow column flow-through (lanes 6,7); wash (8,9) and elution from the column (lanes 10-13).